2012

GEOMETRIC CONTROL OF INFLATABLE SURFACES

Isaac John Scherrer
University of Kentucky, isaac.scherrer@uky.edu

Recommended Citation

Scherrer, Isaac John, "GEOMETRIC CONTROL OF INFLATABLE SURFACES" (2012). *Theses and Dissertations--Mechanical Engineering*. 11.
https://uknowledge.uky.edu/me_etds/11

STUDENT AGREEMENT:

I represent that my thesis or dissertation and abstract are my original work. Proper attribution has been given to all outside sources. I understand that I am solely responsible for obtaining any needed copyright permissions. I have obtained and attached hereto needed written permission statements(s) from the owner(s) of each third-party copyrighted matter to be included in my work, allowing electronic distribution (if such use is not permitted by the fair use doctrine).

I hereby grant to The University of Kentucky and its agents the non-exclusive license to archive and make accessible my work in whole or in part in all forms of media, now or hereafter known. I agree that the document mentioned above may be made available immediately for worldwide access unless a preapproved embargo applies.

I retain all other ownership rights to the copyright of my work. I also retain the right to use in future works (such as articles or books) all or part of my work. I understand that I am free to register the copyright to my work.

REVIEW, APPROVAL AND ACCEPTANCE

The document mentioned above has been reviewed and accepted by the student's advisor, on behalf of the advisory committee, and by the Director of Graduate Studies (DGS), on behalf of the program; we verify that this is the final, approved version of the student's dissertation including all changes required by the advisory committee. The undersigned agree to abide by the statements above.

Isaac John Scherrer, Student

Dr. Susanne Weaver Smith, Major Professor

Dr. James McDonough, Director of Graduate Studies

GEOMETRIC CONTROL OF INFLATABLE SURFACES

THESIS

A thesis submitted in partial fulfillment of the
requirements for the degree of Master of Science in
Mechanical Engineering in the College of Engineering
at the University of Kentucky

By
Isaac John Scherrer
Lexington, Kentucky
Director: Dr. Susanne Weaver Smith Professor of Mechanical Engineering
Lexington, Kentucky
2012

ABSTRACT OF THESIS

GEOMETRIC CONTROL OF INFLATABLE SURFACES

High precision inflatable surfaces were introduced when NASA created the ECHO 1 Balloon in 1960. The experiment proved that inflatable structures were a feasible alternative to their rigid counterparts for high precision applications. Today inflatable structures are being used in aviation and aerospace applications and the benefits of using such structures are being recognized. Inflatable structures used in high precision structures require the inflatable surfaces to have controllable and predictable geometries. Many applications such as solar sails and radar reflectors require the surface of such structures to have a uniform surfaces as such surfaces improve the efficiency of the structure. In the study presented, tests were conducted to determine which combination of factors affect surface flatness on a triangular test article. Factors tested include, three boundary conditions, two force loadings, and two fabric orientations. In total, twelve tests were conducted and results showed that which force loading and fabric orientations used greatly affected the Root Mean Square (RMS) of the surface. It was determined that using the triangular clamp along with 0^0 fabric orientation and high force loading provided the best results.

KEYWORDS: Inflatable Structures, Gossamer Structures, Geometric Control, Photogrammetry, Woven Fabrics

Isaac John Scherrer

July 31, 2012

GEOMETRIC CONTROL OF INFLATABLE SURFACES

By

Isaac John Scherrer

Dr. Susanne Weaver Smith

Director of Thesis

Dr. James McDonough

Director of Graduate Studies

July 31, 2012

This thesis is dedicated to my grandmother, Ruth Scherrer and my parents, Sharon and Daniel Scherrer. You have always stressed the importance of an education and are a major reason I decided to earn my degree. Additionally this is dedicated to my Fiancé, Ellen Foster, without your encouragement and support this would not have been possible.

ACKNOWLEDGEMENTS

I would like to express utmost gratitude to my academic advisor, Dr. Suzanne Weaver Smith. Without her guidance and insight, this would not have been possible. She supported me in my undergraduate degree and continued her support in my post-baccalaureate education. Her support has been unwavering.

Lastly I would like to express gratitude to Dr. Keith Rouch, and Dr. Tim Wu for accepting to be part of my thesis committee.

TABLE OF CONTENTS

ACKNOWLEDGEMENTS iii
TABLE OF CONTENTS iv
LIST OF TABLES vi
LIST OF FIGURES vii
Chapter 1 Introduction 1
  1.1 Background 1
  1.2 Objective of the Thesis 1
  1.3 Thesis Overview 2
Chapter 2 Review of Literature 3
  2.1 Inflatable Structures 3
  2.2 Measuring Geometric Surfaces 12
  2.3 Improving Geometric Control of Surfaces 16
Chapter 3 PhotoModler 20
  3.1 PhotoModler Introduction 20
  3.2 PhotoModler 6 Study 21
  3.3 PhotoModler 6 Study Results 30
  3.4 PhotoModler 6 Study Conclusions 37
Chapter 4 Fixture Design 39
  4.1 Test Fixture Introduction 39
  4.2 Initial Fixture Design 40
  4.2 Final Fixture Design 45
Chapter 5 Fabric Testing 47
  5.1 Test Introduction 47
  5.2 Yield Stress of Material 51
  5.3 Test Results 60
Chapter 6 Conclusion 69
  6.1 Conclusions 69
  6.2 Future Work 71
Appendix A: 73

A.1 PhotoModler Error 73
A.2 PhotoModler RMS Values 75
A.3 Stress-Strain Graphs 77
A.4 Yield Strength Graphs 82
A.5 Contour Lines 86
A.6 Contour Plots 90
Bibliography 102
Vita 105

LIST OF TABLES

Table 1: Comparison of Wight and Stowed Volume for a 0.5 m Diameter Reflector (Mathers, February, 2010)(Used with Permission) 7
Table 2: Geometric Requirements (Fulcher, 2012) (Used with Permission) 13
Table 3: Camera Locations 25
Table 4: Loading Cases 48
Table 5: Modulus of Elasticity for Warp and Fill Directions 53
Table 6: Calculated Yield Strength Using Offset Method 54
Table 7: Yellow Double Coated ILC Dover Material Thickness 56
Table 8: Combination of Factors 62
Table 9: Index for Results 62
Table 10: RMS Values 62
Table 11: Maximum Positive Deflection 66
Table 12: Maximum Negative Deflection 66

LIST OF FIGURES

Figure 1: Echo I Balloon (Freeland, Bilyeu, Veal, & Mikulas, 1998) (Image Courtesy of NASA)....... 3
Figure 2: Deployed IAE (Preliminary Misson Report: Spartan 207/Inflatable AntenaExperiment Flown on STS-77, Feb, 1997) (Image Courtesy of NASA) 6
Figure 3: IAE Stowed in Launch Container (Mathers, February, 2010)(Used with Permission) 7
Figure 4: Deployment of the IAE (Image Courtesy of NASA) 8
Figure 5: Solar Sail Measuring 33 ft. x 33 ft. (Jensen, 2004) (Image Courtesy of NASA) 10
Figure 6: Goodyear GA-33 Inflatoplane (Jacob, Smith, Cadogan, & Scarborough, 2007) (Used with Permission) 11
Figure 7: Survivalbility of Components on UAVs (Simpson, 2008) (Used with Permission) 11
Figure 8: Projected Targets on Fabric (Pappa, Black, & Blandino) (Used with Permission) 15
Figure 9: Shear Compliant Border (Talley, et al., April, 2002)(Used with Permission) 17
Figure 10: Catenary Cable Design (Talley, et al., April, 2002)(Used with Permission).......... 18
Figure 11: PhotoModler Experimental Set-Up 22
Figure 12: 45 ^{o} Vertical Angle Camera Position 23
Figure 13: PhotoModler Study Setup 24
Figure 14: Camera Locations 26
Figure 15: Camera Locations 27
Figure 16: Point Locations Used for Scaling 28
Figure 17: Camera Positions Using 2-5 Photos 29
Figure 18: Camera Positions Using 6-8 Photos 30
Figure 19: PhotoModler 4 Inch Error 31
Figure 20: PhotoModler 10 Inch Error 32
Figure 21: PhotoModler 10 Inch Error with Upper and Lower Bound Requirements 33
Figure 22: Normalized Error 34
Figure 23: RMS Values For 10 Inch Segment 35
Figure 24: PhotoModler RMS For 10 Inch Segment with Upper and Lower Bounds 36
Figure 25: Test Material 40
Figure 26: Initial Fixture Setup with Force Directions Shown 41
Figure 27: Rigid Clamp Design 42
Figure 28: Fixed Clamp Setup 43
Figure 29: Pulley and Pulley Mount 44
Figure 30: Final Fixture Setup 46
Figure 31: Loading Configuration 48
Figure 32: Fabric Orientation 49
Figure 33: Boundary Conditions 49
Figure 34: Stress-Strain Graph Warp_1 52
Figure 35: Stress-Strain Warp_1 Line of Best Fit 52
Figure 36: Yield Strength Using Offset Method 53

Figure 37: Yield Strength Warp_4 55
Figure 38: Yield Strength Fill_3 55
Figure 39: Shear Clamp Dimensions 57
Figure 40: Contour Line Locations 58
Figure 41: Contour A- A.......... 59
Figure 42: Contour B-B.......... 59
Figure 43: Example Contour with Average Deflection Shown 61
Figure 44: Contour Line Locations 63
Figure 45: Case 3 Contour Lines 64
Figure 46: Case 10 Contour Lines 65
Figure 47: Case 1 Contour Plot 67
Figure 48: Case 4 Contour Plot 68
Figure 49: Additional Fabric Orientation 72
Figure 50: PhotoModler 2 Inch Error 73
Figure 51: PhotoModler 4 Inch Error 73
Figure 52: PhotoModler 6 Inch Error 74
Figure 53: PhotoModler 8 Inch Error 74
Figure 54: PhotoModler 10 Inch Error 75
Figure 55: RMS Values For a 2 Inch Segment 75
Figure 56: RMS Values For A 4 Inch Segment 76
Figure 57: RMS Values For A 6 Inch Segment 76
Figure 58: RMS Values For A 8 Inch Segment 77
Figure 59: Stress-Strain Warp_1 Line of Best Fit 77
Figure 60: Stress-Strain Warp_2 Line of Best Fit 78
Figure 61: Stress-Strain Warp_3 Line of Best Fit 78
Figure 62: Stress-Strain Warp_4 Line of Best Fit 79
Figure 63: Stress-Strain Warp_5 Line of Best Fit 79
Figure 64: Stress-Strain Fill_1 Line of Best Fit 80
Figure 65: Stress-Strain Fill_2 Line of Best Fit 80
Figure 66: Stress-Strain Fill_3 Line of Best Fit 81
Figure 67: Stress-Strain Fill_4 Line of Best Fit 81
Figure 68: Stress-Strain Fill_5 Line of Best Fit 82
Figure 69: Yield Strength Warp_1 82
Figure 70: Yield Strength Warp_2 83
Figure 71: Yield Strength Warp_3 83
Figure 72: Yield Strength Warp_4 83
Figure 73: Yield Strength Warp_5 84
Figure 74: Yield Strength Fill_1 84
Figure 75: Yield Strength Fill_2 85
Figure 76: Yield Strength Fill_3 85
Figure 77: Yield Strength Fill_4 85
Figure 78: Yield Strength Fill_5 86

Figure 79: Case 1 Contour Lines..86
Figure 80: Case 2 Contour Lines..86
Figure 81: Case 3 Contour Lines..87
Figure 82: Case 4 Contour Lines..87
Figure 83: Case 5 Contour Lines..87
Figure 84: Case 6 Contour Lines..87
Figure 85: Case 7 Contour Lines..88
Figure 86: Case 8 Contour Lines..88
Figure 87: Case 9 Contour Lines..88
Figure 88: Case 10 Contour Lines..88
Figure 89: Case 11 Contour Lines..89
Figure 90: Case 12 Contour Lines..89
Figure 91: Case 1 Contour Plot 90
Figure 92: Case 2 Contour Plot 91
Figure 93: Case 3 Contour Plot 92
Figure 94: Case 4 Contour Plot 93
Figure 95: Case 5 Contour Plot 94
Figure 96: Case 6 Contour Plot 95
Figure 97: Case 7 Contour Plot 96
Figure 98: Case 8 Contour Plot 97
Figure 99: Case 9 Contour Plot 98
Figure 100: Case 10 Contour Plot 99
Figure 101: Case 11 Contour Plot 100
Figure 102: Case 12 Contour Plot 101

Chapter 1 Introduction

1.1 Background

Inflatable structures have long been recognized to have many benefits compared to their counterparts that are made out of rigid materials such as aluminum and steel. One reasons inflatable structures have not seen expansive use in areas such as space and aviation is that the geometry and the material of the structures are not as easily as predictable as rigid materials. Since many of the areas that seek to use inflatable structures require a high level of precision, inflatable structures have seen limited use in the space and aviation industry.

As new plans for future space structures and winged aircraft emerge, the benefits for using inflatables structures are becoming increasingly more desirable. To make a significant impact on the future, geometric control of the inflatable components must be accurate as well as predictable. Understanding what factors have a significant effect on the geometric surface of inflatable structures is the basis of the research that was conducted at the University of Kentucky and is the topic of my thesis.

1.2 Objective of the Thesis

The motivation behind this thesis is to get an understanding of how the combination of different boundary conditions, bi-axial loadings, and fabric orientation affect the overall flatness of a triangular piece of inflatable material. Three different types of boundary conditions, two different bi-axial loading scenarios, and two different fabric orientations will be examined to see their effect on surface flatness. To accurately measure the surface flatness of the material, photogrammetry will be used, since it has been extensively studied and is able to provide accurate and repeatable results. After analyzing the data, the information gained could provide significant insight into how to effectively control inflatable structures, thus making use of inflatable structures more viable.

1.3 Thesis Overview

Chapter 2 of this thesis concerns the literature that has been documented on previous research in the field of inflatable structures as well as photogrammetry. Chapter 3 will discuss guidelines in using photogrammetry as well as the accuracy capabilities of the photogrammetry software used compared to manufacture’s accuracy. Chapter 4 will discuss the evolution of the fixture used in the testing. Chapter 5 will describe testing that was completed to ensure the material did not yield when forces were applied, as well as focusing on the results of the research. Chapter 6 will discuss conclusions made in testing and describe possible future research on the topic.

Chapter 2 Review of Literature

2.1 Inflatable Structures

Since inflatable structures were introduced for space applications with the Echo I Balloon in the early 1960's, many have recognized the advantages that such structures possess. The Echo I Balloon was launched into orbit on August 12, 1960 and was designed to be able to calibrate radars. The Echo I Balloon proved that inflatable structures were a technology that could be utilized for space applications, and that inflatable structures could meet the surface precision requirements that are involved with many space structures. The Echo I Balloon was designed to be a perfect sphere since having a perfect sphere would allow scientists to use analytical equations and to accurately calibrate their radars. Figure 1 displays the large size of the structure. A person can be seen at the base of the balloon for a height reference.

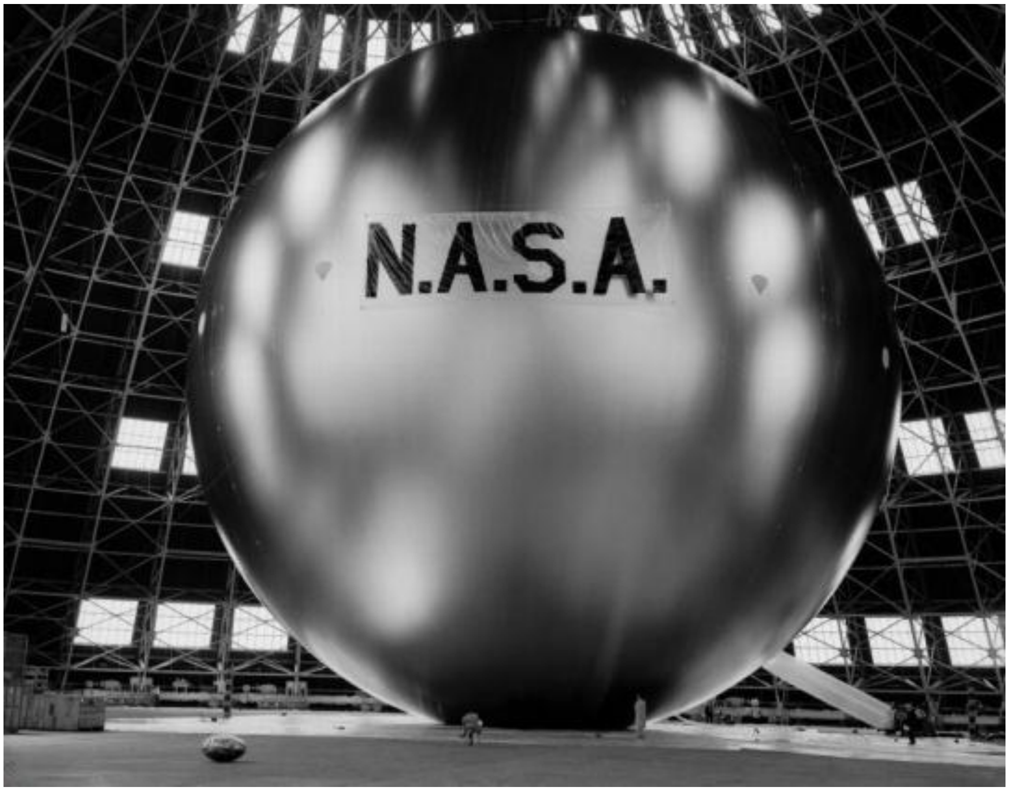

Figure 1: Echo I Balloon (Freeland, Bilyeu, Veal, & Mikulas, 1998) (Image Courtesy of NASA)

Additionally the Echo program highlighted the capabilities of inflatable structures. The major advantage in using inflatable structures can be seen with the Echo I Balloon in regards to its packing efficiency. When the balloon was fully inflated it had a diameter of 100 feet and was able to compress into a spherical container with a diameter of 26 inches (Freeland, Bilyeu, Veal, & Mikulas, 1998).

Since the balloon was able to compress into such a small stowed volume, launching large inflatable structures became feasible and is a very attractive technology since it opens up many possibilities on other missions, especially where storage space is an issue. In the case of the Echo I Balloon, the balloon was able to expand to a volume over 98,000 times its stowed volume. Since the balloon was built using a very thin, light-weight material, it only weighed 136 lbs. This is a drastic reduction in weight if compared to a similar non-inflatable system. For example, if we take the weight of a 2,300 foot diameter inflatable antenna and take into account its replacement gas, the weight is comparable to a mechanical system that is around 32-66 feet in diameter (Thomas & Friese, 1980). Since the Echo I Balloon utilized inflatable technology, there was no need for an internal structure to hold the shape of the sphere, instead the sphere used gases to inflate and maintain the shape of the balloon.

One issue with using an inflatable structure in space is that the gases can rapidly leak from the sphere especially considering that in one day it is estimated that about 4.36 inch^2 of holes are put into the sphere due to micrometeoroids (Clemmons, 1964). To solve the issue of the sphere not being able to retain its shape due impacts by micrometeoroids, scientists came up with an idea to use the material properties of the sphere to their advantage. Due to the fact the balloon was coated in a thin layer of aluminum, the sphere was able to be inflated to the point that the aluminum yielded a small amount, and was therefore able to be strain hardened and became rigid. Consequently the balloon did not rely on the gases to stay inflated (Cobb, Black, & Swenson, 2010).

Building upon on the success of the Echo project, L'Garde Inc. built an inflatable antenna comprised of multiple inflatable structures. The Inflatable Antenna Experiment (IAE) consisted of an inflatable reflector assembly which was made up of three 92-foot inflatable struts, one 46-foot diameter torus and a 0.01 inch of aluminized mylar material for the reflector itself. The antenna was designed to have a surface accuracy of 0.04 inch RMS in comparison to the proposed shape. The IAE was launched in May of 1996 (Freeland, Bilyeu, Veal, & Mikulas, 1998). The deployed IAE can be seen in Figure 2.

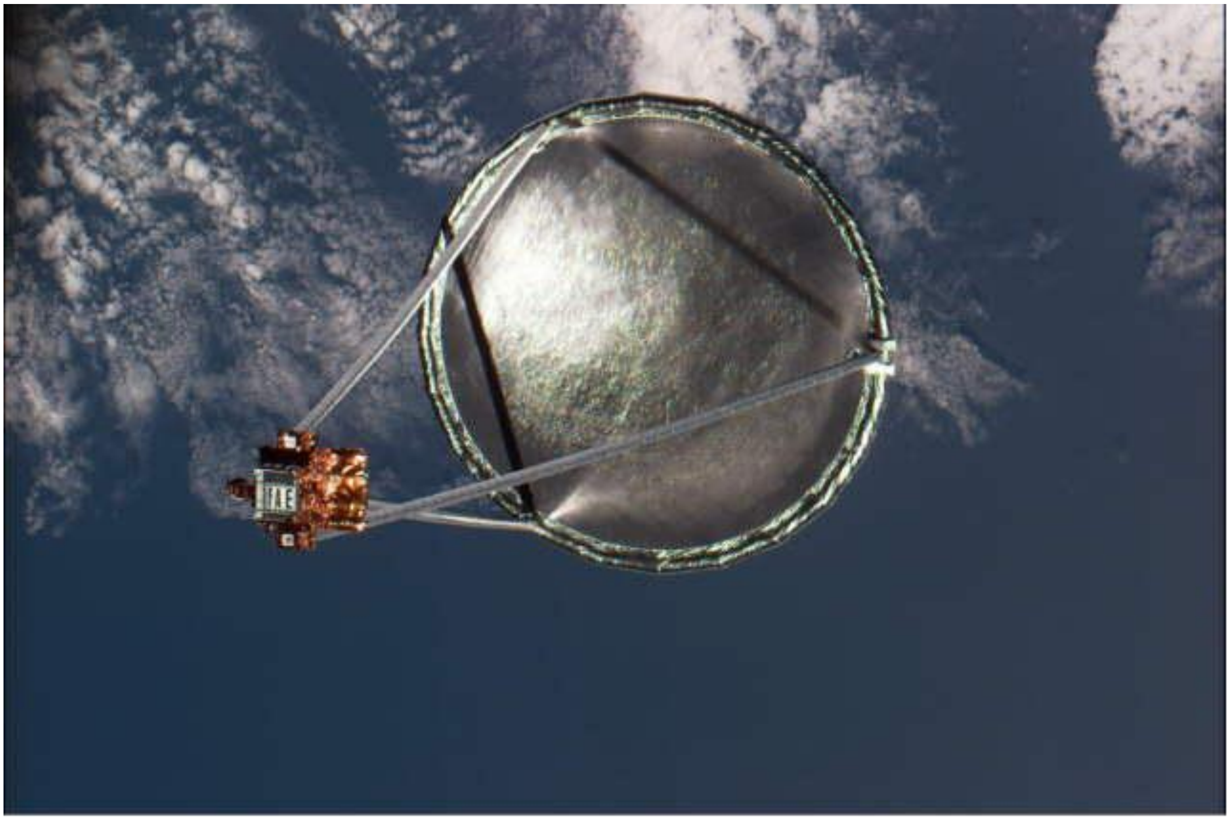

Figure 2: Deployed IAE (Preliminary Misson Report: Spartan 207/Inflatable AntenaExperiment Flown on STS-77, Feb, 1997) (Image Courtesy of NASA)

To pack the IAE most efficiently, the workers at L'Garde used their past experience in packing large quantities of smaller inflatable structures and it was concluded that folding the struts and part of the lenticular structure in a "z" configuration would produce the most compact stowed volume (Freeland, R. E.; Veal, G. R., 1998). Since one of the main advantages of using inflatables is their packing efficiency, being able to pack them into the smallest container is essential. The IAE in its initial stowed container can be seen in Figure 3.

Figure 3: IAE Stowed in Launch Container (Mathers, February, 2010)(Used with Permission)

To get a better understanding of how inflatable structures weight and packing efficiency compares to other materials, Table 1 can be referenced.

Table 1: Comparison of Wight and Stowed Volume for a 0.5 m Diameter Reflector (Mathers, February, 2010)(Used with Permission)

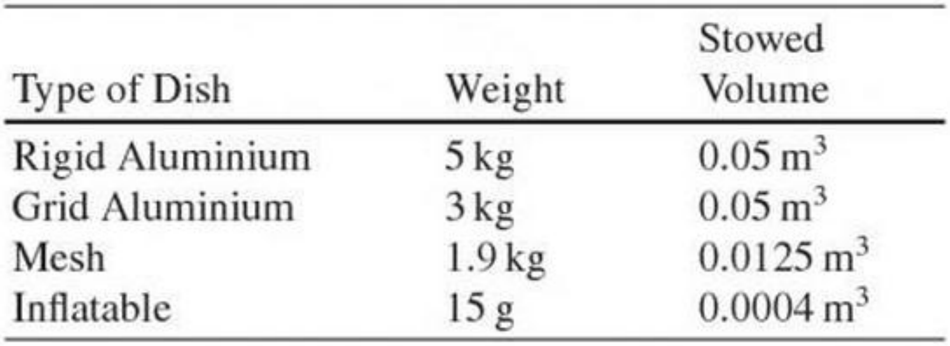

Type of Dish	Weight	Stowed Volume
Rigid Aluminium	5 kg	0.05 m^3
Grid Aluminium	3 kg	0.05 m^3
Mesh	1.9 kg	0.0125 m^3
Inflatable	15 g	0.0004 m^3

Wanting to demonstrate the utility of inflatable structures, the IAE had 5 major goals:

1. Show Inflatable structures are an inexpensive alternative to mechanical structures.
2. Showcase how inflatable structures are capable of having a high packing efficiency.
3. Display the reliability of inflatables.
4. Show that inflatables can have a high surface precision.
5. Be able to measure surface precision in orbit (Freeland, Bilyeu, Veal, & Mikulas, 1998).

Although considered a success, an unplanned event occurred on the mission. During the deployment, residual air was present inside the stowed inflatable structure before being deployed. This resulted in the antenna inflating at a more aggressive rate than designed. The violent deployment threatened to twist and/or tangle the structure, potentially causing catastrophic failure. The deployment can be seen in Figure 4.

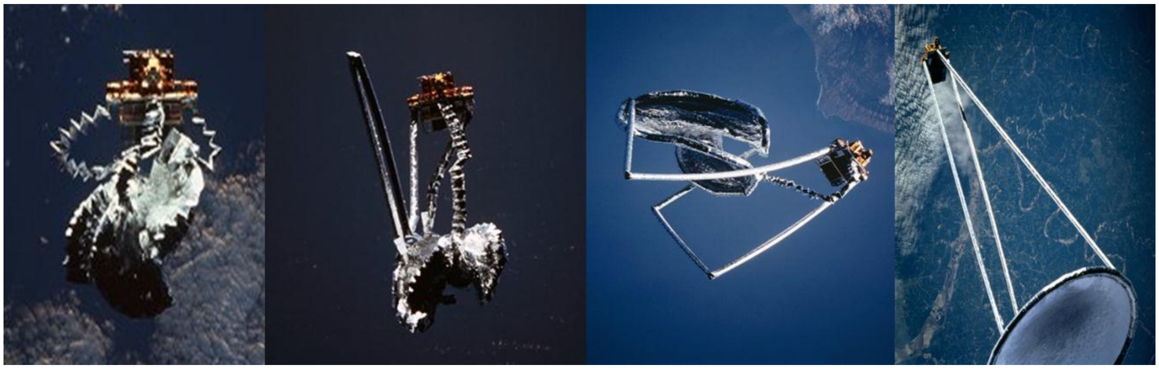

Figure 4: Deployment of the IAE (Image Courtesy of NASA)

Even though the IAE did not deploy as expected, it was considered to be a success and the antenna was able to deploy as designed. The deployed antenna had a surface accuracy of 0.08 inch RMS which was only 0.04 inch RMS off the design goal (Mathers, February, 2010). The experiment demonstrated the robustness of inflatable structures, in addition to showing that inflatable structures were capable of meeting strict design requirements.

The IAE consisted of an inflatable structure which provided support for the reflector itself which was made from a gossamer material. Gossamer structures are made from materials that typically have a low areal density. Gossamer materials tend to have densities that in some cases are lower than 10 $\frac{g}{m^2}$. In comparison, the typical photocopy paper has a density of 80 $\frac{g}{m^2}$ (Lennon, 2008).

An important space structure that deals with gossamer structures are solar sails. Solar sail technology is seen by many to be a concept that could be used to propel spacecraft into space. In 2010, the technology was demonstrated on two separate space craft, NASA's Nanosail-D, and Japan Aerospace Exploration Agency's IKAROS (Anderson, 2011) (Small Solar Power Sail Demonstrator "IKAROS", 2012). The main benefit to using solar sails is they are able to provide spacecraft with an unlimited amount of propulsion, allowing for spacecraft to travel deep into space. Aside from being able to propel spacecraft further into space than ever before, one of the main goals of the Nanosail demonstration was to show solar sails could be used to deorbit decommissioned satellites. Upon re-entering earth's atmosphere, the satellite would disintegrate completely. This technology would help reduce excessive space debris. Since gossamer structures are being used, the deorbiting component of the satellite would not take up considerable room on spacecraft. This makes it an attractive feature to add to future spacecraft (Anderson, 2011).

One of the main design considerations in using solar sails is the amount of wrinkles that are present on the sails. Since scientists envision using solar sails measuring 328 feet or more on each side, this issue becomes a major design limitation. If wrinkles are present, the effects can be detrimental. Some of the effects include “non-concurrent centers of pressure and mass, reduced reflectivity, and non-uniform surface heating” (Leifer, J.; Belvin, W. K., April, 2003). Figure 5 shows a picture of a proposed solar sail. Notice that the sail is comprised of four individual triangular sails.

Figure 5: Solar Sail Measuring 33 ft. x 33 ft. (Jensen, 2004) (Image Courtesy of NASA)

Inflatable structures are not exclusively used in the aerospace industry. In the 1950’s, inflatable wings were introduced into the aviation industry when the Goodyear GA-33 Inflatoplane was built in 1956. The plane was designed to be dropped behind enemy lines to downed pilots. The plane was constructed from inflatable wings, and fuselage, while the landing gear assembly and engine were fabricated from rigid parts. The plane was able to be parachuted to a downed pilot in a single enclosure (Harris, 2011). The Inflatoplane can be seen in Figure 6.

Figure 6: Goodyear GA-33 Inflatoplane (Jacob, Smith, Cadogan, & Scarborough, 2007) (Used with Permission)

In a recent study, the durability of inflatable wings was shown. In approximately 300 flights using inflatable wings on UAVs, the wings never needed to be repaired or replaced (Simpson, 2008). A chart comparing the survivability of key components on UAVs tested can be seen in Figure 7.

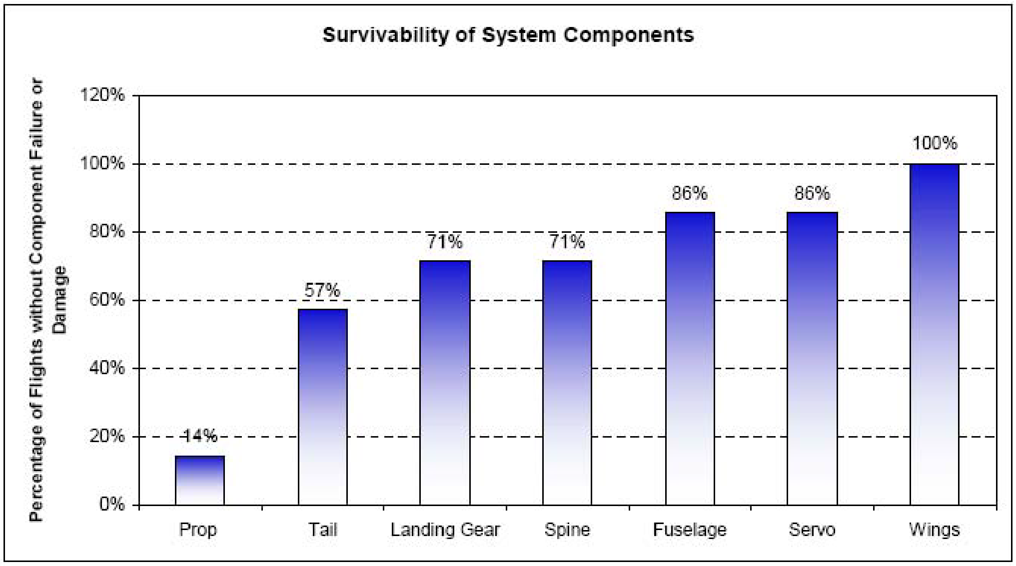

Figure 7: Survivalbility of Components on UAVs (Simpson, 2008) (Used with Permission)

Another incentive for using inflatable wings on a UAV is the packing efficiency. There has been recent research in the field of finding an optimal packing configuration for certain geometric shapes and conditions. In the paper (Harris, 2011), a computer program was developed that allowed users to run a simulation to see how large of wing could fit into a given container, and in a separate simulation, the users were able to calculate the packed volume of a wing with no packing restrictions. The simulation did allow a few variations to be entered, such as different wing designs and different types of materials. Although there were limitations with the simulations, it does give users a more accurate estimation for stowed volumes, and gives guidance on how to pack a material most efficiently.

2.2 Measuring Geometric Surfaces

Using large, light-weight structures in space is a very attractive since they possesses great advantages compared to their mechanical counter-parts. These light-weight structures can be used in a wide range of applications such as large antennas, observatories, solar sails, trusses and inflatable habitats (Pappa, Black, & Blandino). In most applications, the inflatable structures need to have very precise and accurate surface requirements. Table 2 shows various geometric requirements for inflatable systems. In regards to the radar reflector, the reflectors are designed to be an effective decoy with frequencies ranging from 10-40 GHz. (Foch, 2011)

Table 2: Geometric Requirements (Fulcher, 2012) (Used with Permission)

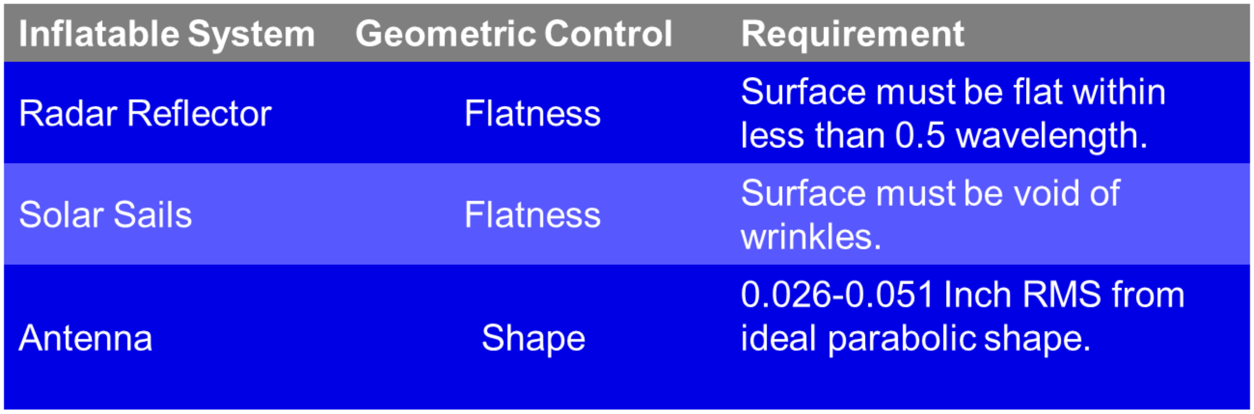

Inflatable System	Geometric Control	Requirement
Radar Reflector	Flatness	Surface must be flat within less than 0.5 wavelength.
Solar Sails	Flatness	Surface must be void of wrinkles.
Antenna	Shape	0.026-0.051 Inch RMS from ideal parabolic shape.

Due to strict geometric requirements, there needs to be an effective way to measure the inflatable surfaces. Commonly two types of measurements are used when it comes to light-weight structures. Capacitance or photogrammetry measurements are used since the materials being dealt with have low mass, and are flexible. These two types of measurements were compared in (Dharamsi, Evanchik, & Blandino, April 22-25, 2002). Capacitance measurements are a good way to test many materials but since the sensors are designed to work on metallic surfaces, a thin, 0.00004 inch thick aluminum coating must be put on one side of the material. This step takes time and slightly changes the material properties of the material. Another drawback of this type of measurement is that it is not a true non-contact measurement. Therefore, the sensor must come into contact with the surface which may affect the results. Benefits of this type of measurement include it being highly repeatable, and in addition the sensors are able create a high resolution model since it is able to measure a key point every 0.0031 inch^2.

Alternatively, the other type of measurement technique is photogrammetry which is a true non-contact type of measurement. Photogrammetry is the science of taking multiple pictures from different locations and using triangulation to compute the 3D location of key points. A commonly used program that is based upon photogrammetry is PhotoModler 6. According to (Thota, Leifer, Smith, & Lumpp, January, 2003), there are 8 steps to precisely and accurately locate the position of key points:

1. Establish accuracy requirements.
2. Calibrate cameras.
3. Photograph key points from multiple positions.
4. Transfer photos from camera to computer.
5. Mark key points on the photos.
6. Identify points in each image that refer to the same physical points on other photos.
7. Process the data.
8. Export results.

Incorporated in step 7 is where the 3D model gets scaled. This is where the user defines the distance between two key points, therefore allowing the software to compute distances between any two key points.

In the experiment conducted in (Dharamsi, Evanchik, & Blandino, April 22-25, 2002) the two different methods measured a 19.69 inch x 19.69 inch x 0.000098 inch membrane made from Kapton®. The material was then loaded at the four corners with different weights. Overall the photogrammetry software was able to accurately measure key points on the material and produce measurements that were comparable to the capacitance sensors. Although photogrammetry was able to accurately measure all points on the material, the method was only able to measure key points every 0.0248 inch^2 which is considerably less when compared to the capacitance resolution of key points every 0.0031 inch^2. When looking at the time it took to produce results, the photogrammetry software was able to obtain and process the data in about 1.5 hours compared to the 10-12 hours which was the time it took the capacitance sensors to measure the 19.69 inch square (Dharamsi, Evanchik, & Blandino, April 22-25, 2002). Overall since the photogrammetry is able to provide excellent results and take a fraction of the time, it makes using photogrammetry an attractive choice when measuring inflatable structures.

To improve on the results obtained by using photogrammetry, users have relied on projecting targets onto the material using a high intensity projector. This allows for a higher resolution model to be created since you can project a dense point cloud onto the material if desired. Figure 8 shows 5,000 targets being projected onto a 6.45 foot^2 material.

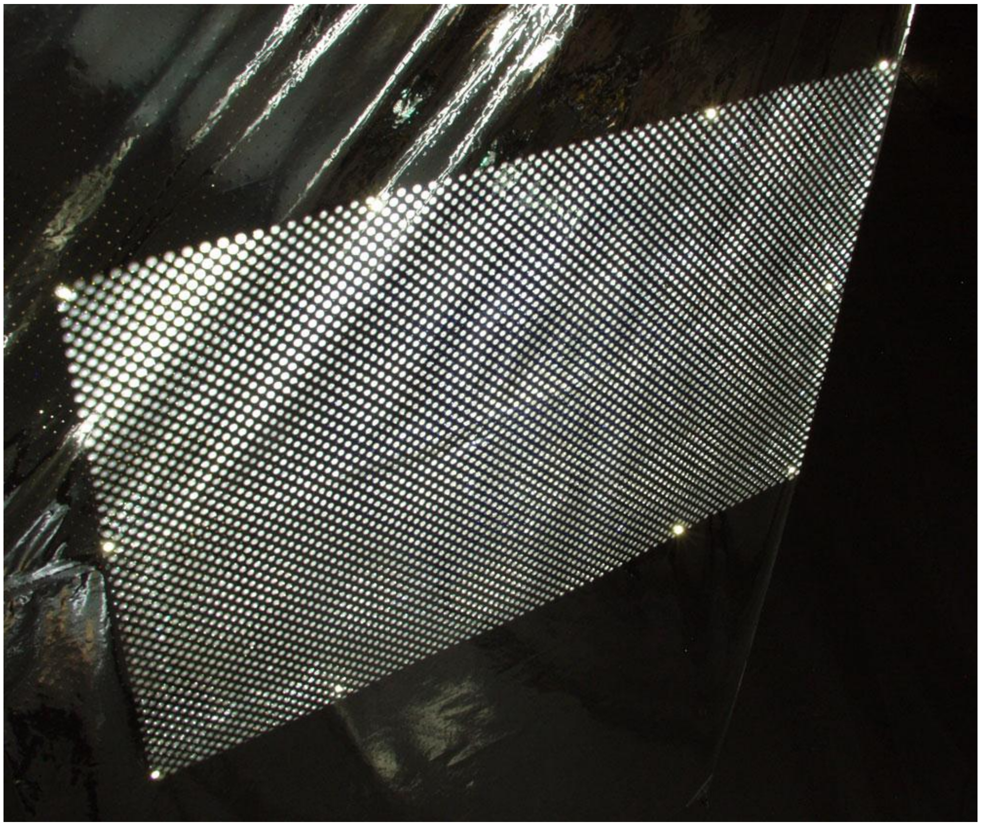

Figure 8: Projected Targets on Fabric (Pappa, Black, & Blandino) (Used with Permission)

There are a couple of distinct advantages to having targets projected onto the material by projectors. The first reason is that they add no mass or stiffness to the material. The second reason is that you are able to produce a 3D model with hundreds or even thousands of targets allowing for a higher resolution model. However, this method does have a few drawbacks. If the material is not perfectly flat, then the projected targets will not be perpendicular with the test article, and therefore the targets will be elliptical which reduces the accuracy of photogrammetry. Another downside is that this method has difficulties when dealing with materials with reflective surfaces such as Kapton®. As a result, the light intensity varies across the material thus reducing the accuracy of the analysis (Pappa, et al., 2003).

An alternative to using dot projected targets is available. Many have found using retroreflector targets to be the “gold standard” targeting method (Ganci & Brown, 2000). Retroreflective targets reflect light strongly back to the source of the light and appear as bright white dots (Pappa, et al., 2003). Just like using dot projection, there are advantages and disadvantages. Using Retroreflective targets provides excellent contrast between the target and test material and therefore substantially increases the accuracy of photogrammetry. Additionally the targets are able to be illuminated by the camera’s flash from long distances making it ideal for measuring large inflatable structures. Some disadvantages of retroreflectors are that the targets have to be manually placed on the test article, therefore it is not capable of producing the same resolution as dot projection. There is an additional mass and stiffness added to the test specimen from the reflectors as well. Additionally, if any of the dots need to be removed, it could damage thin materials such as Kapton® upon removal (Pappa, et al., 2003).

2.3 Improving Geometric Control of Surfaces

Being able to measure geometric surfaces accurately allows for research into how to effectively control the geometry of gossamer structures. Since there are many negative effects of having wrinkles present, avoiding them is a high priority. One idea that has shown positive effects in reducing wrinkles is using shear compliant borders. Incorporating a shear compliant border does not allow shear stress to cause the fabric to buckle and therefore the amount of wrinkles present is reduced (Talley, et al., April, 2002). Figure 9 shows the effectiveness of shear compliant borders. It can be seen that when shear compliant borders are incorporated onto the material, the wrinkling amplitude is decreased as well as the amount of wrinkles near the border where the shear stress was induced.

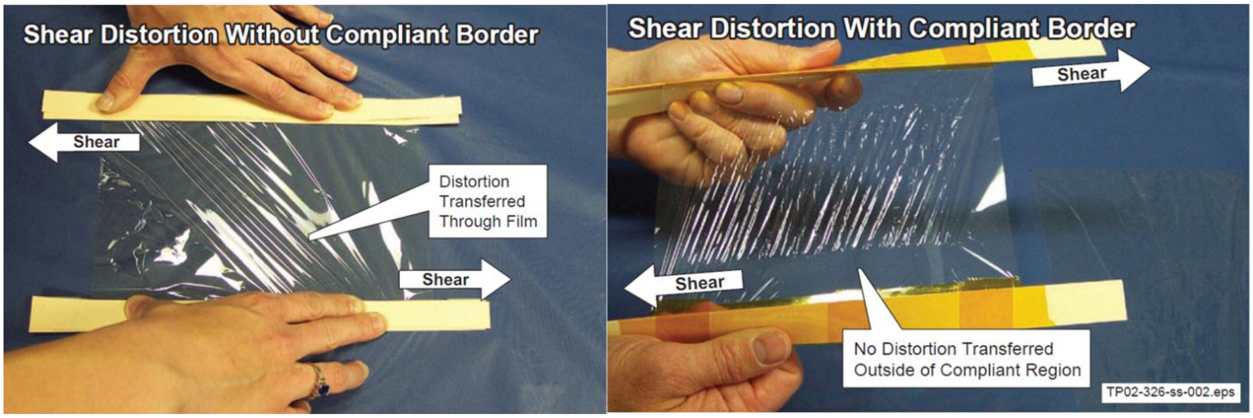

Figure 9: Shear Compliant Border (Talley, et al., April, 2002)(Used with Permission)

Using the shear compliance design can be implemented into creating gossamer structures such as solar sails and reducing the amount of wrinkles present and ultimately increasing the effectiveness of the propulsion system. Figure 10 shows a design in which a shear compliance border is incorporated into the solar sail design.

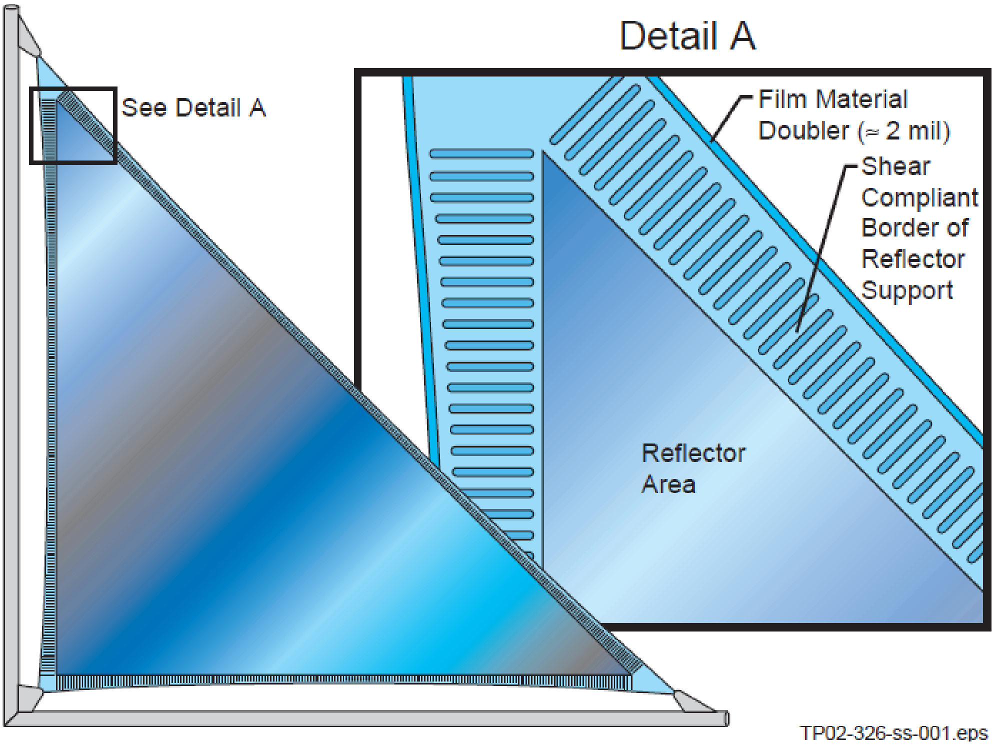

Figure 10: Catenary Cable Design (Talley, et al., April, 2002)(Used with Permission)

Incorporating the catenary design into the solar sails allows for a uniformly distributed load to be applied to the all three of the edges of the sail while only applying forces at three points.

Alternatively changing the material properties has been considered to improve effectiveness. Using additives to existing films has become a promising area of research to combat wrinkles. The concept behind the design is that the sail material is coated with an additive that has a melting point below that of the sail. Once the additive is exposed to solar heat, the additive melts off, causing the sail film to shrink. Currently there are films that will de-wrinkle on their own when exposed to extreme heat, but these types of materials need to be close to the sun to achieve the high temperatures necessary. Advances in material additives will allow for the sail to use coatings at much further distances away from the sun (Talley, et al., April, 2002).

Chapter 3 PhotoModler

3.1 PhotoModler Introduction

As previously seen with Table 2, which has been reproduced below for convenience, certain applications require a high level of precision in construction. Due to the high level of precision, these applications also require an accurate way to measure the surface geometry of the inflatable structure to ensure specifications are met.

Table 2: Geometric Requirements (Fulcher, 2012) (Used with Permission)

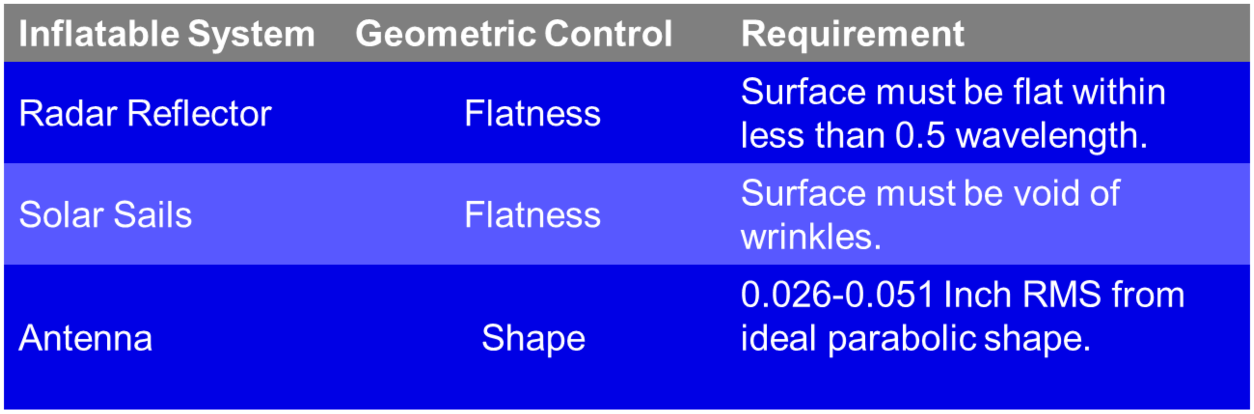

Inflatable System	Geometric Control	Requirement
Radar Reflector	Flatness	Surface must be flat within less than 0.5 wavelength.
Solar Sails	Flatness	Surface must be void of wrinkles.
Antenna	Shape	0.026-0.051 Inch RMS from ideal parabolic shape.

A technology that has been used in the past to measure high precision inflatable surfaces is the method of photogrammetry. Photogrammetry, as discussed previously, is the science of taking still images and using triangulation to create a 3D model. Currently there are different commercial softwares available that use photogrammetry as the basis behind their product. Once such software is PhotoModler 6. PhotoModler has been discussed in previous literature and has been identified as software that is capable of accurate measurements. The main question faced in using the software was how accurate the measurements were with the current available resources. In Table 2, the requirements for a measurement system are given. Not only should PhotoModler be able to meet these specifications, PhotoModler should be able to have an accuracy level that is considerably more strict than the project standards in order to ensure that the requirements for the project are met. PhotoModler therefore needs to be able to measure RMS values with an accuracy of less than 0.026 inches. In regards to the requirements set for the radar reflector, PhotoModler needs to have an accuracy of less than a half wavelength of a given frequency. For example, a half wavelength for a 40 GHz. wave is 0.148 inches. PhotoModler states in its help section that the software is able to measure with an accuracy of up to $\frac{1}{30{,}000}$ of the largest dimension. If the largest dimension in a project is 10 inches, the accuracy is stated to be $\pm \frac{10}{30{,}000}\, inches$ (±0.00033 inches). Although this accuracy would meet the requirements set for this project, this is the best accuracy that the program can achieve. To see if the current capabilities at the University of Kentucky are able to meet these standards an investigation was required.

3.2 PhotoModler 6 Study

To determine the accuracy that is able to be achieved using PhotoModler 6 with current resources available, the following components were used:

- Canon A580 PowerShot Camera 8 MP
- Kinetic Systems Optical Table Model: 5208-4896-22
- Camera Tripod Sunpak Ultra Pro 777B

The experimental set-up can be seen in Figure 11.

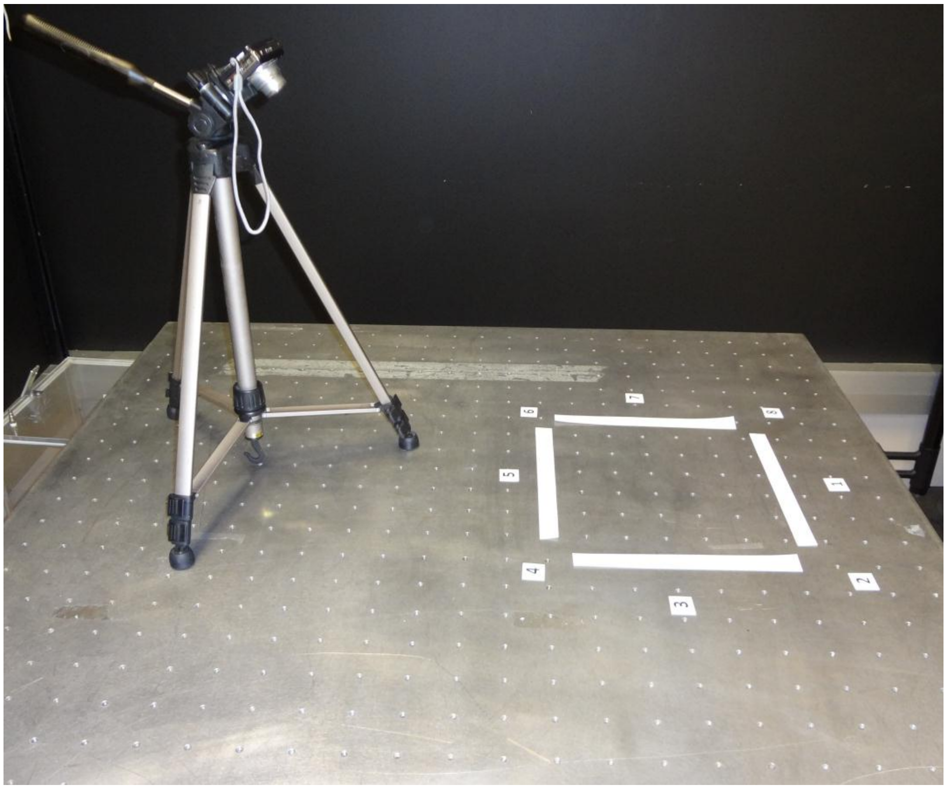

Figure 11: PhotoModler Experimental Set-Up

To obtain the best results, each photo should be taken 90^o apart from one another. Therefore positioning the camera at a 45^o vertical angle will create a 90^o vertical angle with other photos. This will inevitably improve the accuracy of the model. The camera's vertical position can be seen in Figure 12.

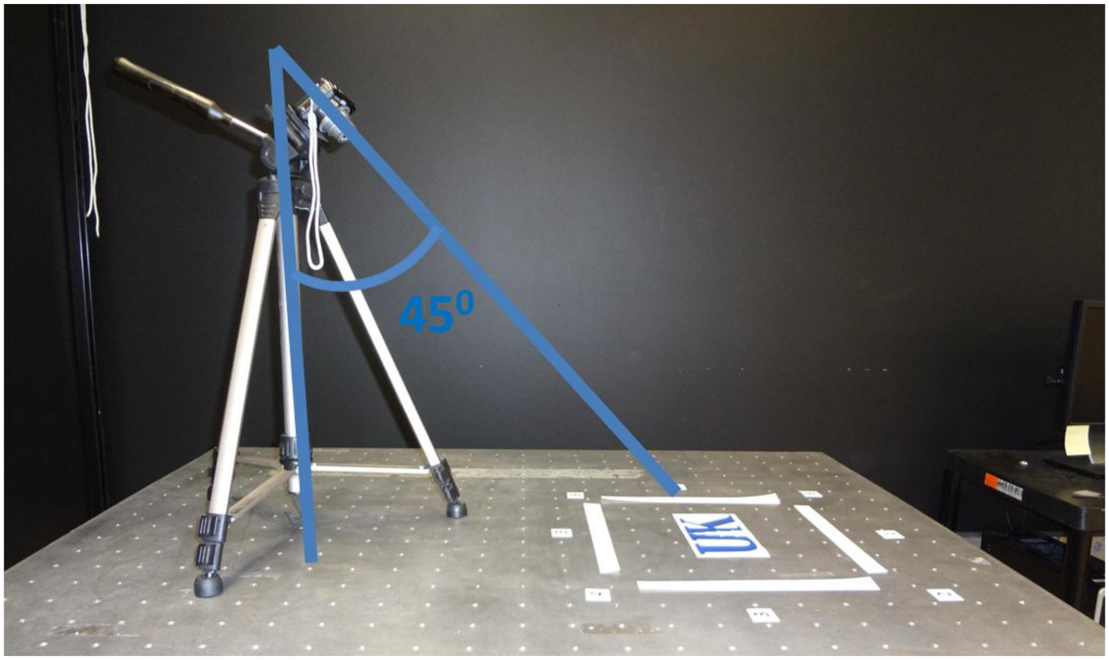

Figure 12: 45 ^{o} Vertical Angle Camera Position

In the investigation, pictures were taken referencing 36 key points. The points that were referenced were spaced 2 inches apart from their neighboring points. Since the goal of the study was to determine the accuracy of our current capability, PhotoModler needed to be able to compare its measurements to known measurements to be able to determine the error in the system. Thus the more accurate the known locations are the more accurate of an error can be obtained. For this reason an optical table was used and the tapped holes were used as key points since the manufacture states that all the holes were manufactured to be evenly spaced by 2 ±0.005 inches apart from one another (Shaver, 2011). Another benefit from determining the accuracy of the system was to learn how to use PhotoModler as well as learning the processes needed to create an accurate model.

Although having the holes accurately spaced was a benefit of using an optical table, the down side of using tapped holes as reference points is that the PhotoModler software may calculate the key point locations to be submersed in the hole, when ideally the software would calculate the key point location to be flush with the surface of the table. But since the hole spacing had such a tight tolerance, it was determined that the tapped holes would still make good reference points. The test created a model using all 36 points within the white square as seen in Figure 13.

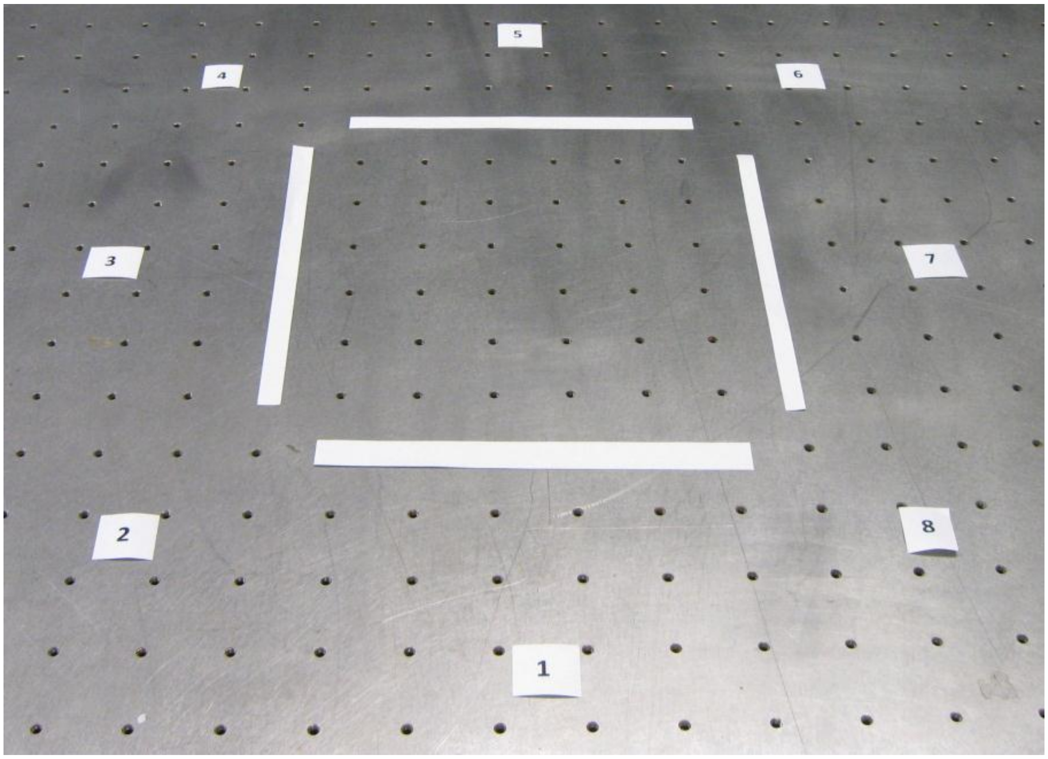

Figure 13: PhotoModler Study Setup

In addition to testing the accuracy of the system, the study had two other objectives. The first was to see how many photos were required to meet the accuracy requirements for inflatable structures. The study examined seven different models each of which were made using different number of photos. The seven models were created using 2,3,4,5,6,7,8 photos.

PhotoModler states that the more pictures that are present in producing the model, the more accurate the results will be. The main reason to examine how many pictures are needed to create an accurate model was that even though more photos may yield a more accurate model, using eight photos may be an excessive use of time since the accuracy requirements may be met with using just two or four photos. Since it takes less time to take and process four photos when compared to eight, it would be ideal to know if and when PhotoModler meets the requirements of the project.

The locations of where the photos were taken can be seen in Table 3. Figure 13 shows the physical camera positions labeled on the optical table. In the study, a total of eight pictures were taken at different locations around the 10x10 inch square. Since only eight photos were used, some photos were used in multiple models. Different combinations of photos were then used to create models. For example the photo that was taken at camera position 1, was used in all seven cases. The photos were all taken at approximately 36 inches away from the points located in the square.

Table 3: Camera Locations

Number of Photos Used	Camera Position
2	1,5
3	1,4,6
4	1,3,5,7
5	1,2,4,6,8
6	1,2,4,5,6,8
7	1,2,3,4,6,7,8
8	1,2,3,4,5,6,7,8

To understand where the camera positions were located, Figure 14, and Figure 15 can be referenced. In the figures, a number is circled designating the position of where the photo was taken from. A University of Kentucky logo has been place in the center of the square to help orient the location of where the photos were taken.

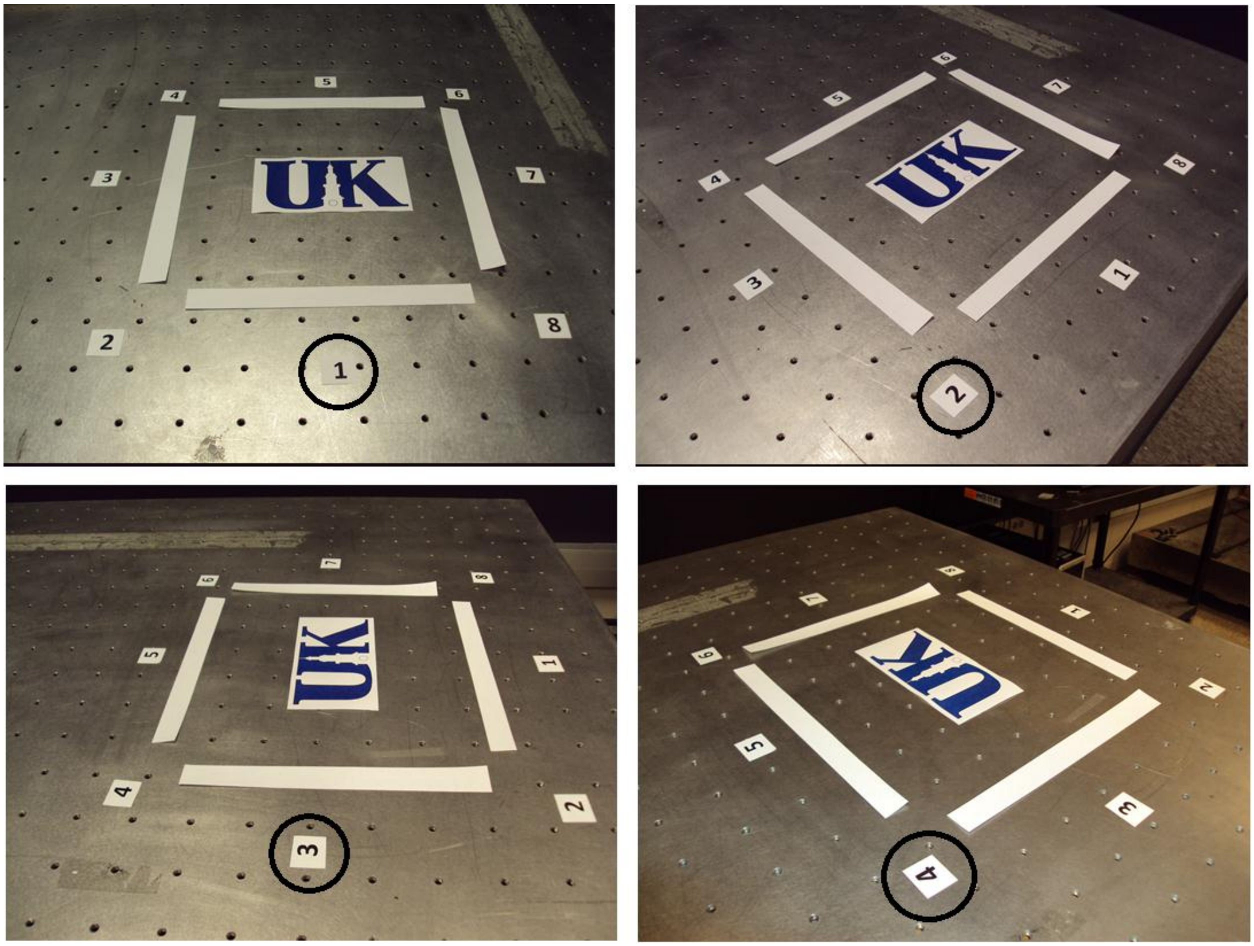

Figure 14: Camera Locations

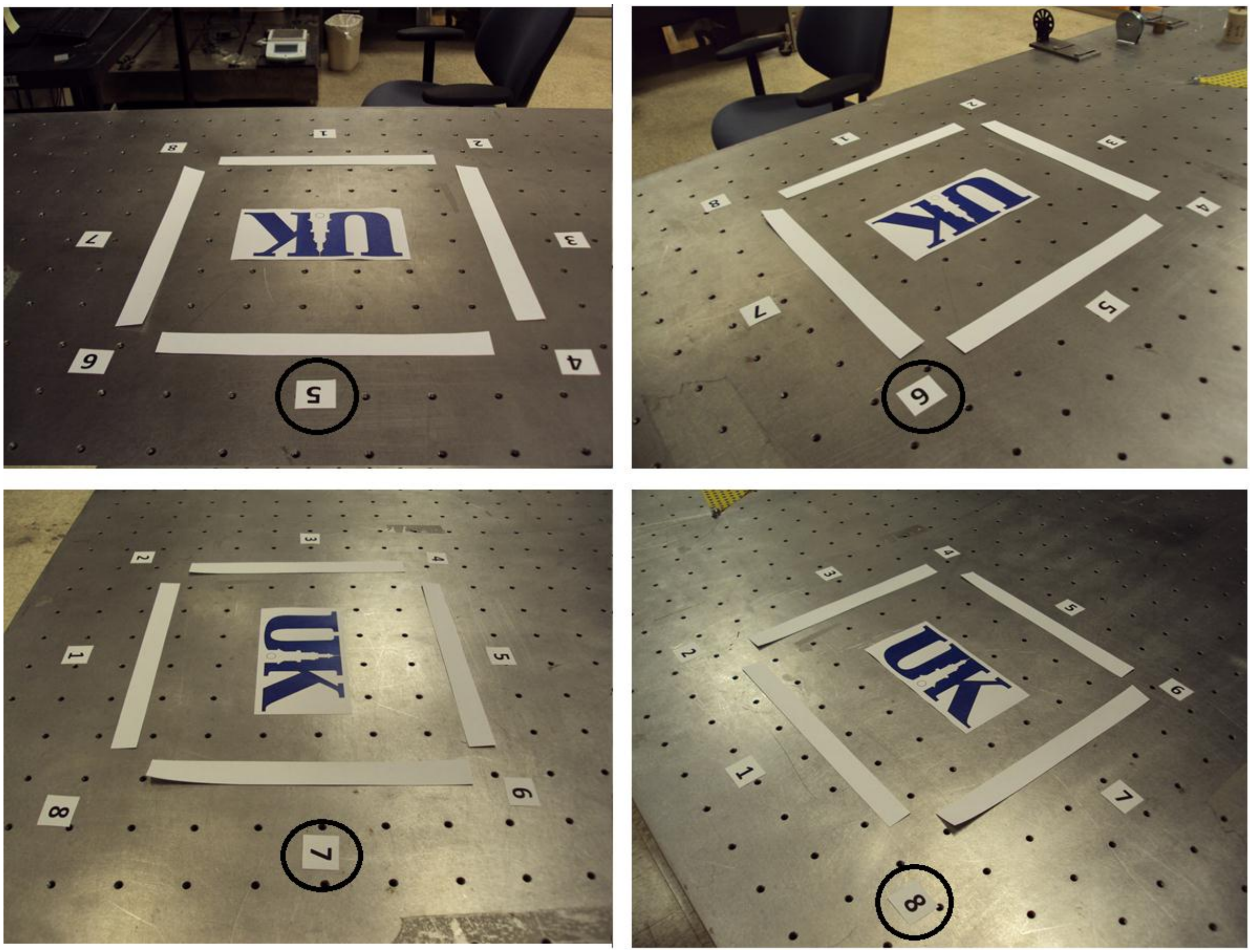

Figure 15: Camera Locations

Another component that may affect PhotoModler accuracy is which two points are used to scale the model. PhotoModler requires users to input the distance between two key points. This allows for the software to then be able to scale the project to the correct dimensions. To get an understanding of which points should be selected to obtain a more accurate model, two separate pairs of points were used to scale the model. PhotoModler gives some insight in how to pick these points that are used to scale the project. Generally it is recommended that the two points selected should not be close together relative to the overall project dimensions. If the two points that are selected are close to each other, and the scale that the user manually inputs is incorrect by a small amount, later when a large distance is measured using the scaled model, the small error will be amplified. In Figure 16, the two different sets locations used for scaling can be seen circled.

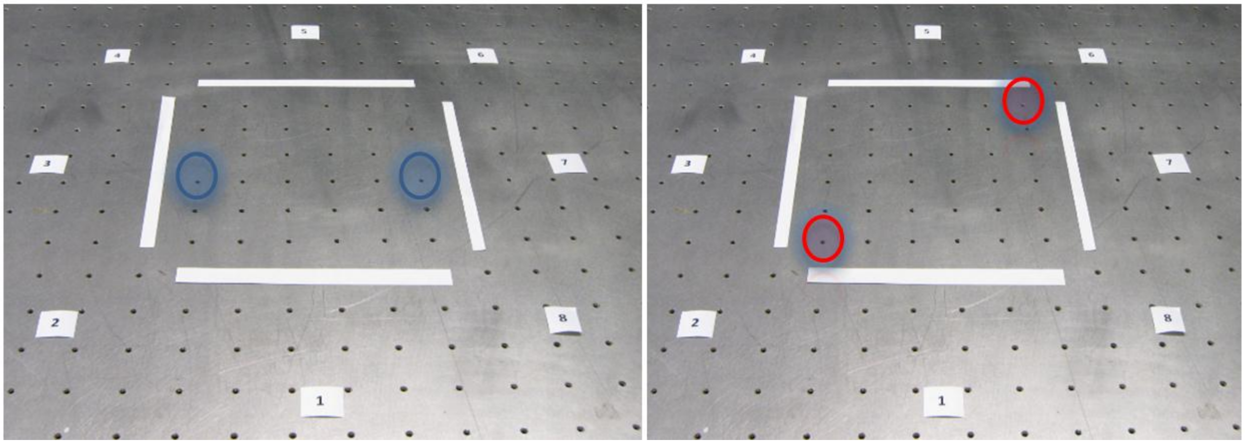

Figure 16: Point Locations Used for Scaling

The image on the left scales the model using the two points strictly on the x-axis, directly in the middle of the square, while the image on the rights used two points at a 45^{o} angle above the x-axis and the points are located in the lower left and upper right corners of the square.

Once the camera position was set to a 45^{o} vertical angle, eight pictures were then taken of the 10x10 inch square. Since there were seven different tests being completed, using two different points to scale the model, a total of 14 models was created. For a visual representation of Table 3, we can refer to Figure 17 and Figure 18. In the figures, we can visually see the points located referenced using PhotoModler as well as the camera's locations.

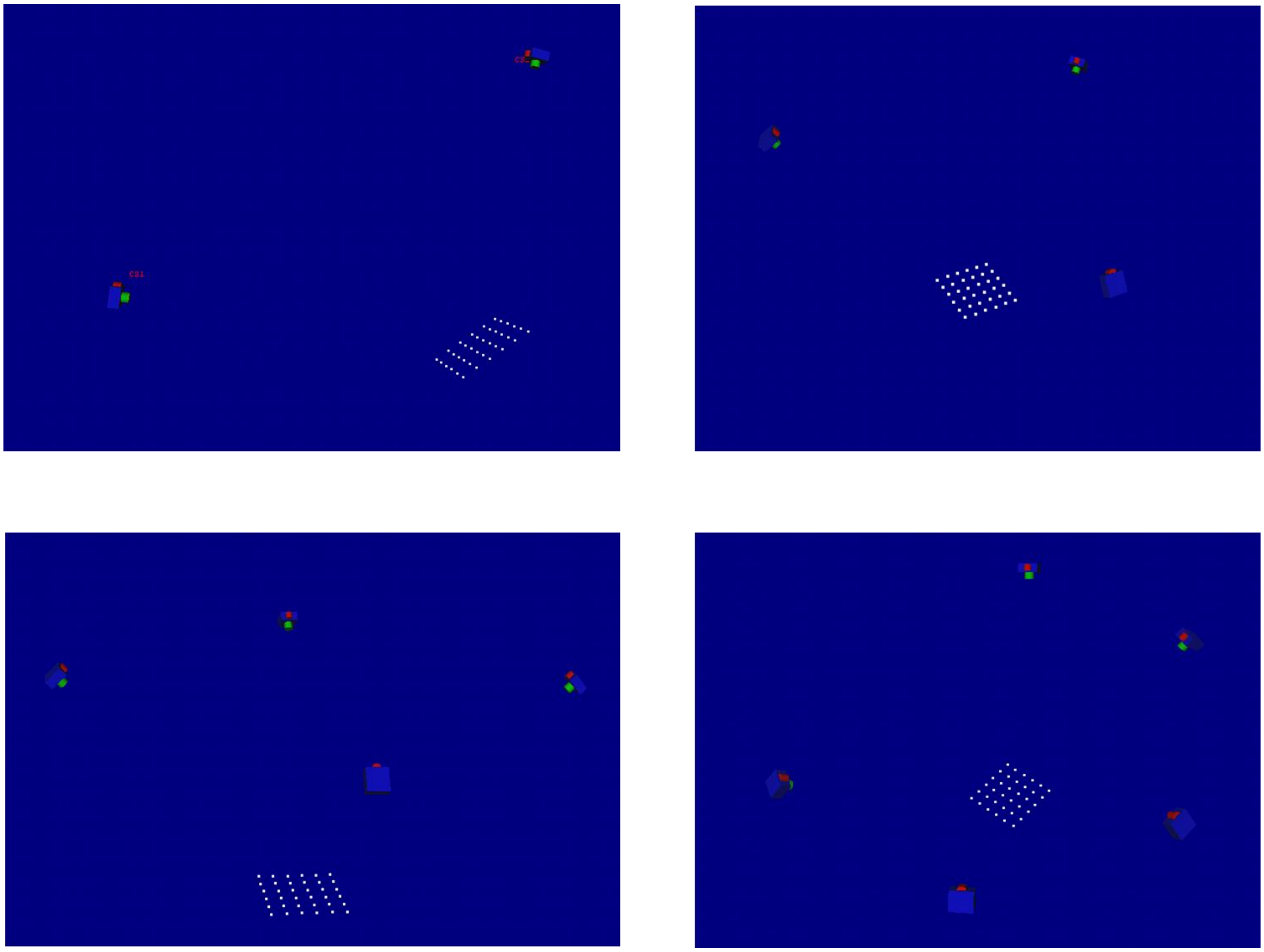

Figure 17: Camera Positions Using 2-5 Photos

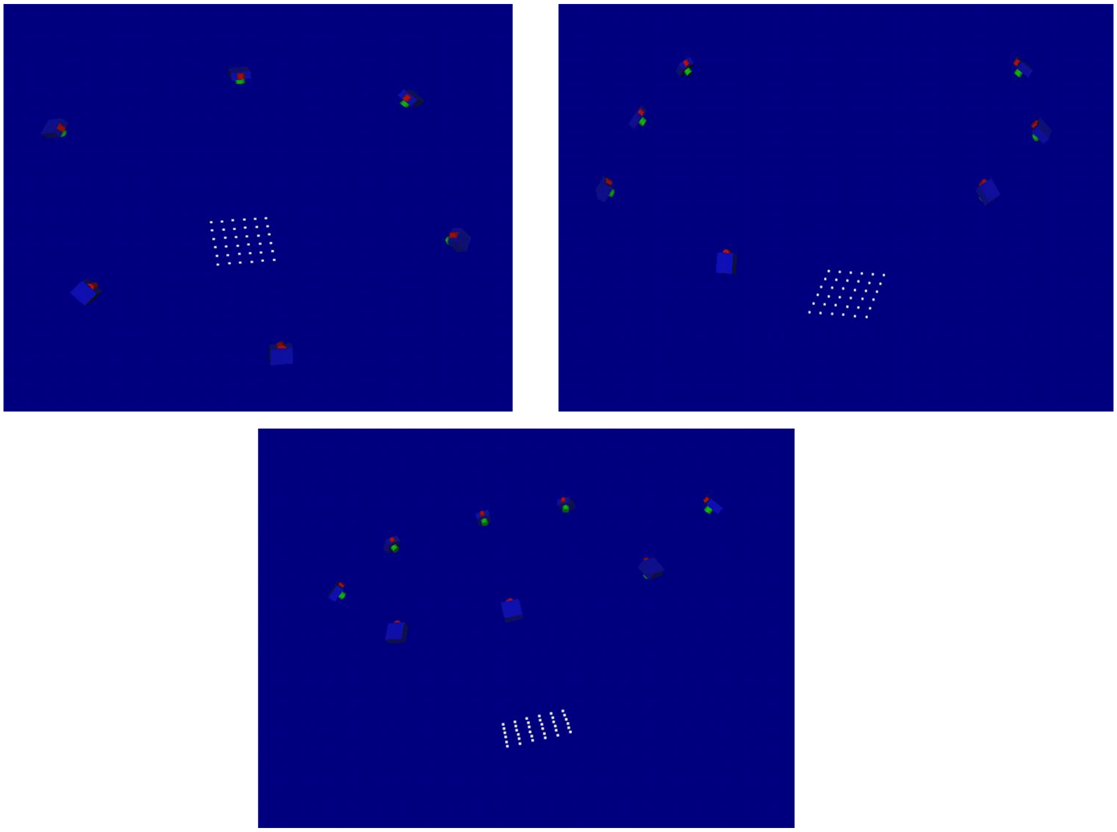

Figure 18: Camera Positions Using 6-8 Photos

3.3 PhotoModler 6 Study Results

After the seven different models were created in PhotoModler and the photos were scaled using the two different scaling locations, the software was able to output the location of all points in the model. Since the tapped hole's locations were known to be evenly spaced apart from each other by 2 inches, the distance between any two points was able to be measured and then compared to the known location between the tapped holes. In this study, it was decided that to find an error, the distance between each neighboring hole was going to be assumed to be "exactly" 2 inches, even though the manufacture states that the holes had a ± 0.005 inch tolerance.

PhotoModler was then able to measure the distance between two reference points. All points that were 2, 4, 6, 8, and 10 inches apart were taken into account and compared to the actual length using the tables manufacture's specifications. The absolute value of the difference of these two distances is going to be considered the error in this study. Seen in Figure 19 is a graph that represents the trend that was present in all of the results produced. In this particular figure, PhotoModler measured all 4 inch distances between key points within the square and the error was calculated.

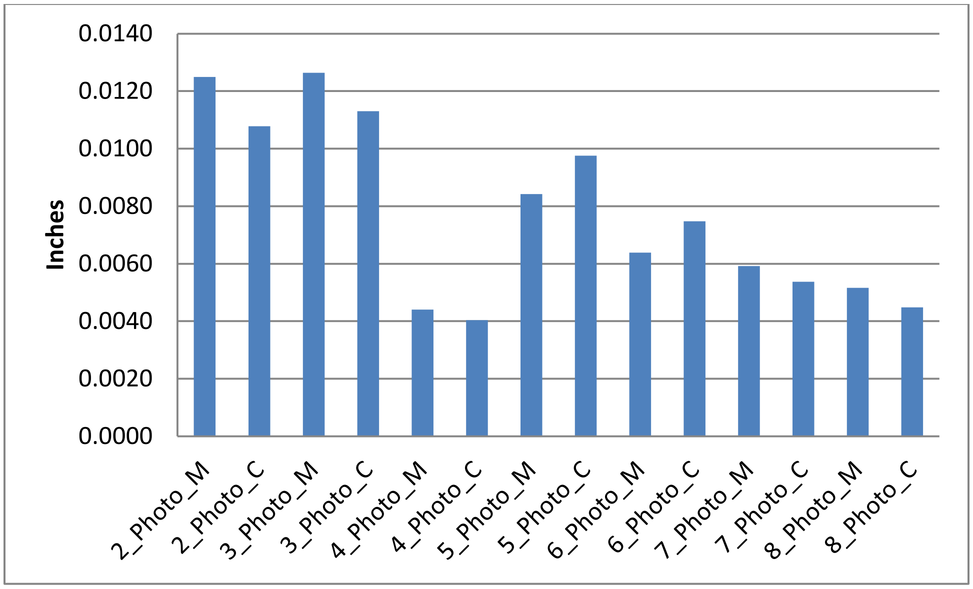

Figure 19: PhotoModler 4 Inch Error

In Figure 19, the horizontal axis shows how many photos were used to develop a model, as well as which two points were used to scale the model. The M and the C designates which two points were used to scale the model. The "M" stands for middle and uses the two points that are located 0^o from the x-axis. The "C" stands for corner since the two points were located in the bottom left and top right corner and uses the two points that are located 45^o above the x-axis. For example, in the case where it refers to 4_Photo_M, four photos per Table 3 were used to create the model, and the two points used to scale the photo were in the middle of the square.

The vertical axis represents the average error between the distances calculated by PhotoModler and the actual distance between two points. The error is calculated using equation 1. n represents the total number of distances measured.

$$\boldsymbol{Error = \frac{1}{n} * \sum_{i=1}^{n}(|PhotoModler\ Distance - Actual\ Distance|)} \quad (1)$$

When the error was calculated for reference points spaced 10 inches apart, Figure 20 was obtained.

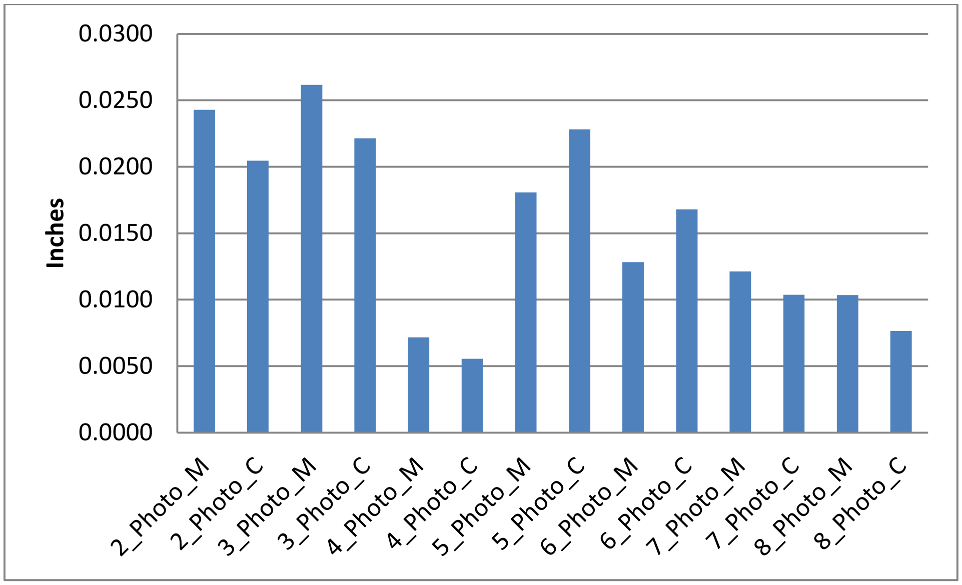

Figure 20: PhotoModler 10 Inch Error

When Figure 19 and Figure 20 are compared it is evident that there are similarities that exist. In both cases, the graphs follow the same overall trend. In both, the error is largest when only two and three photos are used and lowest when four photos are used to create a model.

Then when five photos are used to process the project, the error increases and then this is followed by an overall decrease in error when additional photos are introduced in creating the model. Although the overall trend is similar, when 10 inch sections were measured, the error substantially increased when compared to when only 4 inch sections were measured. For instance, the error associated with 2_Photo_M when 4 inch segments are measured is 0.0125 Inches. Now if we look at the error associated with 2_Photo_M for 10 inch sections, the error measures 0.0243 Inches. The only thing that is different between these two results is the distance measured. The distance measured went from 4 Inches to 10 Inches. Graphs containing 2, 6, 8 Inch error can be found in Appendix A.1 PhotoModler Error.

Additionally we can visually see the error obtained using PhotoModler and compare it to our requirement of being a λ/2 of the desired frequency range in Figure 21.

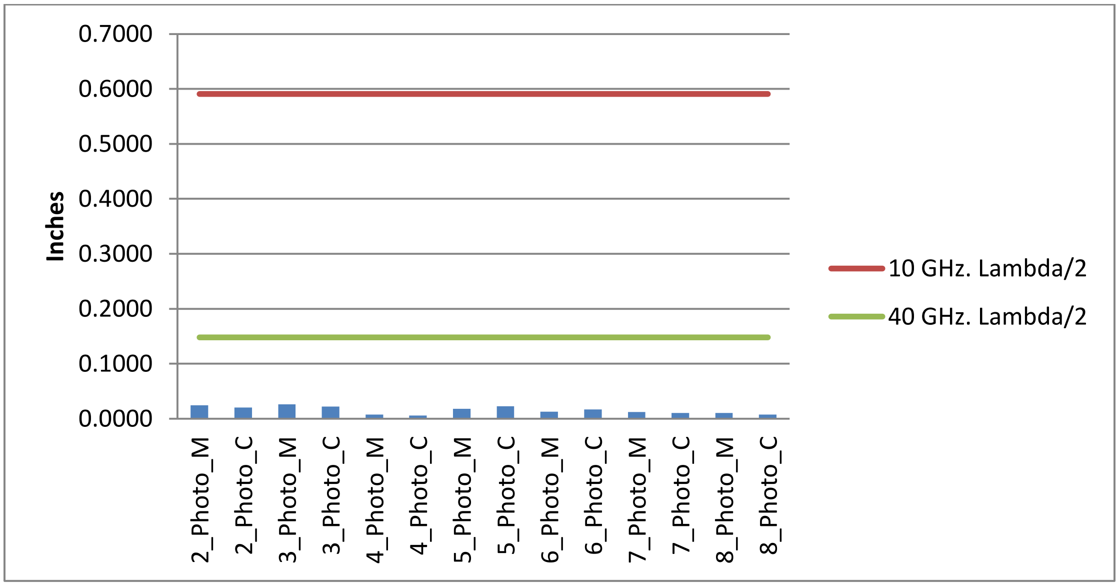

Figure 21: PhotoModler 10 Inch Error with Upper and Lower Bound Requirements

The frequency range desired for radar reflectors ranges from 10-40 GHz. Since the λ/2 for the 40 GHz. waves is smaller than the λ/2 of a 10 GHz. wave, the focus will be if the error is below the λ/2 for the 40 GHz. waves. As can be clearly seen, the error associated with PhotoModler is substantially within the tolerance requirements. Since most error occurs when measuring the largest distance, which is 10 inches, it can be concluded that all measurements meet the λ/2 for the 40 GHz. wave requirements.

Furthermore the data obtained can be normalized to further understanding. If we normalize the calculated errors with their respective length measured using equation 2, we obtain Figure 22.

$$\text{Normalized Error} = \frac{\text{Average Error Measured}}{\text{Known Dimenstion}} \qquad (2)$$

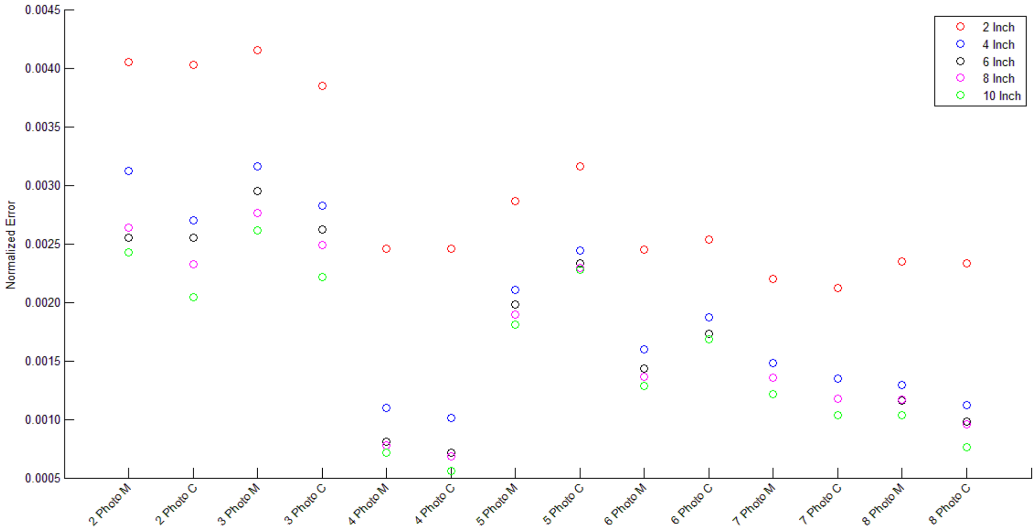

Figure 22: Normalized Error

The figure shows normalized error for all twelve cases. In the figure, it can be seen that when measurements are made using PhotoModler, the normalized error increases when smaller measurements are made.

The other requirement that PhotoModler must meet is having a RMS value of less than 0.026-0.051 Inches. Using equation 3, the average RMS values were calculated for their respective distances. The average RMS values when a 10 inch section was measured can be seen in Figure 23.

$$RMS = sqrt\left(\frac{1}{n} * \sum_{i=1}^{n}(PhotoModler\ Measured\ Distance - Average\ PhotoModler\ Distance)^2\right) \quad (3)$$

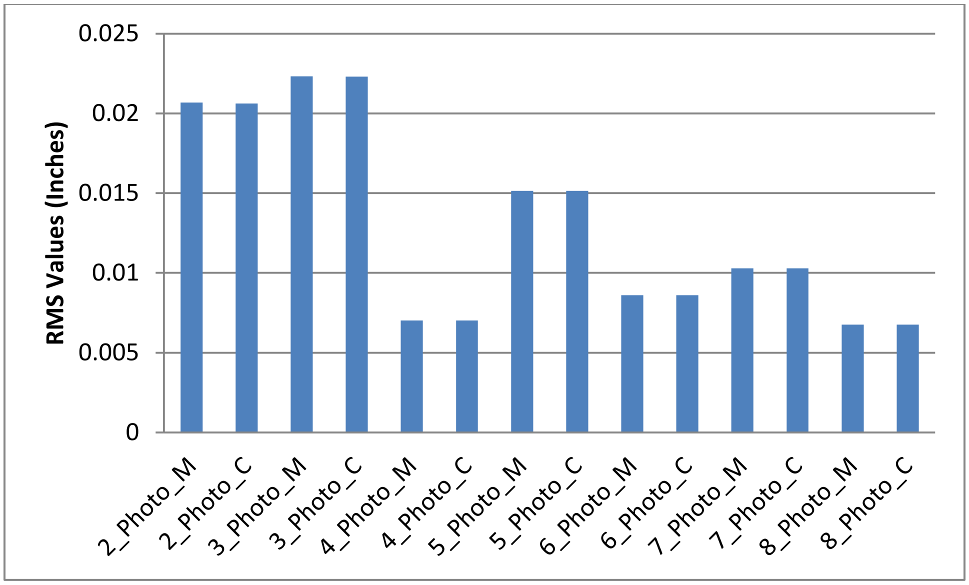

Figure 23: RMS Values For 10 Inch Segment

Figure 23 displays the same overall trend when compared with Figure 19. The RMS values are greatest when only two and three photos are used to create a 3d model and lowest when four photos are used to process the project. Furthermore we can compare the average RMS values obtained using PhotoModler and see if it meets the requirements. Other RMS graphs for the cases in which 2, 4, 6, 8 inch sections were measured can be found in Appendix A.2 PhotoModler RMS Values.

According to (Fulcher, 2012), some inflatable structures require an RMS value of 0.026-0.051 inches. When analyzing Figure 24, it is clear that PhotoModler meets this requirement. When two and three photos are used create the model, the average RMS values come close to exceeding the 0.026 inch requirement. When PhotoModler uses four photos to create the model, the average RMS values were calculated to be well under the 0.026 inch requirement.

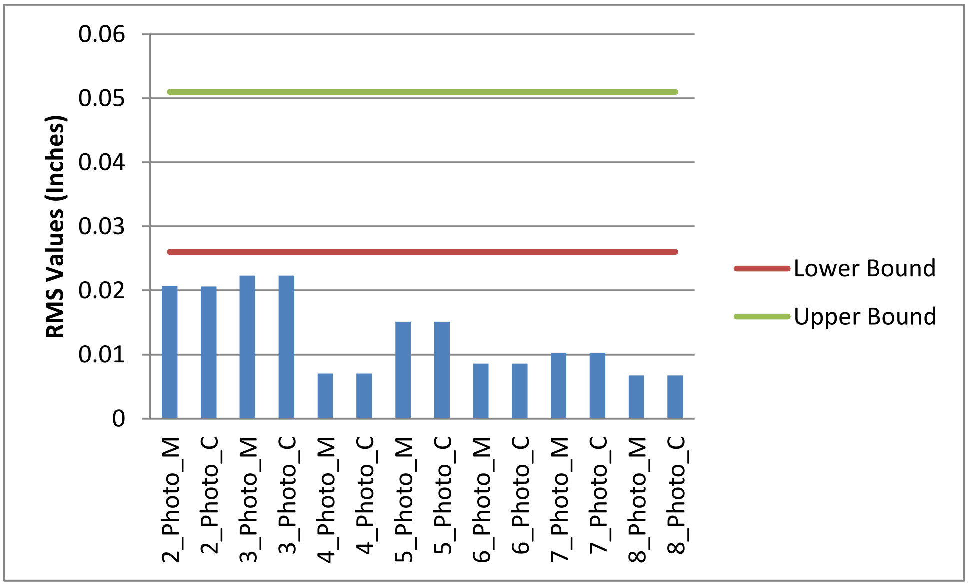

Figure 24: PhotoModler RMS For 10 Inch Segment with Upper and Lower Bounds

As stated previously, PhotoModler states to have accuracy up to $\pm \frac{1}{30{,}000}$ of the largest dimension. To see how the results compared with PhotoModler's specifications, the error calculated using 4_Photo_C was used. Case 4_Photo_C was used because the model produced the lowest error in all cases. Therefore the maximum accuracy produced in this study will be produced. Using this case, it was found that the accuracy was $\pm\frac{1}{1{,}800}$ of the largest dimension.

3.4 PhotoModler 6 Study Conclusions

After studying PhotoModler's capabilities, it was determined that using the software would provide an accurate way to measure the surface of inflatable materials. The error associated with the software was less than the λ/2 requirement as well as lower than the requirement to have a RMS value under 0.026-0.051 inches. Using two photos proved to be sufficient in creating a model while meeting the design requirements. However the most accurate model was created using four photos. Even though PhotoModler states the more photos present in a model, the more accurate the results will be, it is suspected that the most accurate model was made using four photos due to the orthogonality of the cameras to one another. The cameras were positioned 90^0 apart from each other in the horizontal plane as well as being 90^o apart from the camera positioned directly across from its position in the vertical plane. Since creating a model using four photos does not require a significant amount of more time to create a model, four photos were therefore used to create and process models.

Furthermore it was found that which two reference points were used to scale the model did not have a significant effect on the accuracy of the model. Even though different results were obtained when using different pairs of scaling points, not one pair of points used to scale the project consistently created more accurate results than the other. Therefore it can be assumed that which two points used to scale a project does not have a significant effect in the model's accuracy. Although when scaling a project, it is suggested to use the largest distance possible between two points to scale the project because having this long distance will mitigate small amounts of error.

Lastly, the error computed was significantly less than the maximum accuracy PhotoModler states. The accuracy calculated was $\pm\frac{1}{1,800}$ compared to PhotoModler's accuracy of $\pm\frac{1}{30,000}$. Although this number is significantly lower, the accuracy level exceeded all accuracy requirements for inflatable structures. It was suspected the reason for the relatively low accuracy was the key points measured by PhotoModler were not 2d objects. Therefore PhotoModler did not consistently measure the points to be flush with the table.

Chapter 4 Fixture Design

4.1 Test Fixture Introduction

The goal of the project was to be able to test multiple factors and examine their effect on the overall surface flatness of the test article. Three different factors were tested. The factors tested included, bi-axial force loading, boundary conditions, and fabric orientation. To effectively test these factors, a fixture was designed so the forces could be applied and the three factors tested. The fixture needed to be able to apply the forces to the fabric at the corners. Since the goal was to measure surface flatness, the location where the forces were applied all needed to be in the same horizontal plane. Having the forces applied on the same plane would allow for a conclusion to be made about which combination of factors would provide the best results. If the forces applied were all applied at different heights, no conclusion could be made on the best factor combination.

The test article was a triangular piece of fabric manufactured by ILC Dover. The material was made from nylon and was coated on both sides with a polyurethane coating. The shape of the test material can be seen Figure 25. The two legs of the triangle measured 9 inches while the hypotenuse measured 12.73 inches.

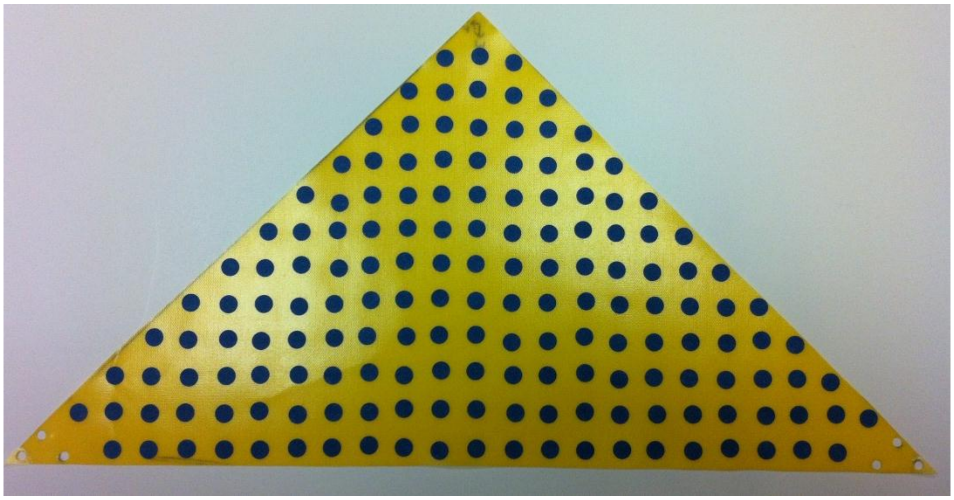

Figure 25: Test Material

The triangle tested had a 90^0, and two 45^0 angles. The “top” of the fabric was a 90^0 angle and the two “lower corners” had a measured angle of 45^0

4.2 Initial Fixture Design

One of the difficulties with using fabric as the test material was applying bi-axial forces to the material at its corners. One concept was to test surface deflection with an apparatus constructed on an optical table since its tapped holes would be useful for mounting and securing the apparatus. The initial testing fixture can be seen Figure 26. Red arrows have been overlaid in the picture to show where the forces are being applied, the direction of the applied forces.

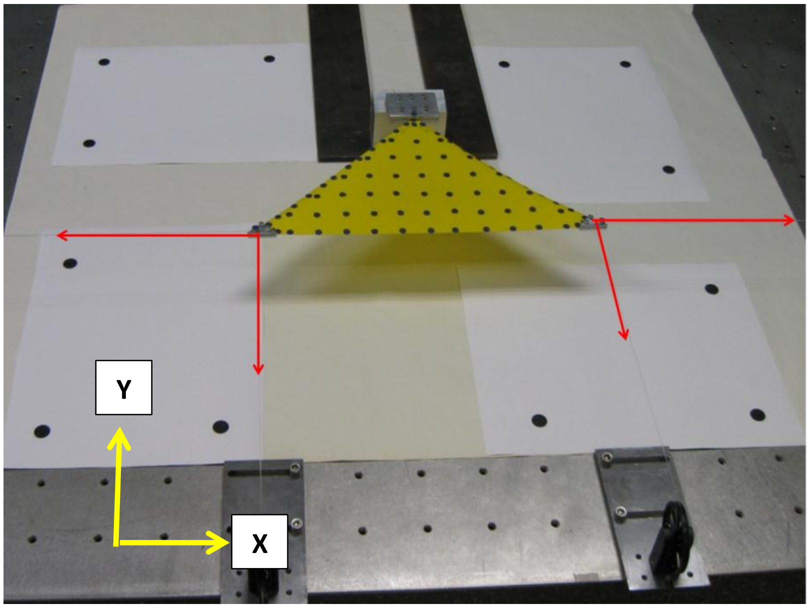

Figure 26: Initial Fixture Setup with Force Directions Shown

Not seen in the figure are two of the four pulleys. These pulleys are located to the left and right of the photo and are responsible for applying the forces in the x direction while the two pulleys seen in the figure apply forces in the y direction.

The concept first tested to apply forces to the corners of the fabric was to punch holes close to the corners of the triangle. Once the holes were made, fishing line could be attached and the forces could be applied. With the fishing line attached, the line would then run over a pulley to redirect the forces of weights that would hang off the optical table. Since the applied forces should be near the corner to accurately simulate the desired loading conditions, the attachment points easily tore the fabric when the forces were applied.

One novel approach to keep the attachment points from tearing was to use rigid clamps. The rigid clamps were designed in the shape of a triangle. The clamps were then attached to the corners of the material. The line was then attached to the rigid clamp and not directly to the fabric, and the tearing of the material did not occur. Although using a rigid clamp kept the material from tearing, this approach did add weight to the corner of the material.

Since the clamps were constructed from a metal, the weights of the clamps were an issue. To keep the weight to a minimum while still providing a significant clamping force, the fabric was clamped between two thin 0.125 inch pieces of aluminum that would be bolted together. Other than being made from a light weight material, the two legs of the triangular clamp measured only 0.75 inches in length to reduce its weight. In total each of the clamps weighed 0.009 lbs. One of the two clamps used to secure the corner of the fabric can be seen in Figure 27.

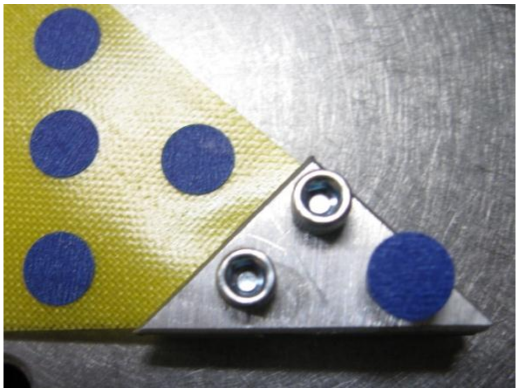

Figure 27: Rigid Clamp Design

Since PhotoModler was going to be used in measuring surface deflection, it was very important to be able to reference certain key points. Since clamps are being used on the fabric and consequently cover up the corner of the material as seen in Figure 27, a circular dot was placed on top of a bolt. This dot allowed for PhotoModler to recognize the circle as a key point and in turn able to measure its location. Both the bolts head, and clamp thickness were able to be measured, therefore the corner point of the material could be accurately determined.

When designing the fixture, only the lower two 45^0 corners needed to have a bi-axial forces applied to be able to maintain tension in the fabric. For this reason the material was fixed in all directions at the 90^0 corner. The clamp can be seen in Figure 28.

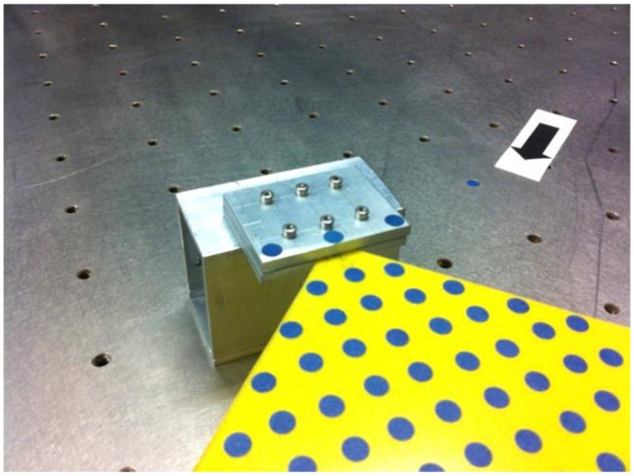

Figure 28: Fixed Clamp Setup

To be able to measure the surface contour of the material, circular dots were placed on the triangle and were evenly spaced 1 inch apart. These would serve as the key reference points allowing PhotoModler to be able to automatically locate the points on the fabric. Although using projected dots or retro-reflective targets would create a more accurate model, it was determined from the previous study that the current set-up was accurate enough to effectively create the 3D model.

Since the main goal is to measure surface deflection of the triangular piece of fabric, one of the main requirements is that all the forces be applied to the fabric in the same horizontal plane. If this requirement was not met, the results of the experiment would not provide useful information. The height at the top of the four pulleys measured 2.3125 inches which was the same height as the fixed 90^0 corner. It was assumed due to the light weight of the two clamps, that the clamps would remain at the same height as the fixed clamp location.

Other components used are the pulleys and pulley mounts. The pulley mounts attached the pulleys to the optical table. Additionally, the pulley mounts had channels milled into the metal to allow movement from side to side. Since we wanted to be able to apply a bi-axial force to each clamp, this allowed for each pair of forces from a single clamp to be perpendicular with one another. Another component affecting the accuracy of the experiment involved knowing the forces applied to the material. If the pulleys do not provide friction free rotation, then once weights were applied, the pulleys may have internal resistance and the force applied may not be the experienced force by the clamps. The four pulleys used were Pasco Super Pulleys. The pulleys were built with dual precision ball bearings that substantially reduced the friction present in the bearing (Pasco). The four pulleys were used to redirect the force applied from weights hanging off the table to the test article. The pulley and pulley mount can be seen in Figure 29.

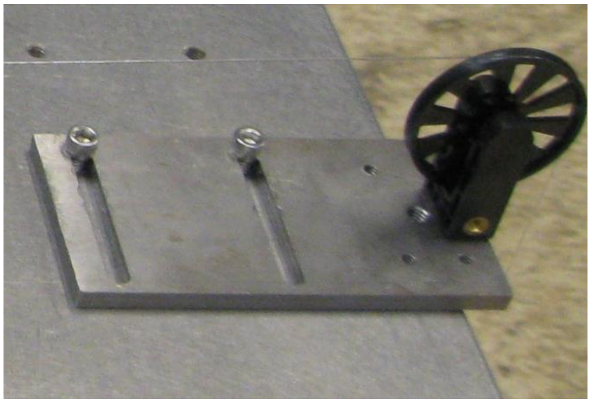

Figure 29: Pulley and Pulley Mount

Once the fixture was ready to test, appropriate symmetric forces were applied at the two corners of the triangle. After creating and processing multiple models, it was found that the vertically adjustable clamps were not in the same horizontal plane as the fixed clamp. The clamps were on average around 0.30 inches below the fixed location. It was believed that the main reason the clamps were not at the same vertical height was due to the assumption that the clamps were weightless. Since the main goal of the project was to create a flat surface by using different combination of factors, it was decided the fixture was unacceptable.

4.2 Final Fixture Design

The main issue with the initial fixture design was that the positions of the two clamps on the bottom corners of the fabric were below the height of the fixed corner of the fabric. This was due to the weights of the clamps. In the initial fixture between the fixed clamp and the table, there was a 0.25 inch spacer present. This allowed for the height of the fixed clamp to be on the same horizontal plane as the other two clamps. To try and offset this problem without having to redesign the fixture, the 0.25 inch spacer was removed and therefore, the fixed location was lowered by 0.25 inches while the pulleys and mounts were kept at the same height. This proved to be an adequate solution. After the change was made, the fixed clamp's height were only a few thousandths of an inch different than the two clamps that could move in the vertical direction, which was considered to be an acceptable amount. This was a substantial improvement compared to the initial design which had over a 0.30 inch difference.

In addition to lowering the fixed clamp's height, the resolution of the project was increased. Initially the material had key points applied roughly every inch. When the resolution was increased, the point spacing was increased to being every half of an inch. This increase in resolution would provide greater detail in the model and will have a greater chance of showing smaller wrinkles in the fabric.

The last change to the fixture setup was the background. In the initial design, there was a white piece of material with a few key points located on the material to help in orienting the photo. It was found that this material did not provide any sort of benefit and was therefore removed. The final fixture design can be seen in Figure 30.

Figure 30: Final Fixture Setup

Chapter 5 Fabric Testing

5.1 Test Introduction

Since many applications involving inflatable structures require strictly toleranced geometries to be effective, understanding how to control geometries of inflatable structures is crucial. In particular, there are structures that require their geometries to have a surface flatness requirement. These applications include but are not limited to solar sails, and radar reflectors. In these applications, the closer their surfaces are to being perfectly flat, the better their performance. In the case of solar sails, the sails will produce more propulsion, and have a uniform temperature distribution. With the radar reflector having a perfectly flat surface will maximize its radar cross section area to match its maximum theoretical value.

To better understand controlling surface flatness of fabric materials, three different factors were examined. These factors include subjecting the material to different bi-axial forces, different boundary conditions, and different fabric orientations. These three factors will be combined to see their effect on the overall flatness of the material. The results will provide information on which combination of factors is optimal.

In total, twelve separate combinations will be applied to the material to see their effect on the fabric's flatness. To avoid buckling in the material, a bi-axial force will be applied at each of the two corners of the material to maintain tension in the fabric. The top 90^0 corner of the triangle will be in a fixed position. To see the loading configuration, Figure 31 can be referenced.

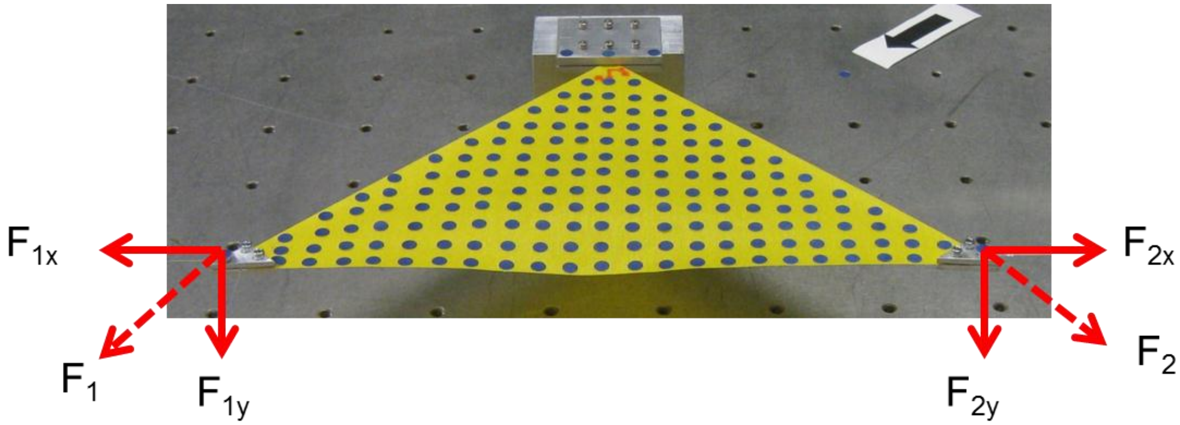

Figure 31: Loading Configuration

The combinations of forces that will be used in the experiment were symmetric and can be seen in Table 4.

Table 4: Loading Cases

Case 1		Case 2	
F_x=	0.680 lbs.	F_x=	0.980 lbs.
F_y=	0.404 lbs.	F_y=	0.320 lbs.
F_1=F_2=	0.791 lbs.	F_1=F_2=	1.031 lbs.

Another variable that was introduced is fabric orientation. The fabric is comprised of material properties that differ in regards to its orientation. The fabric has two different set of properties that run along the warp and fill directions of the fabric. The two different orientations used can be seen in Figure 32. On the left, the warp and fill run directly on their respective legs of the triangle. This is considered for this experiment to have 0^{o} rotation. On the right, the fabric is rotated 45^{o} clockwise.

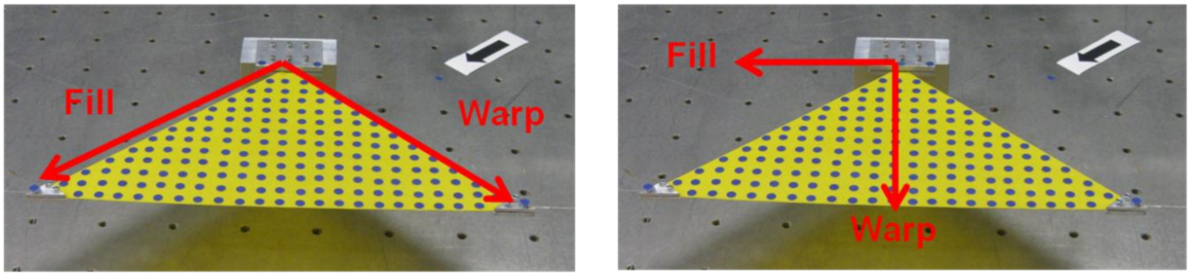

0^0 Orientation

45^0 Orientation

Figure 32: Fabric Orientation

The last variation that was introduced in the experiment deals with different boundary conditions applied at the two bottom corners of the fabric. In total, three different boundary conditions were applied. These boundary conditions can be seen in Figure 33.

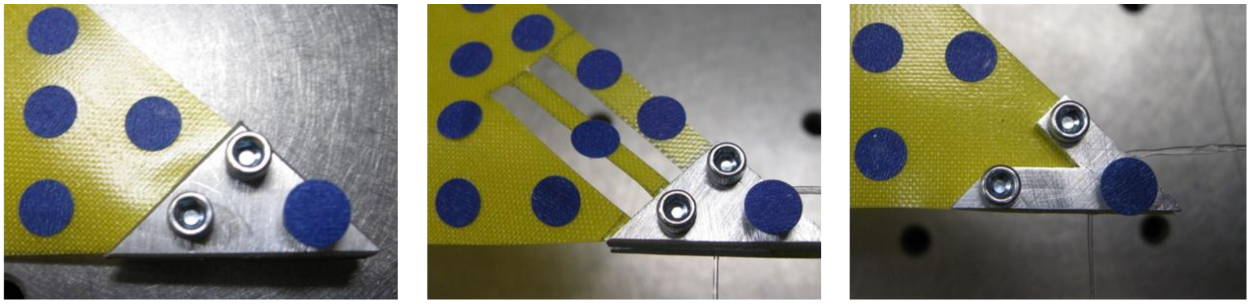

•Triangle Clamp

•Shear Compliant

•V-Clamp

Figure 33: Boundary Conditions

The clamp on the left has been designated as the "triangle clamp." This clamp is designed to apply a uniform force across the entire 0.75 inch corner of the fabric in both the x and y directions. The "shear compliant clamp" is based off the clamps used by Talley. The clamp was designed to reduce the amount of shear stress transferred into the test specimen. Unlike Talley, this experiment is applying a force in both the x and y direction to the fabric. Therefore, to reduce the shear stress, material was removed from the fabric at a 45^0 angle. This should effectively reduce the shear stress caused by both the X and Y forces. When shear forces gets introduced to the fabric, it should cause the wrinkle amplitude to decrease, and therefore result in smaller amounts of deflection.

The main issue found in using the shear compliant boundary condition was whether the material could be placed onto the clamp and the bolts tightened without the material shifting positions. Many times the material would shift during the rotation of the bolts. This caused the shear compliant border to shift upon tightening the clamp. Even though the clamp had a defined location where it should be placed on the fabric, it took many attempts to properly secure the fabric into the clamp without having introduced any wrinkling to the compliant border. If I would slightly tighten each of the bolts and then go back and steadily increase the torque applied to all the bolts and keep repeating till the bolts were adequately tight, the shear compliant border would not shift as significantly if this step was not taken. Still, it took many attempts to properly clamp the fabric.

A new clamp that was introduced in this study was the “V-Clamp.” The clamp resembles the triangular clamp with material removed from the middle. Unlike both the triangular and shear compliant clamps, the V-Clamp was designed to only apply forces to the edges of the fabric. The clamp was designed so that the effects of applying forces exclusively to the edges could be studied. Although the clamp does have material removed from the inner portions, the clamp’s weight was comparable to the triangular clamp. The V-Clamp weights 0.008 lbs. compared to the triangular clamp’s weight of 0.009 lbs.

5.2 Yield Stress of Material

One concern that arose when testing the thin material was that the material may yield during testing. Even though small forces were being applied to the material, the cross section area was relatively small at all three corner locations. If the material would yield, new test articles would need to be created for each of the twelve tests. Since it would be ideal to be able to reuse the fabric material in the multiple experiments, the yield point of the material needed to be determined. Being able to reuse the material would save considerable time since new test specimens would not have to be created, as well as reference points would not have to be applied for each of the twelve cases that were to be tested. The fabric that was used for the triangular piece of material was from ILC Dover and had a coating on both sides. To calculate the materials yield stress, stress-strain curves were used to calculate the modulus of elasticity from data found in (Smith & Fadi, 2009). To calculate the yield point, the offset method was used as defined in (Budynas & Nisbett, 2008). Since using 0.2% of the original gauge length is typical and the gauge length used was 2 inches, an offset of 0.004 was used. To use the offset method, the modulus of elasticity needed to be calculated.

When using the offset method to calculate the yield stress, having a larger modulus will output a lower yield stress. To guarantee that the material will not yield during testing, the largest modulus needed to be determined to ensure the material would not yield. To find the maximum modulus, the initial linear portion of the stress-strain graph was taken into account since its portion had the largest modulus. Using this section of the stress-strain curve, a line of best fit was used to determine the modulus. An example of the section that was used to calculate the modulus can be seen circled in Figure 34.

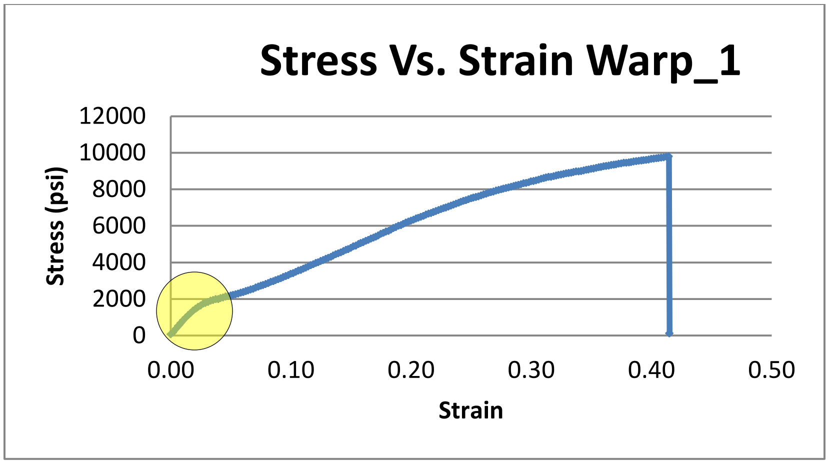

Figure 34: Stress-Strain Graph Warp_1

After examining Figure 34, it is apparent that the graph possesses a linear elastic region, and therefore using the offset method is a valid way to calculate the yield point (Callister & Callister, 2000).

When the portion of the stress-strain graph that is circled is magnified, we are able to apply a line of best fit to obtain the modulus. Figure 35 shows the line of best fit for one of the five cases in the warp direction. The remaining expanded stress-strain graphs for both the warp and fill directions can be found in Appendix A.3 Stress-Strain Graphs.

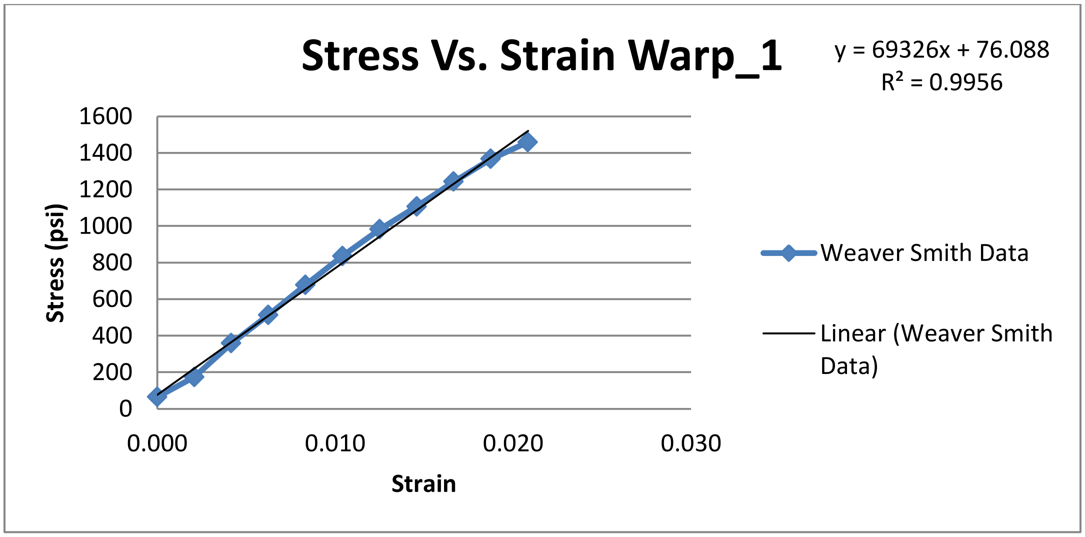

Figure 35: Stress-Strain Warp_1 Line of Best Fit

In total five separate stress-strain tests for each the warp and fill directions were completed and modulus values were calculated for both directions and an average was taken of the five. These values can be seen in Table 5.

Table 5: Modulus of Elasticity for Warp and Fill Directions

Warp Direction		Units	Fill Direction		Units
Modulus 1	69,326	psi	Modulus 1	12,349	psi
Modulus 2	67,853	psi	Modulus 2	13,471	psi
Modulus 3	68,843	psi	Modulus 3	12,903	psi
Modulus 4	67,507	psi	Modulus 4	12,416	psi
Modulus 5	67,197	psi	Modulus 5	12,293	psi
Average Modulus	68,145	psi	Average Modulus	12,686	psi

Having calculated the modulus of elasticity, the yield strength is able to be computed for both the warp and fill directions using the offset method. As stated previously, an offset of 0.004 will be used. The offset method was applied to five different stress-strain graphs for each the warp and fill directions. Applying the offset method produced the graph seen in Figure 36.

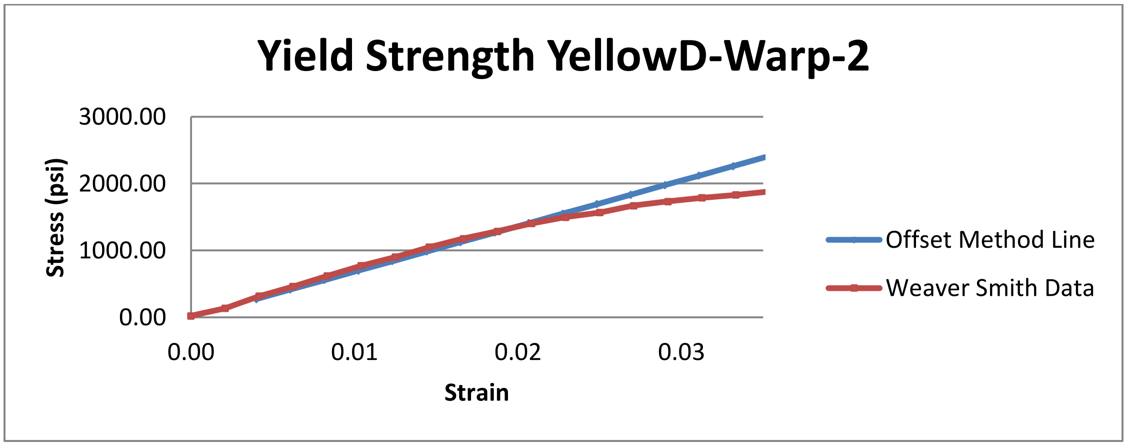

Figure 36: Yield Strength Using Offset Method

After graphing and calculating the intersection for all stress-strain graphs, the yield strengths were inserted into Table 6, and averages were calculated. The rest of the graphs using the offset method to calculate yield strength can be found in Appendix A.4 Yield Strength Graphs.

Table 6: Calculated Yield Strength Using Offset Method

Yield Strength				
Trial #	Warp		Fill	
1	1692	psi	1399	psi
2	1408	psi	N/A	psi
3	1550	psi	N/A	psi
4	N/A	psi	1452	psi
5	1408	psi	1372	psi
Average	1515	psi	1407	psi

In three separate cases the yield strengths were unable to be calculated using the offset method. In the case of when the warp yield strength was calculated in trial 4, the line created using the calculated modulus was consistently above the respective collected data at all points, therefore causing the two lines never to intersect. The line came close to intersecting but never intersected the stress-strain line. This case can be seen in Figure 37.

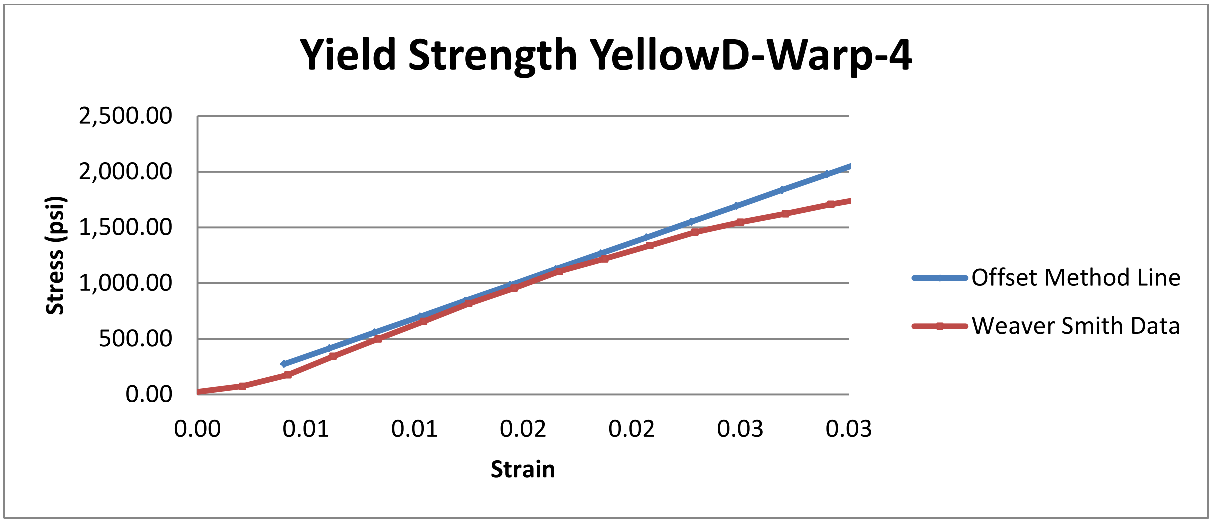

Figure 37: Yield Strength Warp_4

In the case of when trial 2 and 3 yield strengths were calculated in the fill direction, the intersection points were extremely high compared to other values in the fill and warp direction. For this reason, these yield strength values were disregarded. This case can be seen in Figure 38. In this case the lines nearly intersect at about 1800 psi, but the lines don't intersect till over 7000 psi.

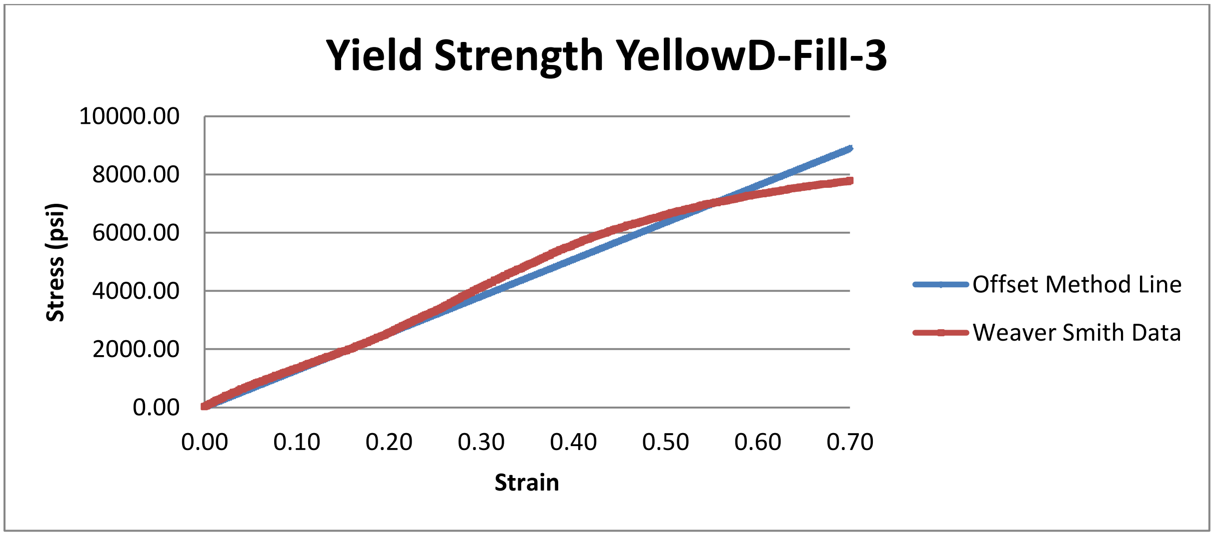

Figure 38: Yield Strength Fill_3

With both the warp and fill yield strengths calculated, it can be determined whether the material will yield when the forces are applied. Since the shear compliant boundary condition is comprised of the smallest cross sectional area in all cases, it will be the only location that will be checked for the material yielding. To calculate the cross sectional area, the thickness of the material needs to be measured. To measure the thickness, 5 locations were measured on the fabric and then the average was then taken. These measurements can be seen in Table 7.

Table 7: Yellow Double Coated ILC Dover Material Thickness

Fabric Height		
1	0.0115	Inches
2	0.012	Inches
3	0.013	Inches
4	0.012	Inches
5	0.015	Inches
Average	0.0127	Inches

The clamp length of the shear compliant boundary condition was 0.75 inches, but there were two strips of material removed from the material, and each had a width of 0.125 inches giving an equivalent clamp length of 0.5 inches. These measurements can be seen in Figure 39.

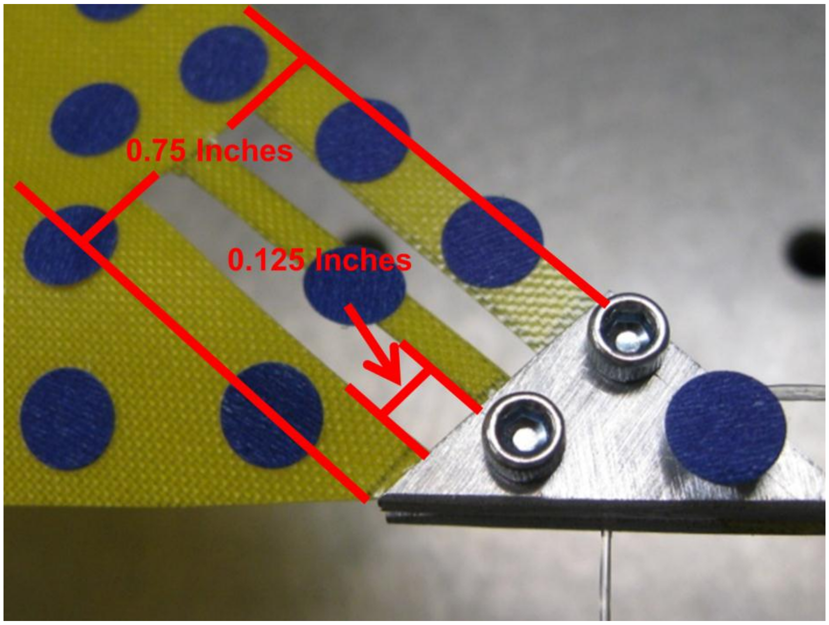

Figure 39: Shear Clamp Dimensions

With both the clamp length of the shear compliant boundary condition as well as the height of the material, the cross sectional area was calculated to be approximately 0.006 inches^2. Using the axial stress equation found in Equation 4, the max stress the material reaches can be determined.

$$\sigma_{max} = \frac{F_{max}}{A_{min}} \tag{4}$$

The total magnitude of the forces in the X and Y directions for case 2 loading, which was the heaviest load applied, was 1.031 lbs. Applying Equation 4 gives the max stress;

$$\sigma_{max} = 172\ psi$$

Since it was previously determined that the yield stress for the warp and fill were 1515 psi and 1407 psi respectively, it can be seen that the max stress induced in the material is well under the yield stress. For this reason, it was determined that the material would be able to reused for multiple cases.

To further validate that the material will not yield, an additional test was conducted. To test if yielding occurred, 0.791 lbs. were applied to the shear compliant border and the surface was measured using PhotoModler. The force was then increased to a magnitude of 1.031 lbs. Next the force was decreased to the original weight of 0.791 lbs. and the surface was measured again. To confirm the material did not yield, contours were compared before and after the high loading of 1.031 lbs. was applied. If there were any signs of sagging in the contours after the high load was applied, this would have been evidence that yielding took place. Two contours were examined to verify that no yielding took place. These contours locations can be seen in Figure 40.

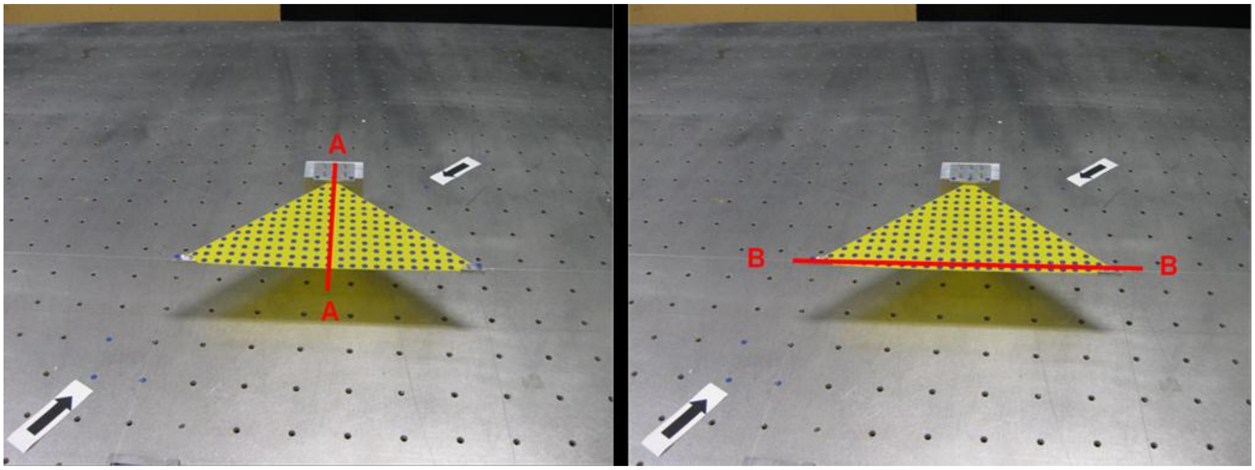

Figure 40: Contour Line Locations

The appropriate loads were applied and the surface was measured twice, once before the high load of 1.031 lbs. was applied and once after. The contours can be seen in Figure 41, Figure 42.

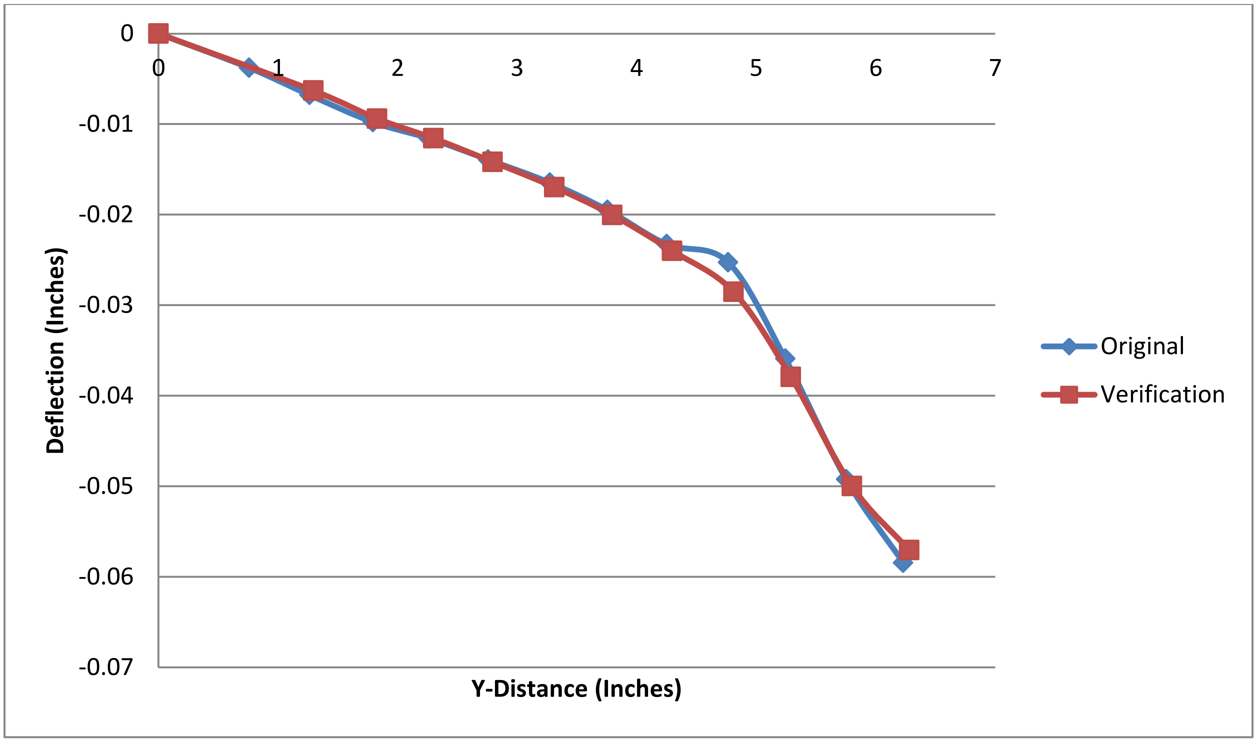

Figure 41: Contour A- A

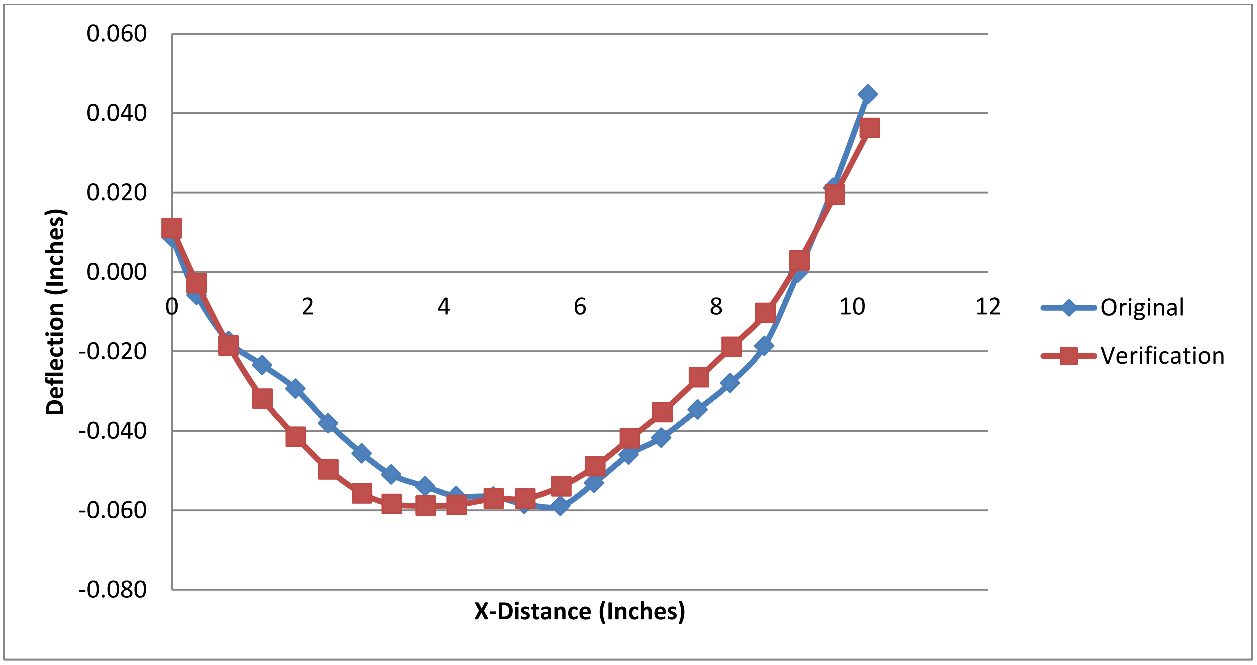

Figure 42: Contour B-B

In examining both contours, there was no evidence that yielding took place after the material was loaded with 1.031 lbs. As stated the shear compliant border was the boundary condition used in the test. Since the shear compliant border had material removed at both of its 45^0 corners, it was therefore subjected to the highest stress out of all of the boundary conditions. Since the test showed that the shear compliant did not yield under the applied loads, it can be concluded that the material will not yield when subjected to a max force of 1.031 lbs.

Although the test showed no signs of yielding, the results did vary by small amounts and can be seen in Figure 41. This difficulty of attaching the clamps to the material is suspected to be the root cause and the difficulty has been previously discussed in this paper.

5.3 Test Results

Having determined the material used would not yield due to the applied forces, testing of different combinations could be completed while reusing previously tested material. Since there were two loading cases, two fabric orientations, and three boundary conditions used, a total of twelve test cases were compiled to see how different combinations would affect the overall flatness of the material. In all cases, flatness was calculated in terms of RMS values. To calculate the RMS values, Equation 3 was used and can be seen again:

$$RMS = sqrt(\frac{1}{n} * \sum_{i=1}^{n}(PhotoModler\ Measured\ Distance - Average\ PhotoModler\ Distance)^2) \qquad (3)$$

The RMS values were calculated in part by taking each measured reference point on the contour surface and subtracting from it the average deflection. To help visualize the Equation 5, Figure 43 shows the overall contour of the material along with the average deflection measured.

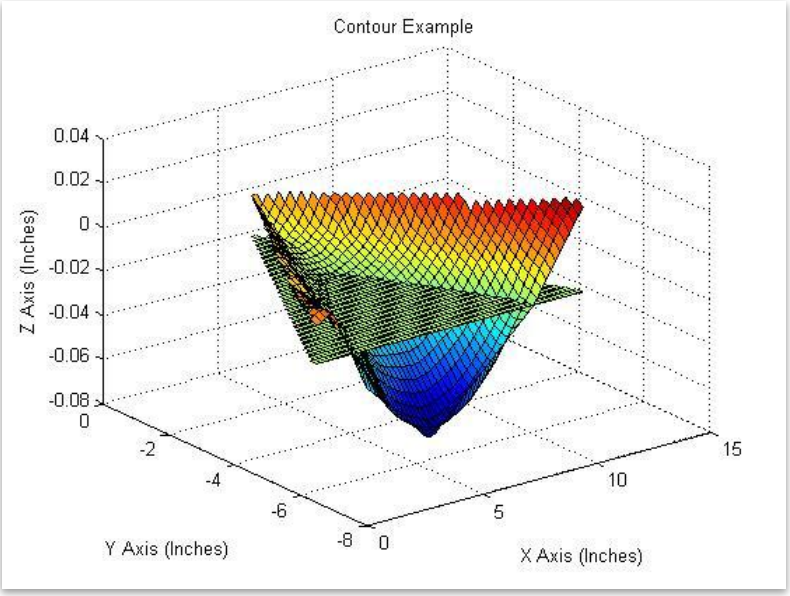

Figure 43: Example Contour with Average Deflection Shown

Once the twelve test cases were ready to be measured, the 8 steps described in (Thota, Leifer, Smith, & Lumpp, January, 2003) to accurately locate points and create at 3D model were used. To see which combination of factors were used in each test of the twelve test cases, Table 8 can be referenced and an index can be seen in Table 9.

Table 8: Combination of Factors

Case #	**Loading (lbs.)**	**Boundary Condition**	**Fabric Orientation**
Case 1	0.791	T.C.	0°
Case 2	1.031	T.C.	0°
Case 3	0.791	T.C.	45°
Case 4	1.031	T.C.	45°
Case 5	0.791	S.C.	0°
Case 6	1.031	S.C.	0°
Case 7	0.791	S.C.	45°
Case 8	1.031	S.C.	45°
Case 9	0.791	V.C.	0°
Case 10	1.031	V.C.	0°
Case 11	0.791	V.C.	45°
Case 12	1.031	V.C.	45°

Table 9: Index for Results

B.C.	Boundary Condition
T.C.	Triangle Clamp
S.C.	Shear Compliant
V.C.	V-Clamp

When each of the twelve test cases was completed, a RMS value was able to be calculated for each respective case. The results can be seen in Table 10.

Table 10: RMS Values

RMS (Inches)						
Loading	**Fabric Orientation 1 (0°)**			**Fabric Orientation 2 (45°)**		
	B.C. (1) T.C.	**B.C. (2) S.C.**	**B.C. (3) V.C.**	**B.C. (1) T.C.**	**B.C. (2) S.C.**	**B.C. (3) V.C.**
F=0.791 lbs.	**0.020**	**0.021**	**0.017**	**0.033**	**0.050**	**0.049**
F=1.031 lbs.	**0.011**	**0.019**	**0.015**	**0.014**	**0.022**	**0.016**

From the table, the impacts of different combinations are able to be seen. The major impact on the overall flatness of the material was the fabric orientation. It can be clearly seen that when the orientation is rotated from a 0^{o} to 45^{o}, the RMS value on average increases by 76%. The fabric orientation had the most significant impact on the materials RMS value. The second factor that had a significant effect on the RMS values was the different forces applied to the material. When the forces applied were increased by 30%, the RMS values decrease by an average of 40%. In particular, if the force is increase by 30% and the effect is examined for each fabric orientation, we see that the RMS decreases by 59% and 20% for fabric orientations of 45^{0} and 0^{0} respectively. The factor that impacted the RMS values the least were the three boundary conditions. When different boundary conditions were changed, the RMS values did vary, although it was seen that the triangular clamp provided the best results.

In addition to being able to calculate the RMS values of the material, different contour lines of the fabric were able to be produced. In specific, two specific contour lines were examined. The locations shown before are presented again and can be seen in Figure 44.

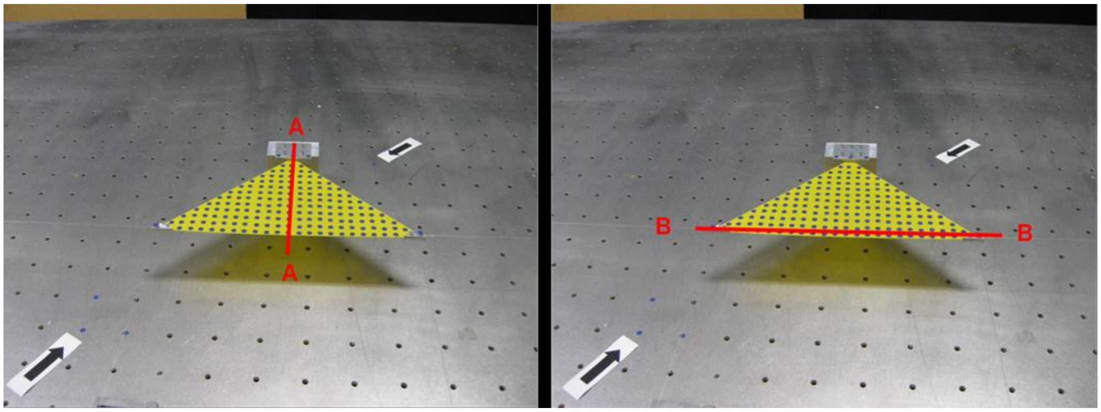

Figure 44: Contour Line Locations

When examining the two separate contours for all cases, it was observed that two trends were present and varied when different loads were applied. The first trend was apparent in all cases when the forces applied had a magnitude of 0.791 lbs. A representative graph can be seen in Figure 45.

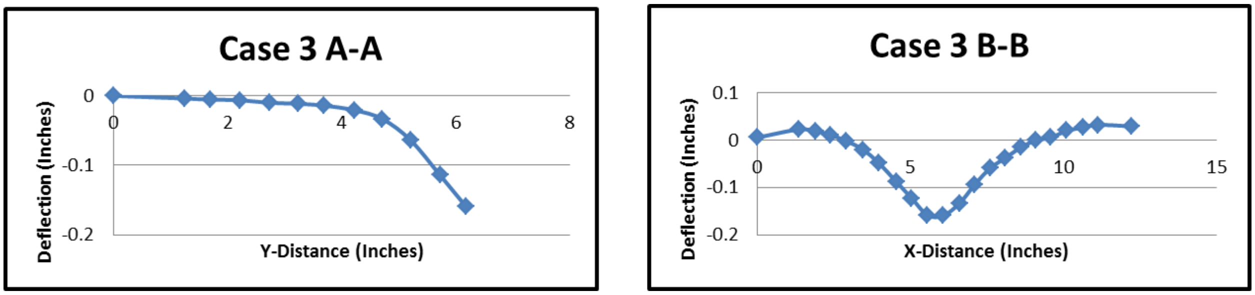

Figure 45: Case 3 Contour Lines

In Case 3, the A-A contour line starts at the fixed clamp and therefore starts at a height of 0 inches. As the contour line moves further away from the fixed point along the y-axis, deflection increases, until the line ultimately achieves its max deflection at the last point on the contour. When the B-B contour line is examined, it seen that the max deflection occurs roughly at the center of the contour. Additionally the effects of the clamps not being weightless can be seen at both ends of the graph.

The second trend present occurred in most cases when the loading is increased to a magnitude of 1.031 lbs. Representative contour lines of the high loading case can be seen in Figure 46.

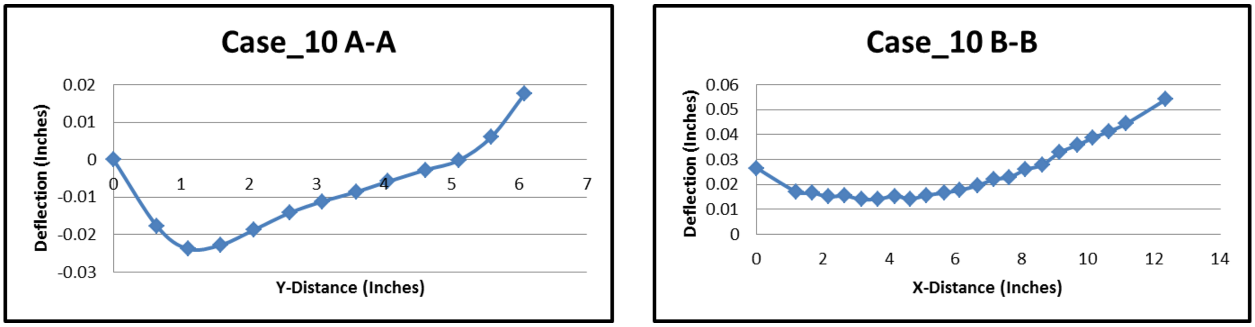

Figure 46: Case 10 Contour Lines

Unlike cases where lower forces were applied, the point furthest from the fixed location on the contour line of A-A was not always where the maximum deflection occurred on the contour. When 1.031 lbs. was applied, contour lines usually consisted of multiple concave and convex portions where when 0.791 lbs. was applied, the A-A contour line remained concave in most all cases. When the B-B contour line was examined, the overall shape of the contour was different. In the six cases where the forces applied were 1.031 lbs. all points with the exception of one, had only positive deflection. With the contour B-B line, it was seen that the contour was flatter than previously seen when the lower forces were applied. This verifies the information presented in Table 10 of the twelve RMS values. In most cases, the contour did not have any drastic changes in slope. The rest of the contour lines can be found in Appendix A.5 Contour Lines.

Since it can be seen that the deflection present in the material does not all occur below or above the fixed point, having the maximum, minimum and average deflections for all cases should be examined for the twelve test cases. These values can be seen in Table 11 and Table **12**.

Table 11: Maximum Positive Deflection

Max Positive Deflection (Inches)						
Loading	Fabric Orientation 1 (0^0)			Fabric Orientation 2 (45^o)		
	B.C. (1) T.C.	B.C. (2) S.C.	B.C. (3) V.C.	B.C. (1) T.C.	B.C. (2) S.C.	B.C. (3) V.C.
F=0.791 lbs.	0.022	0.070	0.056	0.032	0.062	0.054
F=1.031 lbs.	0.022	0.122	0.060	0.038	0.095	0.051

When examining Table 11, it is apparent that the trends that existed in RMS values were not present. Fabric orientations did not play a major factor in the maximum positive deflection. When looking at the table, which fabric orientations were used did not consistently provide a lower deflection either. Additionally when the weight was increased to 1.031 lbs., in all but two cases the maximum positive deflection increased. When boundary conditions were examined, it can be seen that in all cases, the triangular clamp produced the least deflection.

Table 12: Maximum Negative Deflection

Max Negative Deflection (Inches)						
Loading	Fabric Orientation 1 (0^0)			Fabric Orientation 2 (45^o)		
	B.C. (1) T.C.	B.C. (2) S.C.	B.C. (3) V.C.	B.C. (1) T.C.	B.C. (2) S.C.	B.C. (3) V.C.
F=0.791 lbs.	-0.067	-0.059	-0.039	-0.159	-0.194	-0.195
F=1.031 lbs.	-0.020	-0.012	-0.023	-0.021	-0.032	-0.020

Alternatively, the maximum negative deflection can be examined. The table contains trends that were present in Table 10 containing RMS values. Here it can be seen that when the force is increased to 1.031 lbs., the deflection is decreased by on average 75%. Furthermore, fabric orientation has a large role in effect on the maximum negative deflection. When the fabric has an orientation of 45°, and 0.791 lbs. is applied, the fabric has a much larger deflection than its 0° counterpart.

Looking at contour lines of certain key locations and calculating the maximum and minimum deflections provides useful, but limited information on the overall shape of the fabric. To get a full understanding of the deflection that took place, a 3D model was the best way to visualize the deformation. The information present in the 3D model expanded greatly upon the information gained by visualizing the 2D contour lines. When a force of 0.791 lbs. was applied to the material at the lower corners, resulting deflection occurred mostly in the negative direction. The effects from the weight of the clamps were able to be seen as well. When the force is increased to 1.031 lbs., the deflection is seen to occur in both the negative and positive direction. These trends present can be seen in Figure 47, and in Figure 48. The remaining contour plots can be found in Appendix A.6 Contour Plots.

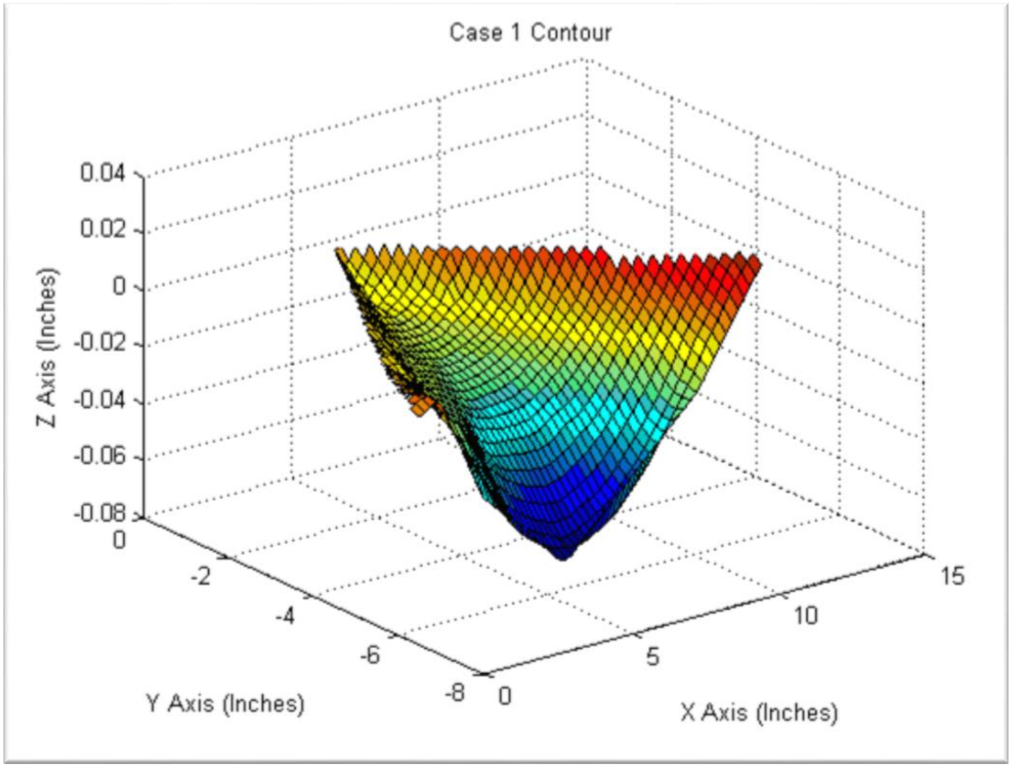

Figure 47: Case 1 Contour Plot

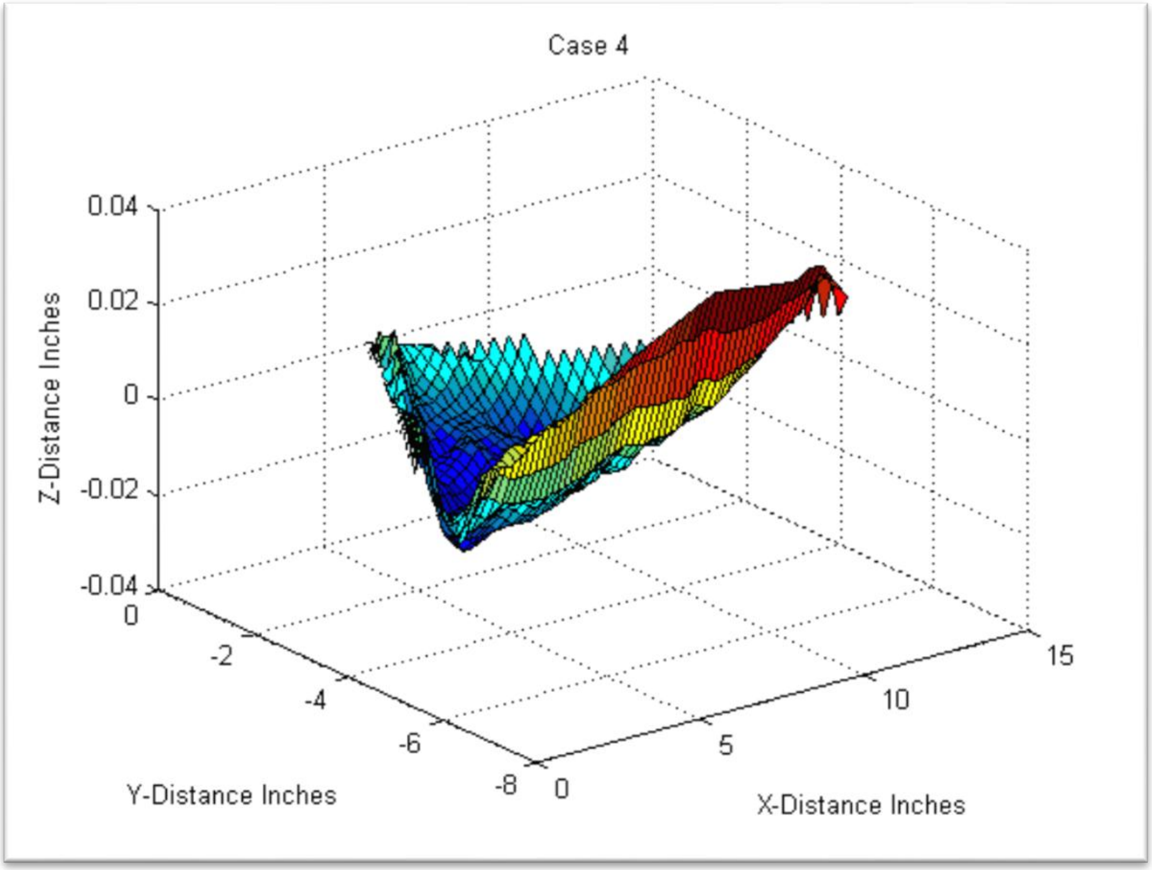

Figure 48: Case 4 Contour Plot

Chapter 6 Conclusion

6.1 Conclusions

High precision inflatables have been used in many applications since their start with NASA's ECHO I Balloon. As demand for inflatable structures grows so does the need for the structures to become more precise in their construction. While work has been conducted to research ways into improving geometric control, the work has been limited. The shear compliant boundary condition was an advancement but still left much to be researched in effectively controlling inflatable surfaces.

Precisely controlling inflatable surfaces requires an accurate way to measure surfaces to determine if surface requirements have been met. It was determined through testing that PhotoModler 6 would efficiently and effectively be able to measure surfaces used in inflatable and gossamer structures. Using PhotoModler, testing was completed on a triangular piece of fabric manufactured by ILC Dover. The triangular geometry of the fabric was chosen since the shape sees use in applications such as solar sails as well as radar reflectors. Testing completed involved testing three boundary conditions, two fabric orientations and two different applied forces.

Before testing could begin, the yield strength of the material needed to be calculated. If the material would yield with the applied loads, this would require twelve separate test specimens to be created which would not be ideal. It was determined that the stress induced never exceeded the materials yield strength and therefore the material did not yield. As a result only four test specimens needed to be created which took substantially less time to manufacture than if twelve test articles were to be made. Testing the material's yield strength was calculated two ways. First the offset method was used as described in (Budynas & Nisbett, 2008). It was found that the yield strength of the material was substantially greater than the stress the material was subjected to.

An additional test to verify whether the material did not yield was completed. In the test, the shear compliant border was used. The test article was loaded with the low loading case of 0.791 lbs. The surface was measured, and the force was increased to 1.031 lbs. The applied force was then lowered to the original force of 0.791 lbs. The surface was measured again and compared with the original surface measurement. If yielding had taken place, signs of yielding would have been seen in the two contours that were examined. No signs of yielding were seen in the conducted test, and since the shear compliant boundary condition saw the highest stress levels of all boundary conditions, it was concluded that all the twelve test cases would not yield under the applied loads.

After the twelve test cases were completed, RMS values for each of the twelve test cases were calculated. It was found that which boundary condition used did not have as significant effect as the other two test variations used in testing. However, the triangle clamp used in testing produced slightly lower RMS values in all test cases but one case. It was found that the greatest factor on the fabric's flatness was fabric orientation. When the fabric was rotated from 0^{o} to 45^{o}, the RMS value on average increased by 76%. The second significant effect on flatness was which of the two force combinations were used. When the force was increased by 30%, the RMS values decrease by an average of 40%.

The effects of different combinations were seen to have a significant impact on the test materials RMS values. To produce a surface with the lowest RMS values, the high loading case should be used along with the 0^{0} fabric orientation as well as the triangular clamp used.

6.2 Future Work

To improve upon the current study involving deflection and the measuring of RMS values, a new fixture could be designed to test the material. The new design would be based around having all three corner of the triangle at a known, fixed height. With all the heights of the corners known and on the same horizontal plan, the weight of the clamps would not have an effect on the results. Having this new fixture, the results produced would provide more insight into how the different combinations affect the flatness of the material. The results would purely reflect the difference in the combinations tested and not have the noise of the weight of the clamps integrated in the results.

To further improve on the testing fixture, introducing a new way to scale the project would be an advancement. Although an optical table provided an accurate and precise way to calibrate the distance of the project, the issue occurred was when photos were taken and key points were selected and referenced, PhotoModler did not always locate the point to be flush with the surface of the table. Consequently this made the scaling to not be exact. Instead of setting a distance that should be solely in the X and Y direction, a vertical component of distance was introduced. In most cases, the points were measured to be only few thousandths of an inch into the tapped hole. To scale the model ideally, the scale should have two points relatively far apart from one another and the two points would be flush with the surface. The two points would have an accurate and known length between them. The more accurate the distance is between the two points, the more accurate the model created would be.

With an updated fixture the twelve test cases could be reexamined while testing an additional factor in the test matrix. One additional factor that could be tested is to examine the effect that a -45^{o} rotation on the fabric's orientation would have on the model. Since the fabric orientation play a large role in the fabric's RMS value, having an additional orientation would provide insight in how to best control the flatness of the surface. This fabric orientation can be seen in Figure 49.

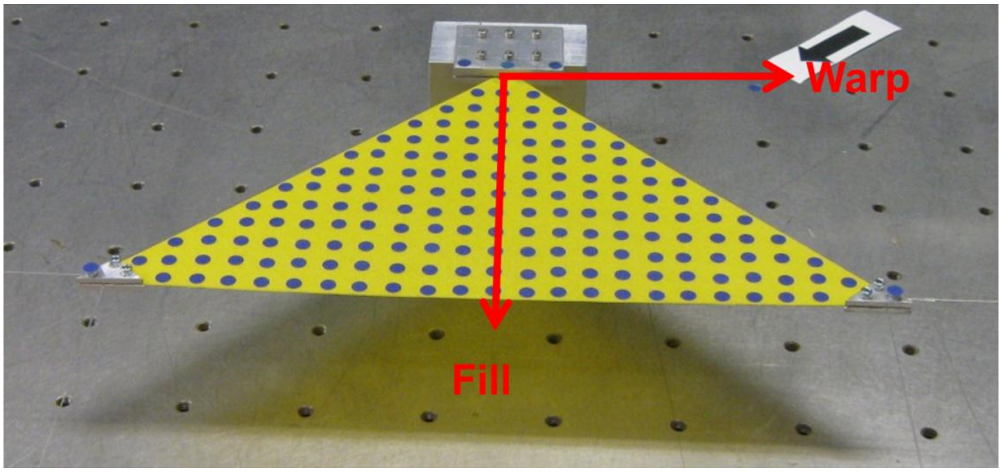

Figure 49: Additional Fabric Orientation

The last recommendation for future work would entail comparing the experimental models to numerical models. Programs that use finite elements could be used to simulate the different boundary conditions, different loading cases as well as the different fabric orientations that were used in experimental models. Since the experimental models have been created, the numerical models could be checked against experimental data to ensure accuracy of the model generated. Having an accurate numerical model that represents these different test cases, the code used could be optimized to provide users with which conditions provide the smallest surface deflection. Additionally different factors could then be examined and introduced into the test matrix.

Appendix A:

A.1 PhotoModler Error

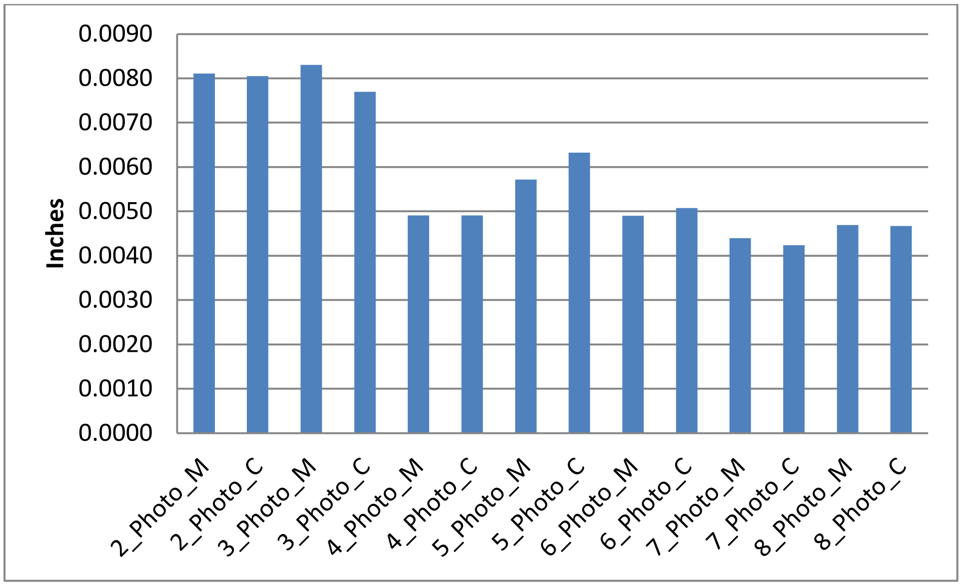

Figure 50: PhotoModler 2 Inch Error

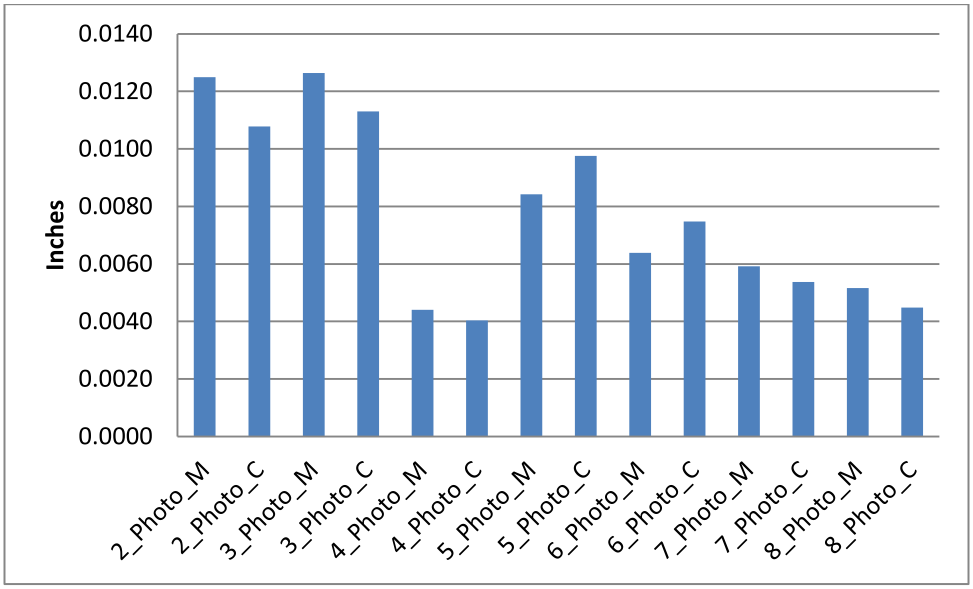

Figure 51: PhotoModler 4 Inch Error

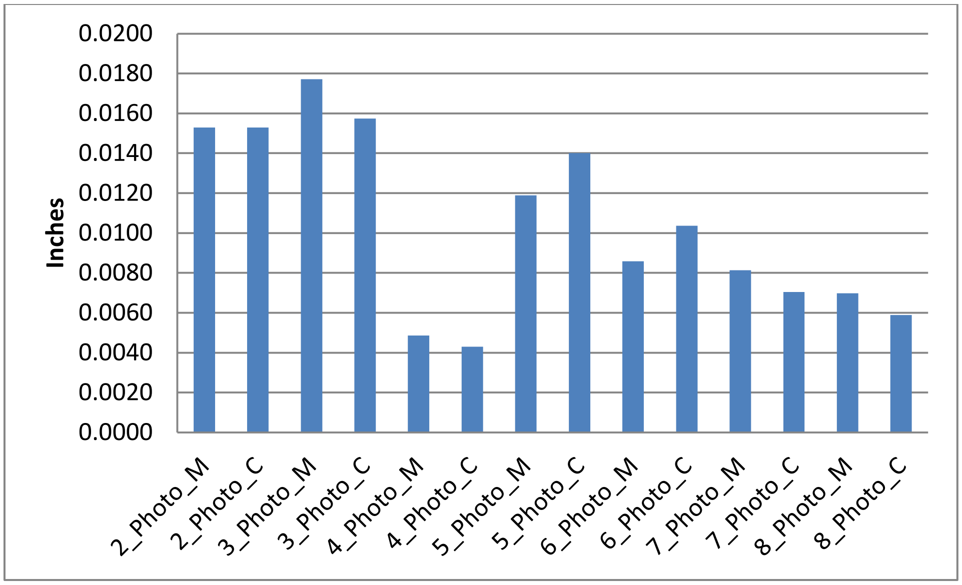

Figure 52: PhotoModler 6 Inch Error

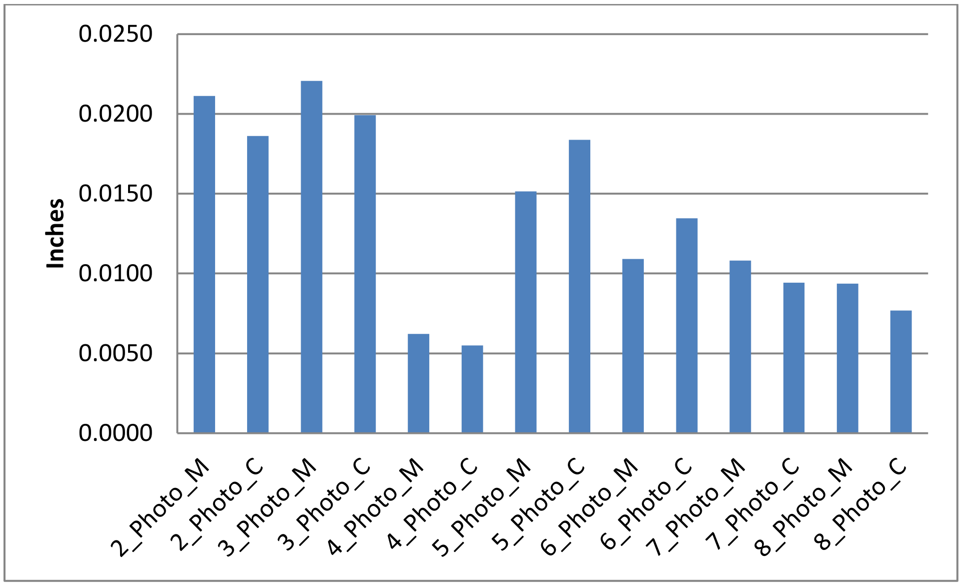

Figure 53: PhotoModler 8 Inch Error

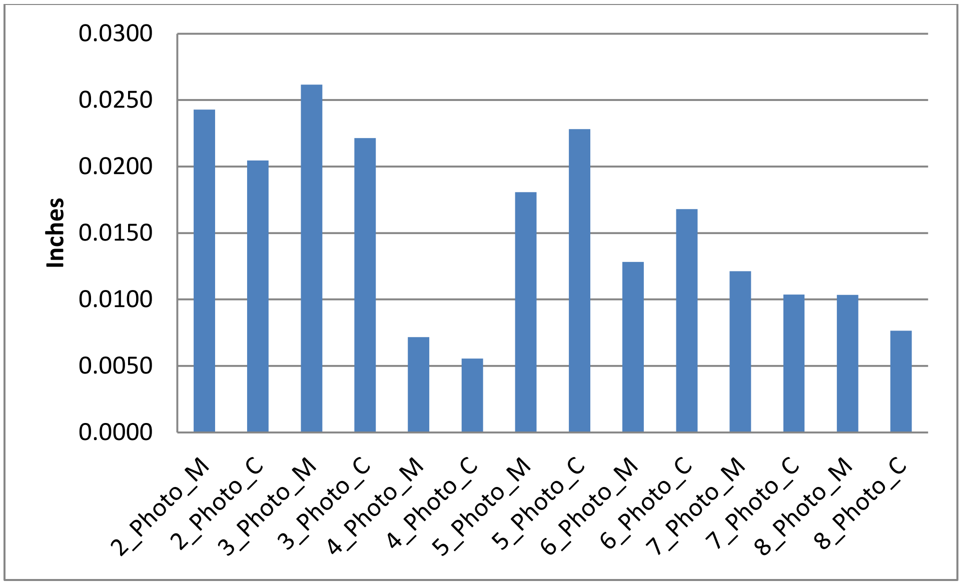

Figure 54: PhotoModler 10 Inch Error

A.2 PhotoModler RMS Values

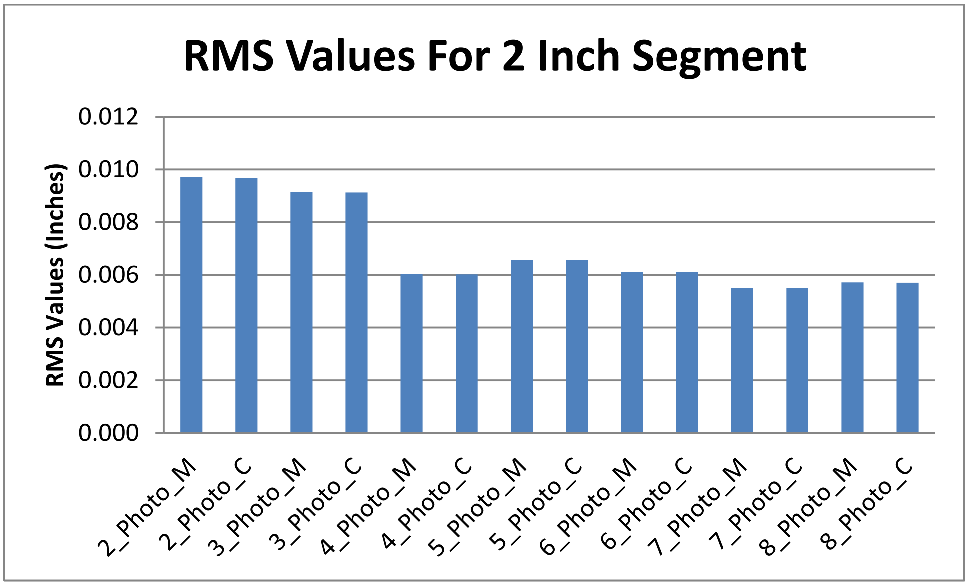

Figure 55: RMS Values For a 2 Inch Segment

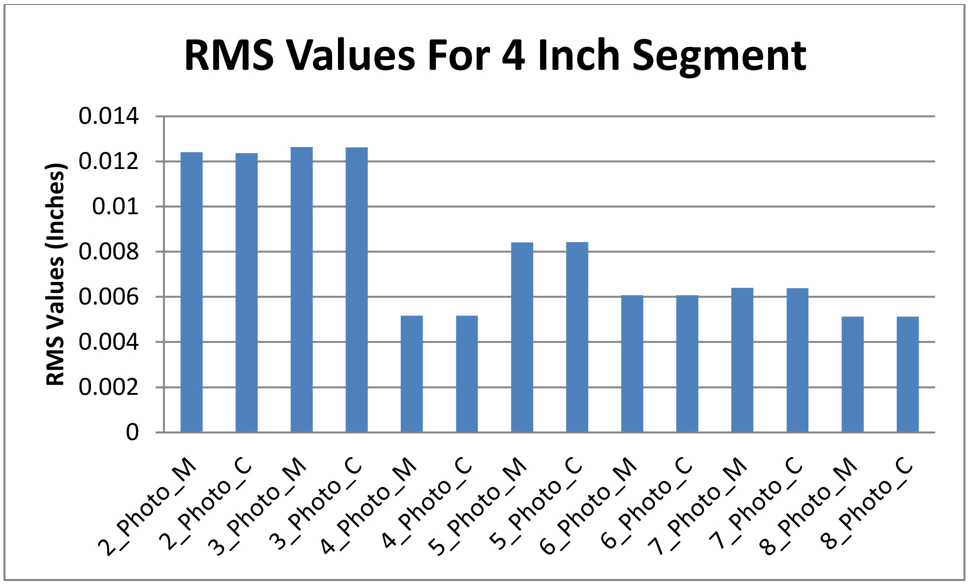

Figure 56: RMS Values For A 4 Inch Segment

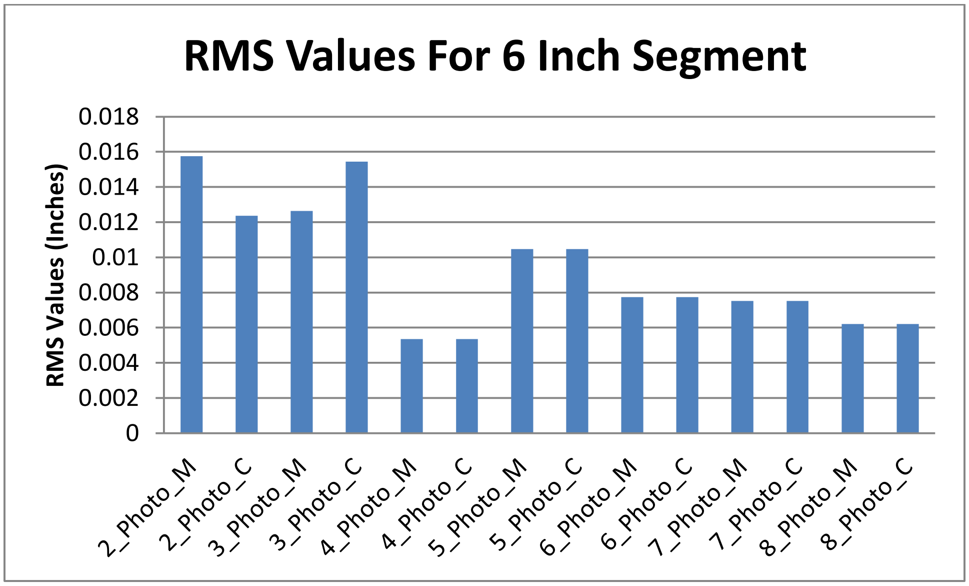

Figure 57: RMS Values For A 6 Inch Segment

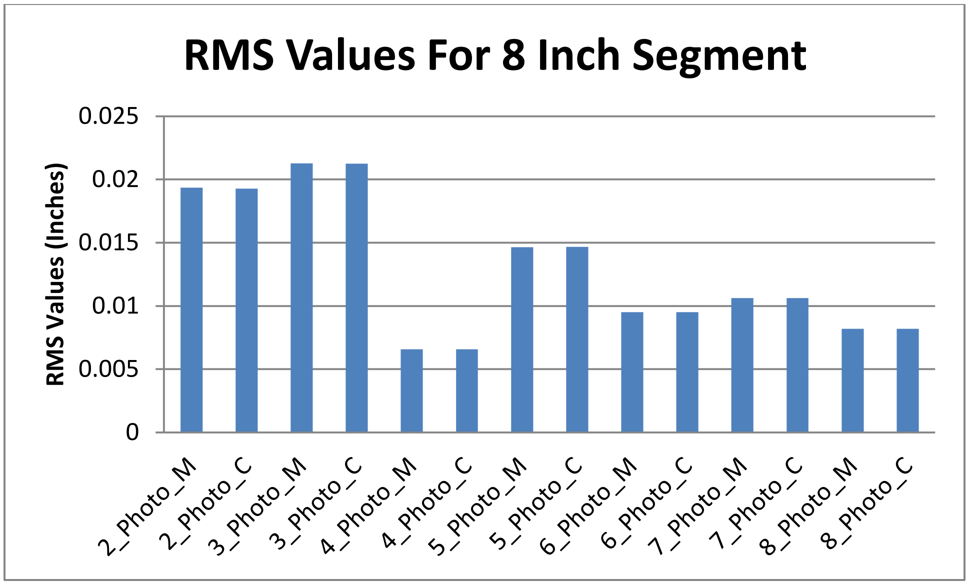

Figure 58: RMS Values For A 8 Inch Segment

A.3 Stress-Strain Graphs

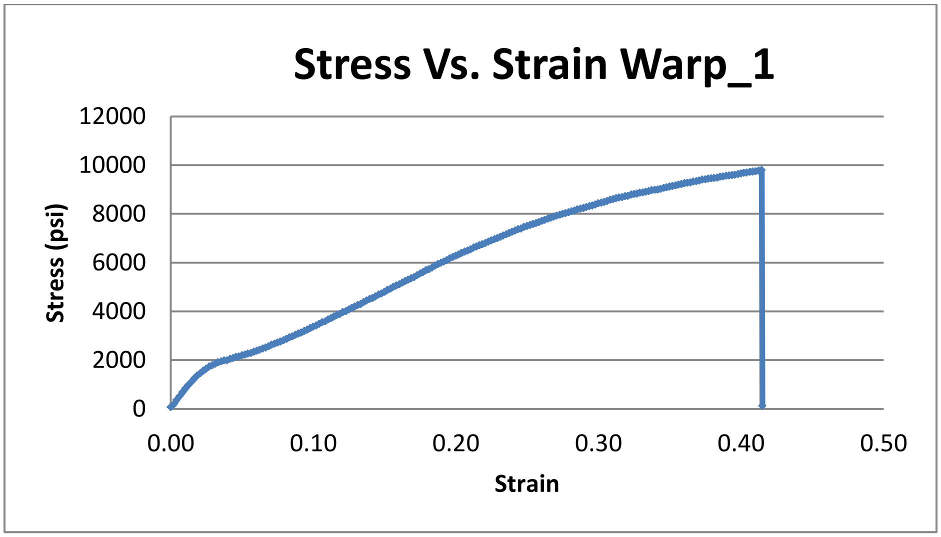

Figure 59: Stress-Strain Warp_1 Line of Best Fit

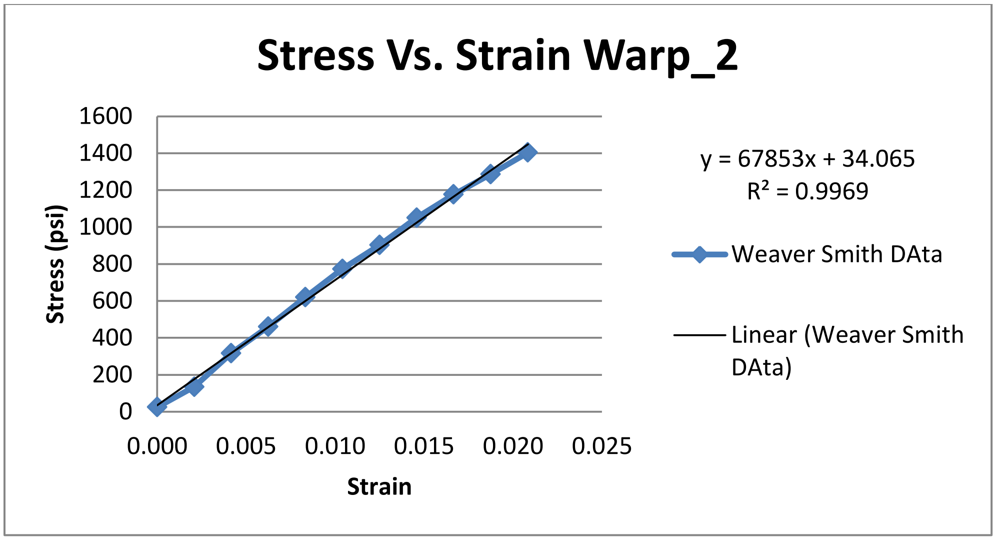

Figure 60: Stress-Strain Warp_2 Line of Best Fit

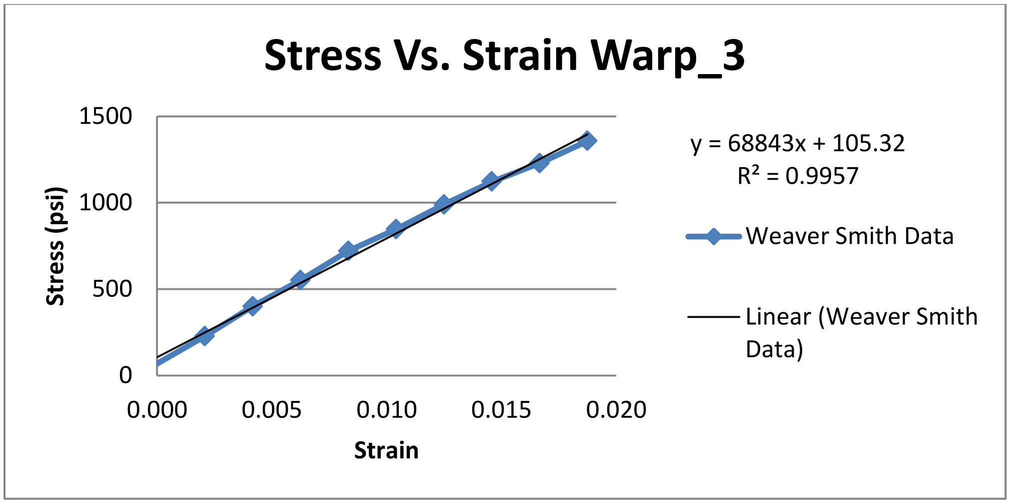

Figure 61: Stress-Strain Warp_3 Line of Best Fit

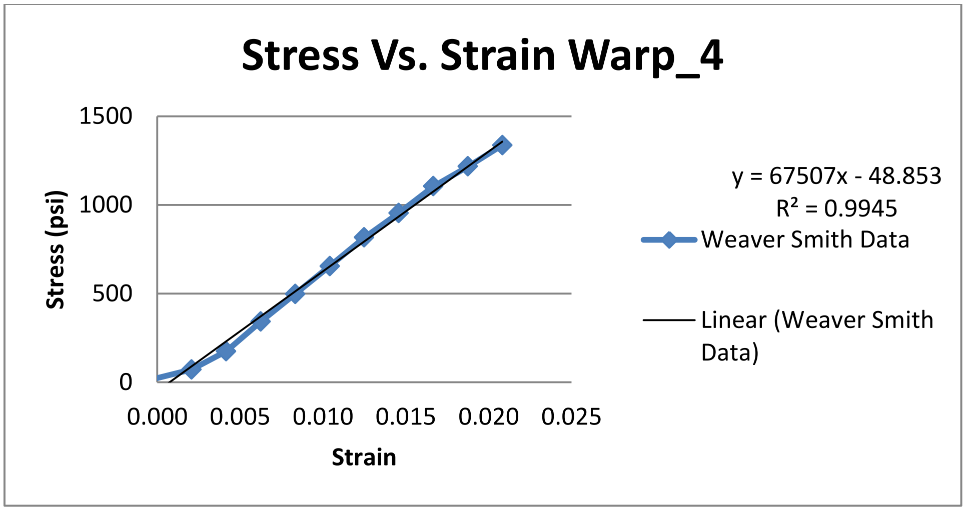

Figure 62: Stress-Strain Warp_4 Line of Best Fit

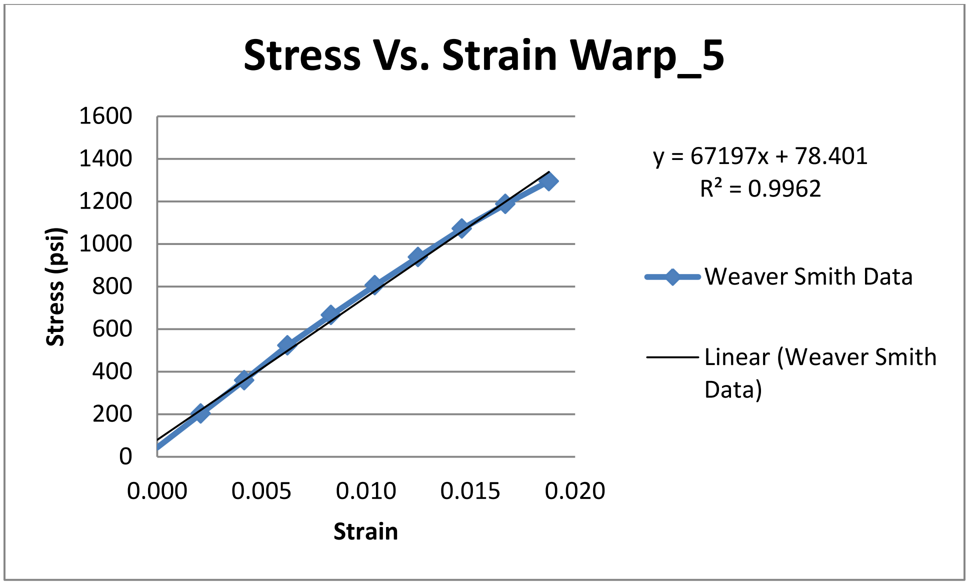

Figure 63: Stress-Strain Warp_5 Line of Best Fit

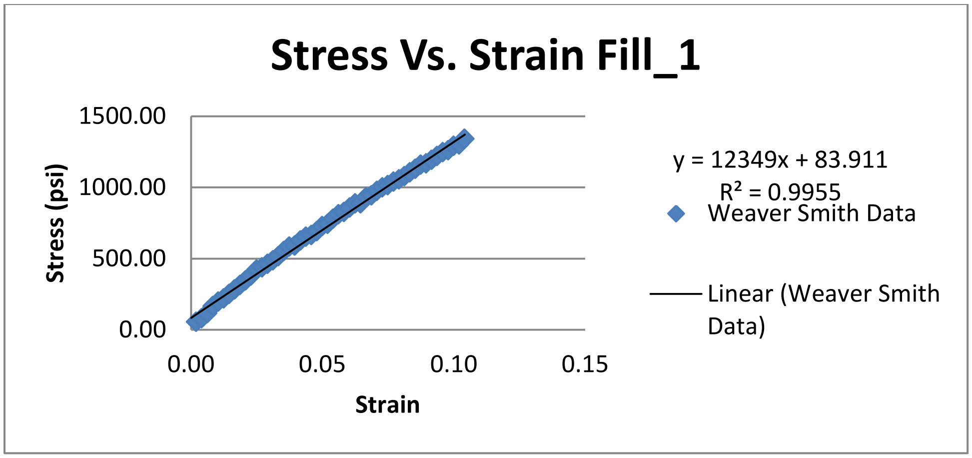

Figure 64: Stress-Strain Fill_1 Line of Best Fit

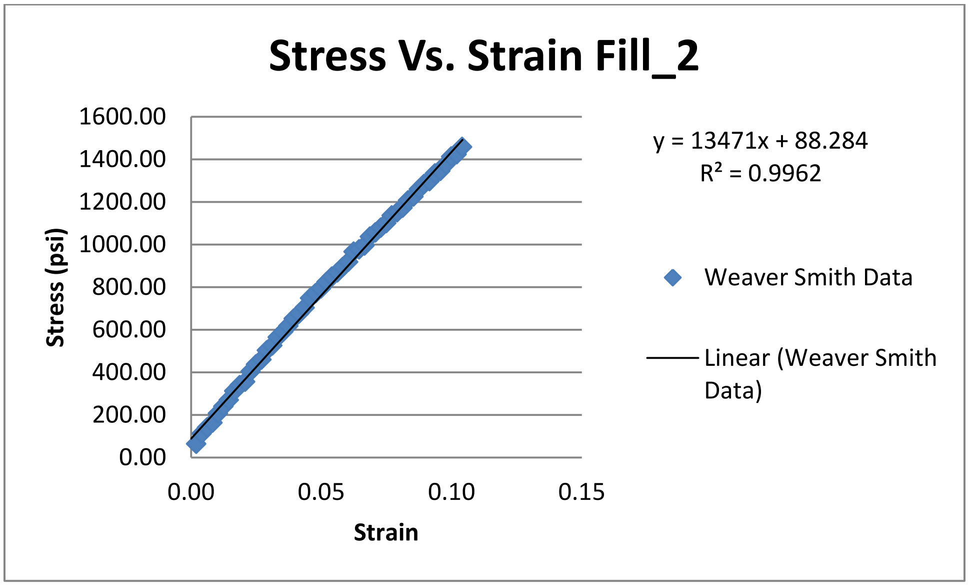

Figure 65: Stress-Strain Fill_2 Line of Best Fit

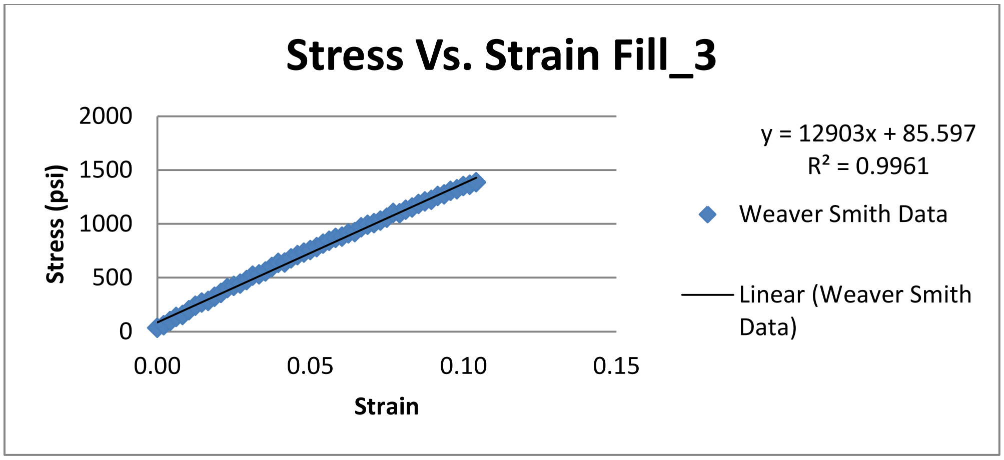

Figure 66: Stress-Strain Fill_3 Line of Best Fit

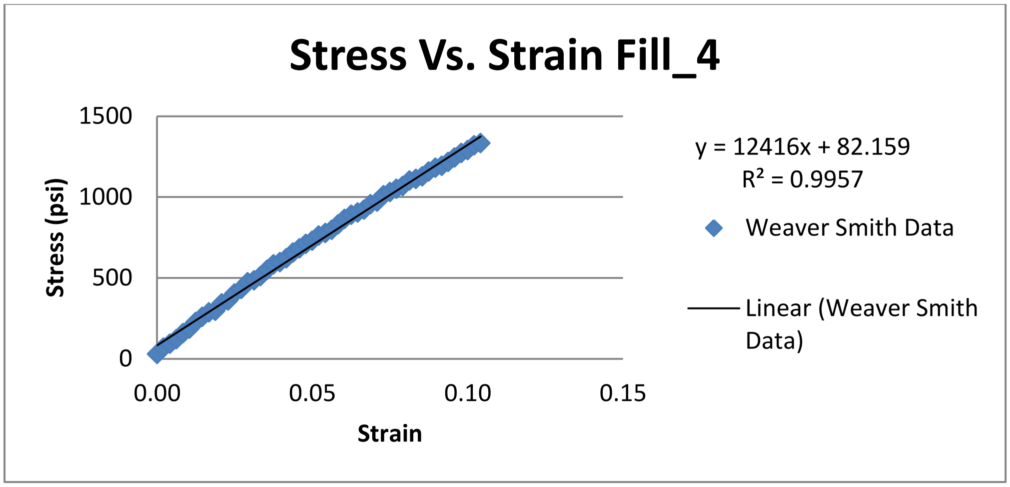

Figure 67: Stress-Strain Fill_4 Line of Best Fit

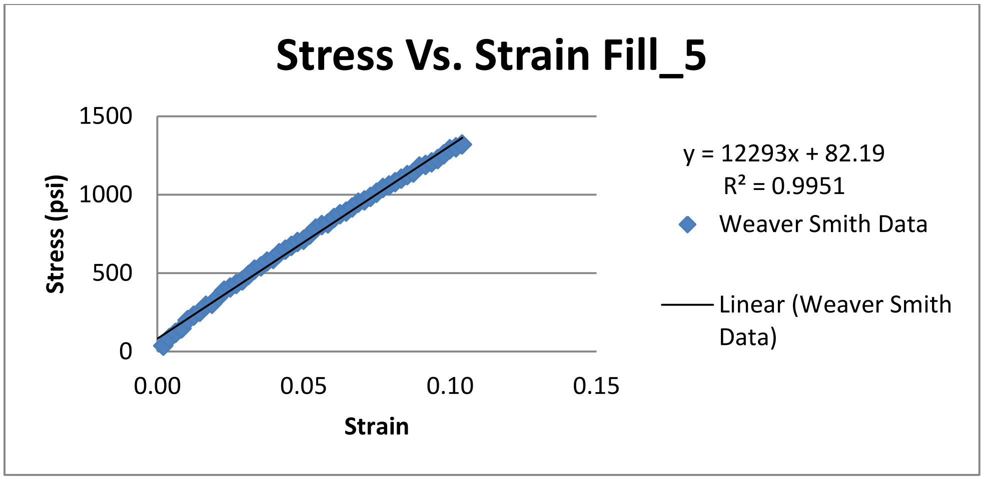

Figure 68: Stress-Strain Fill_5 Line of Best Fit

A.4 Yield Strength Graphs

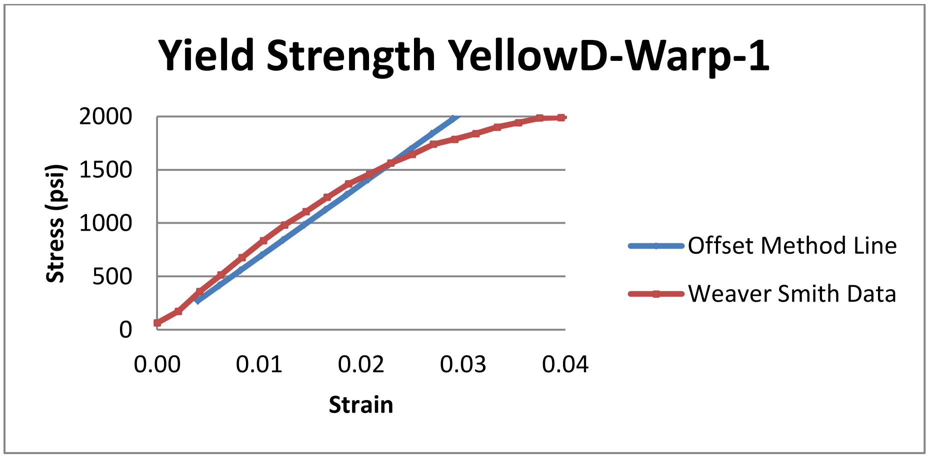

Figure 69: Yield Strength Warp_1

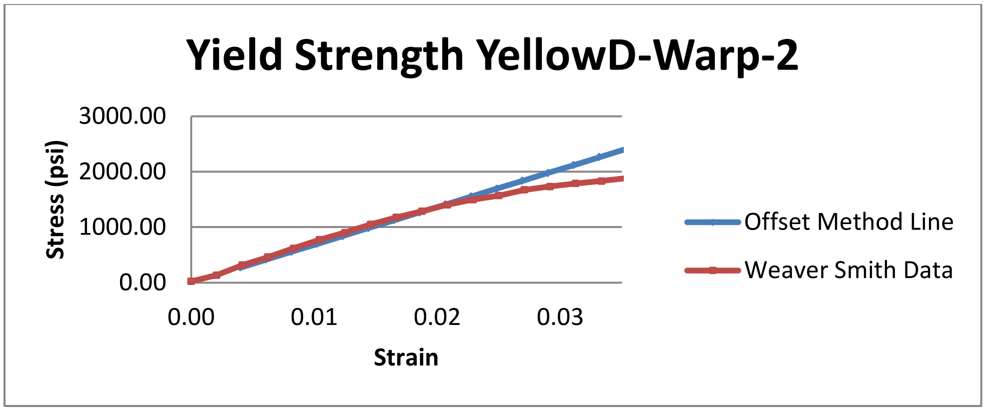

Figure 70: Yield Strength Warp_2

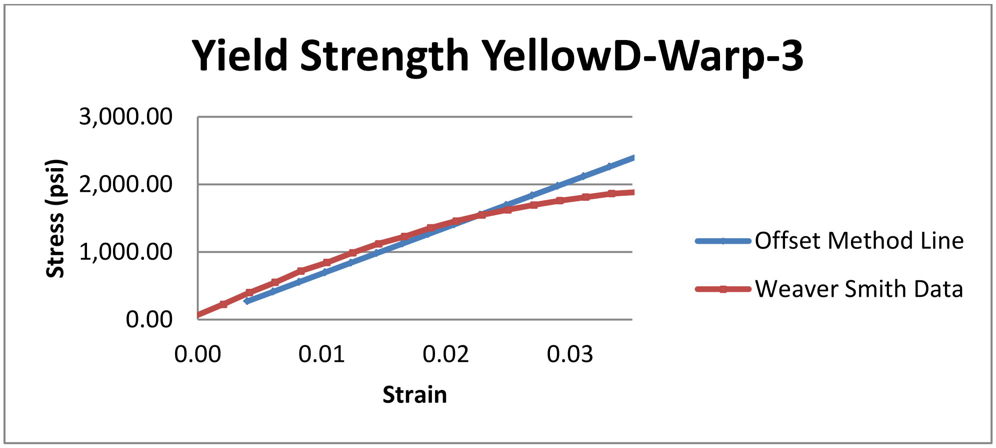

Figure 71: Yield Strength Warp_3

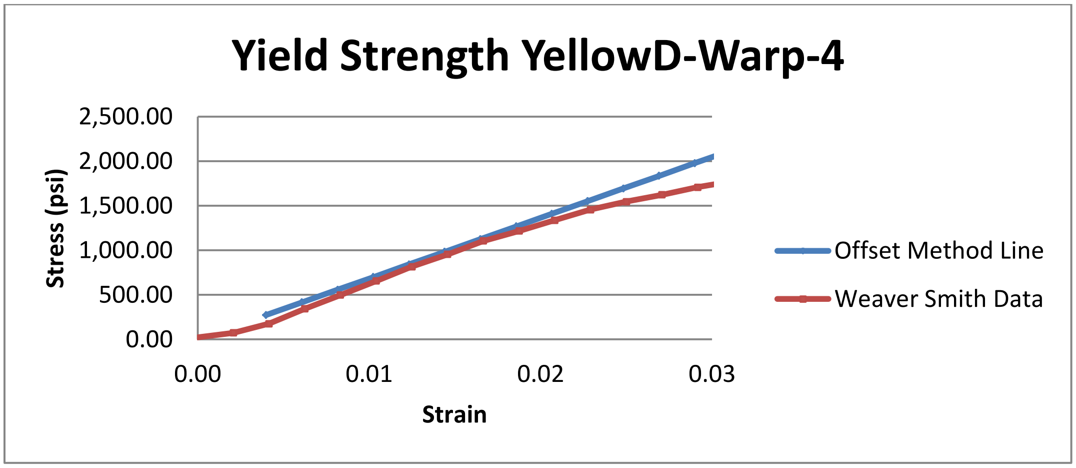

Figure 72: Yield Strength Warp_4

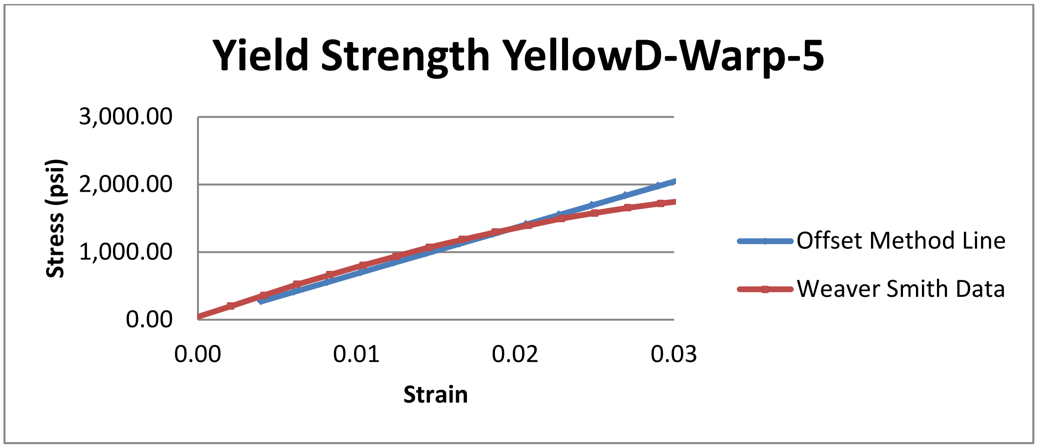

Figure 73: Yield Strength Warp_5

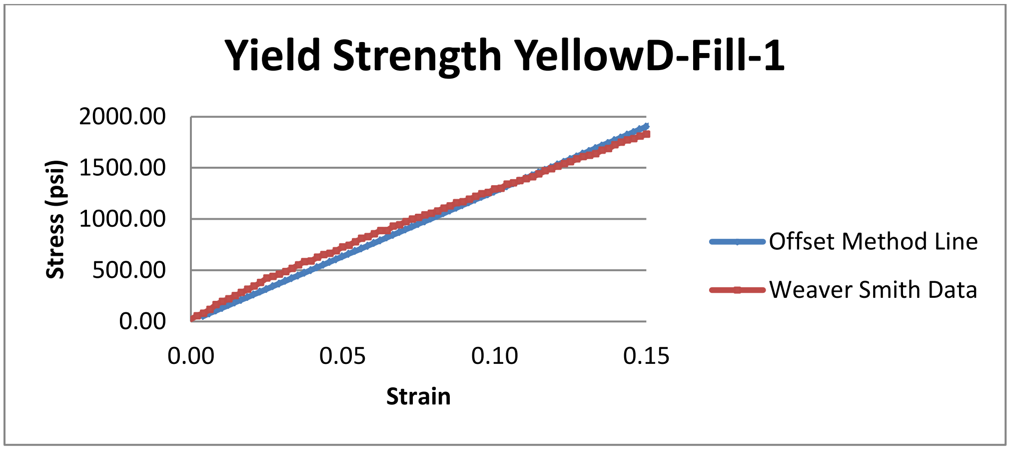

Figure 74: Yield Strength Fill_1

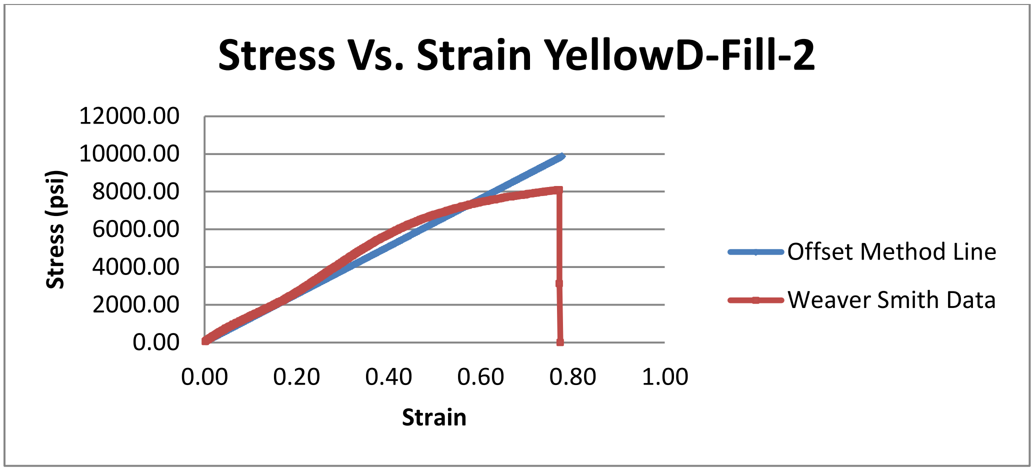

Figure 75: Yield Strength Fill_2

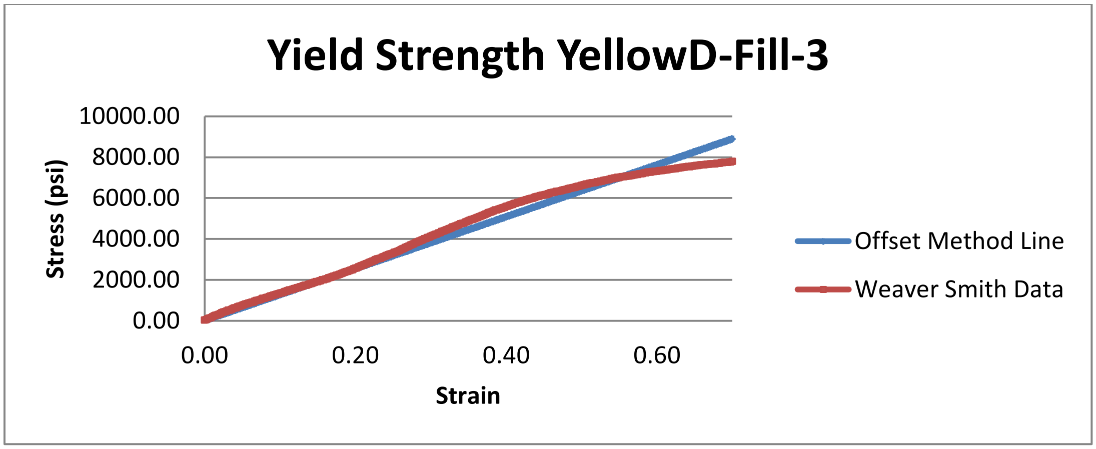

Figure 76: Yield Strength Fill_3

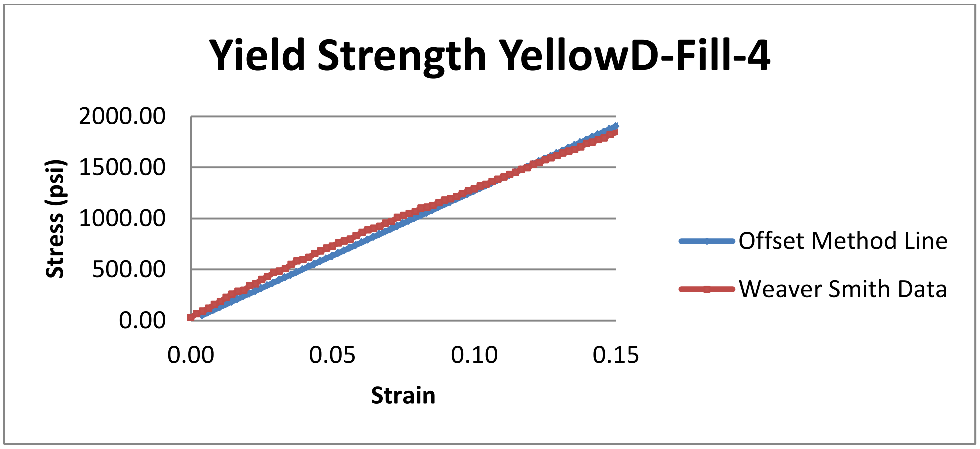

Figure 77: Yield Strength Fill_4

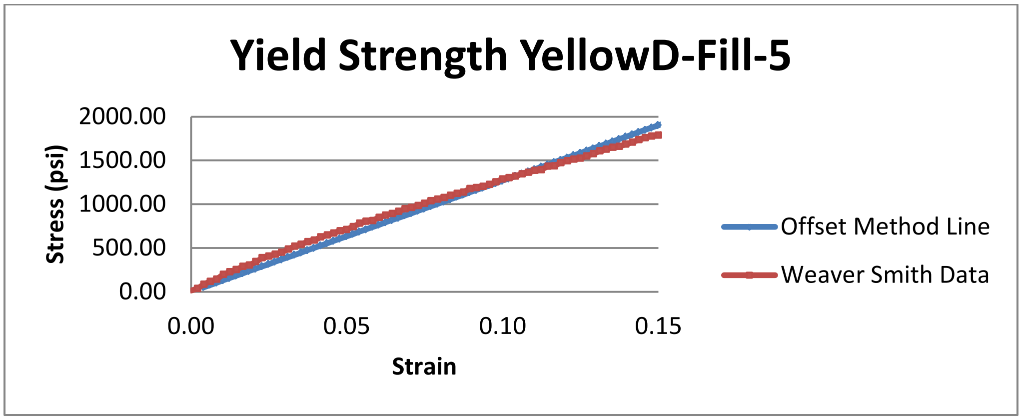

Figure 78: Yield Strength Fill_5

A.5 Contour Lines

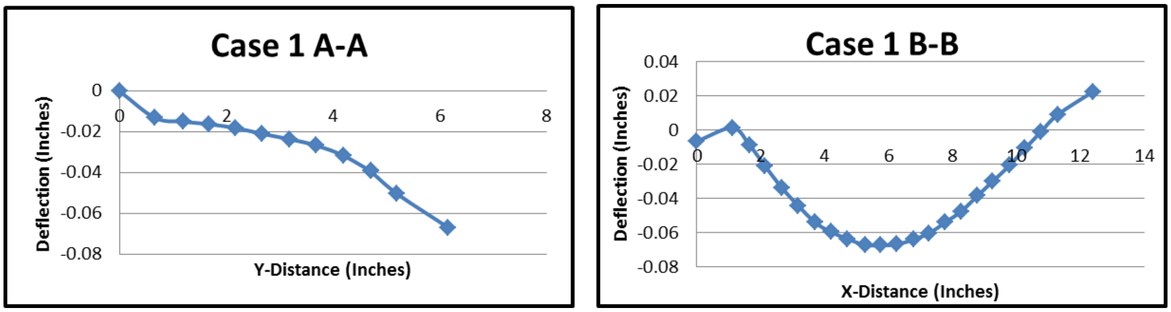

Figure 79: Case 1 Contour Lines

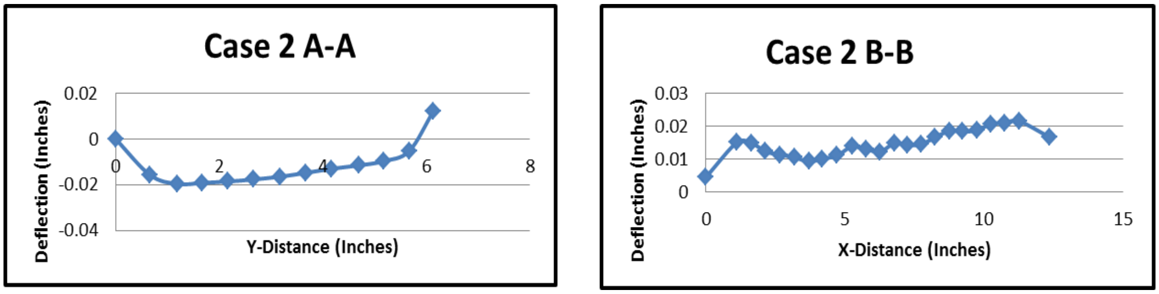

Figure 80: Case 2 Contour Lines

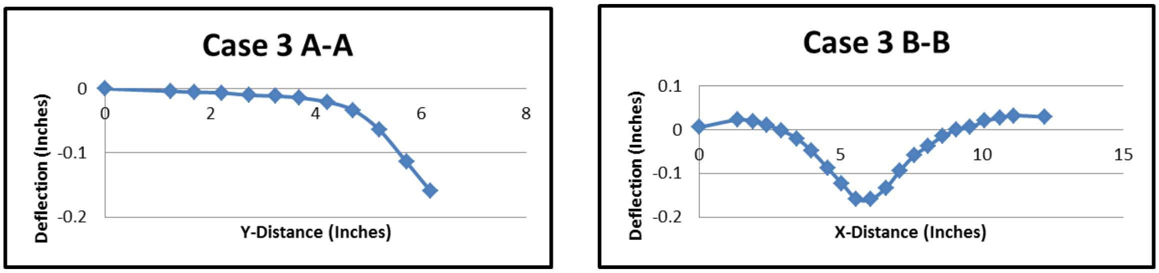

Figure 81: Case 3 Contour Lines

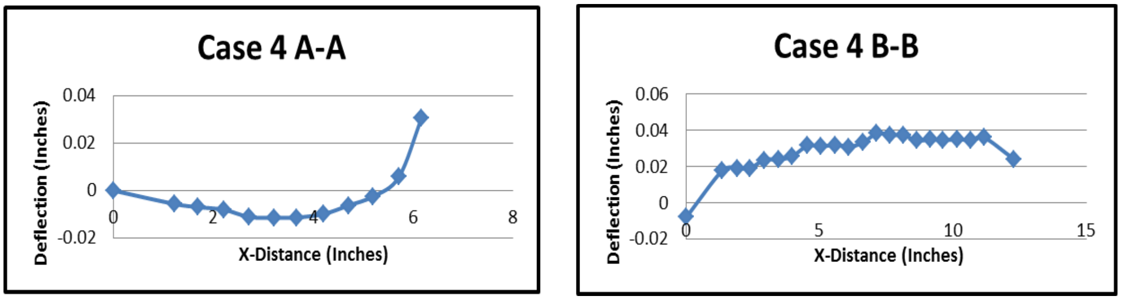

Figure 82: Case 4 Contour Lines

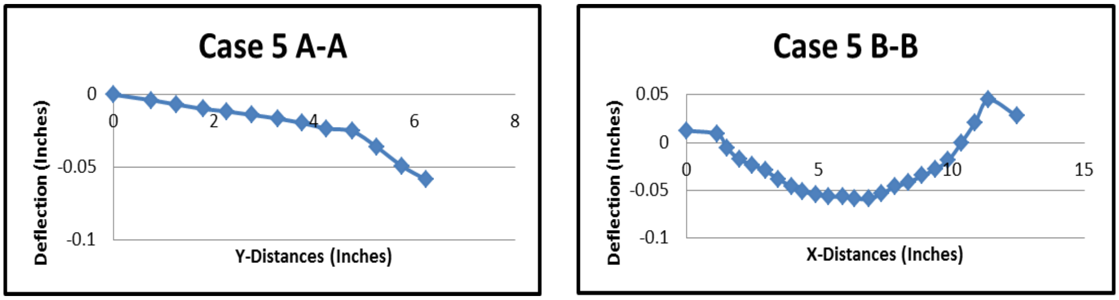

Figure 83: Case 5 Contour Lines

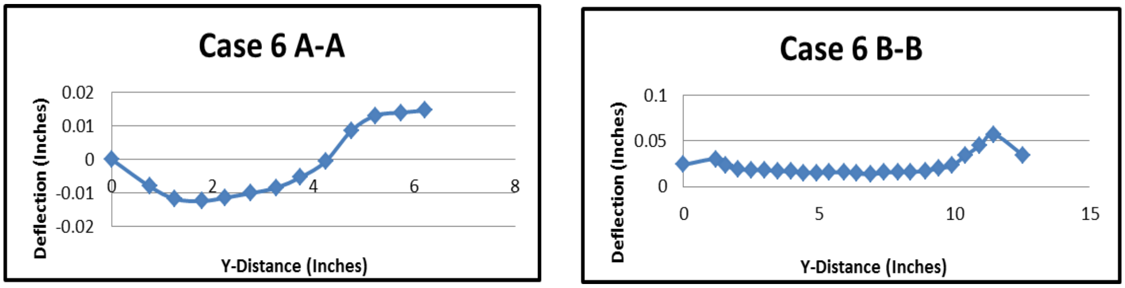

Figure 84: Case 6 Contour Lines

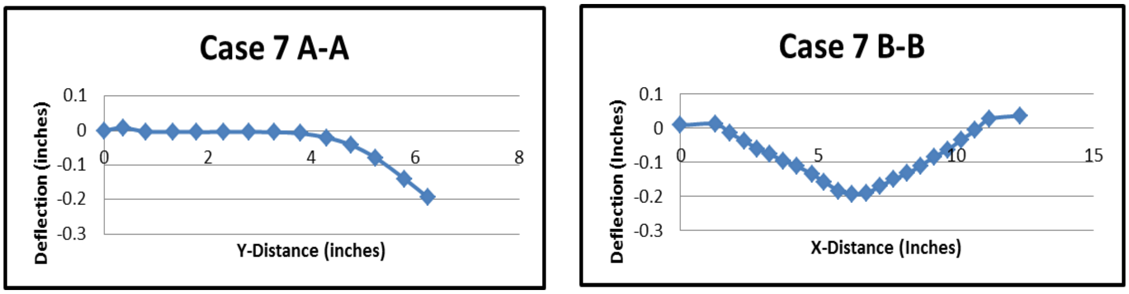

Figure 85: Case 7 Contour Lines

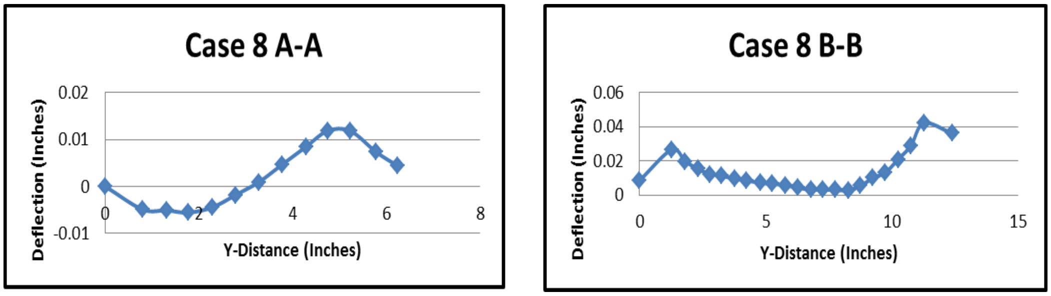

Figure 86: Case 8 Contour Lines

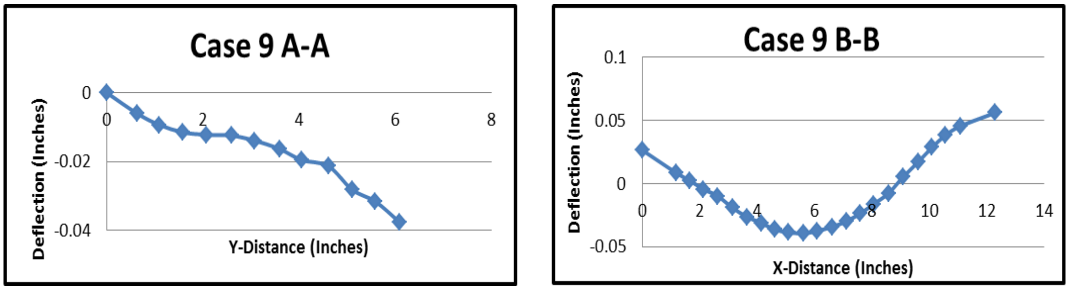

Figure 87: Case 9 Contour Lines

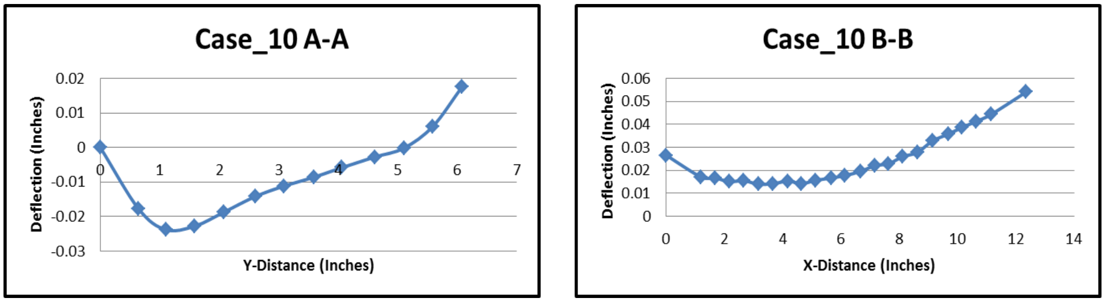

Figure 88: Case 10 Contour Lines

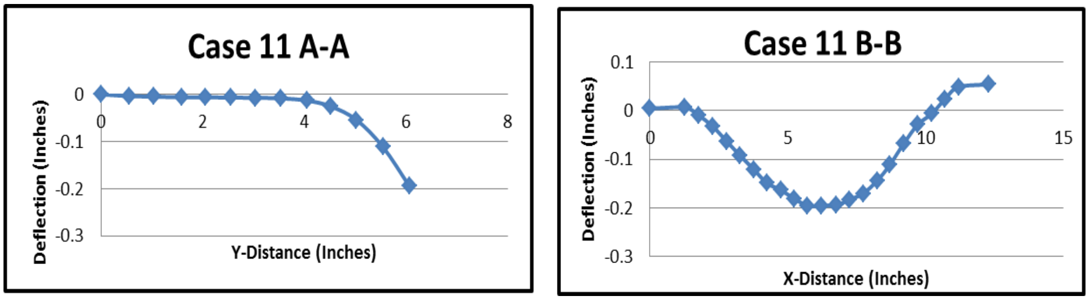

Figure 89: Case 11 Contour Lines

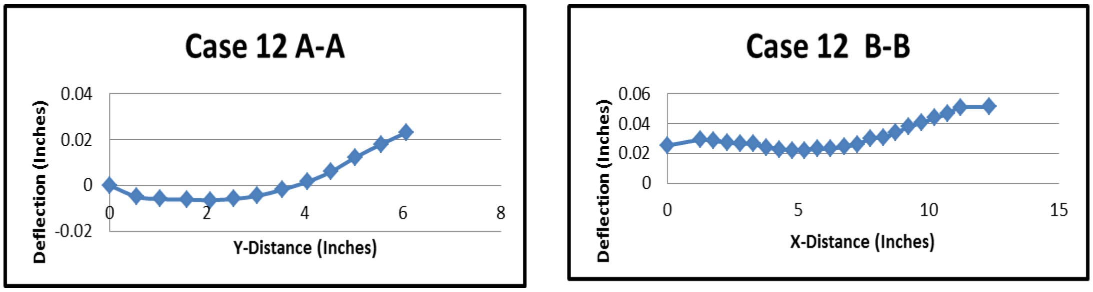

Figure 90: Case 12 Contour Lines

A.6 Contour Plots

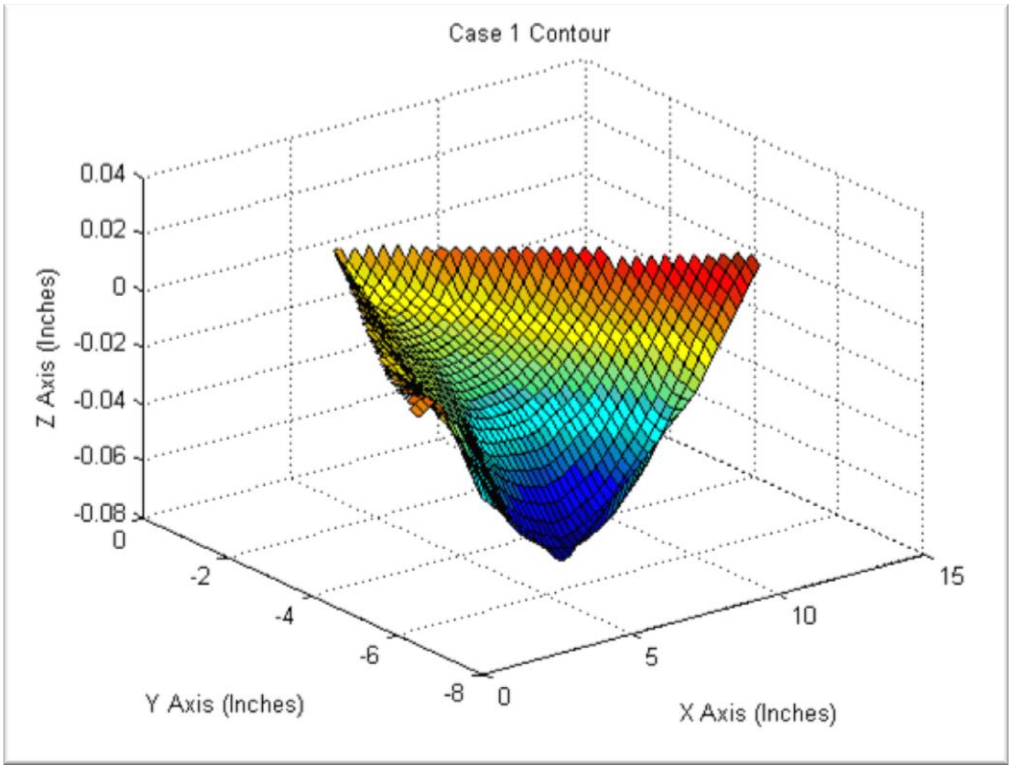

Figure 91: Case 1 Contour Plot

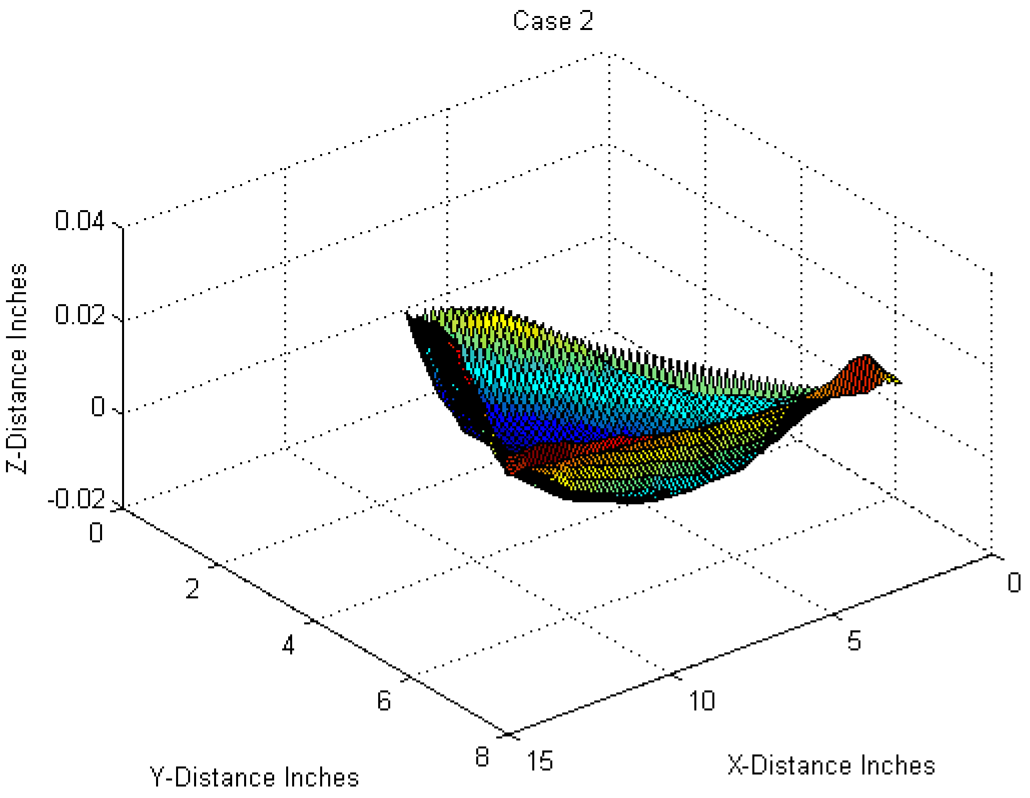

Figure 92: Case 2 Contour Plot

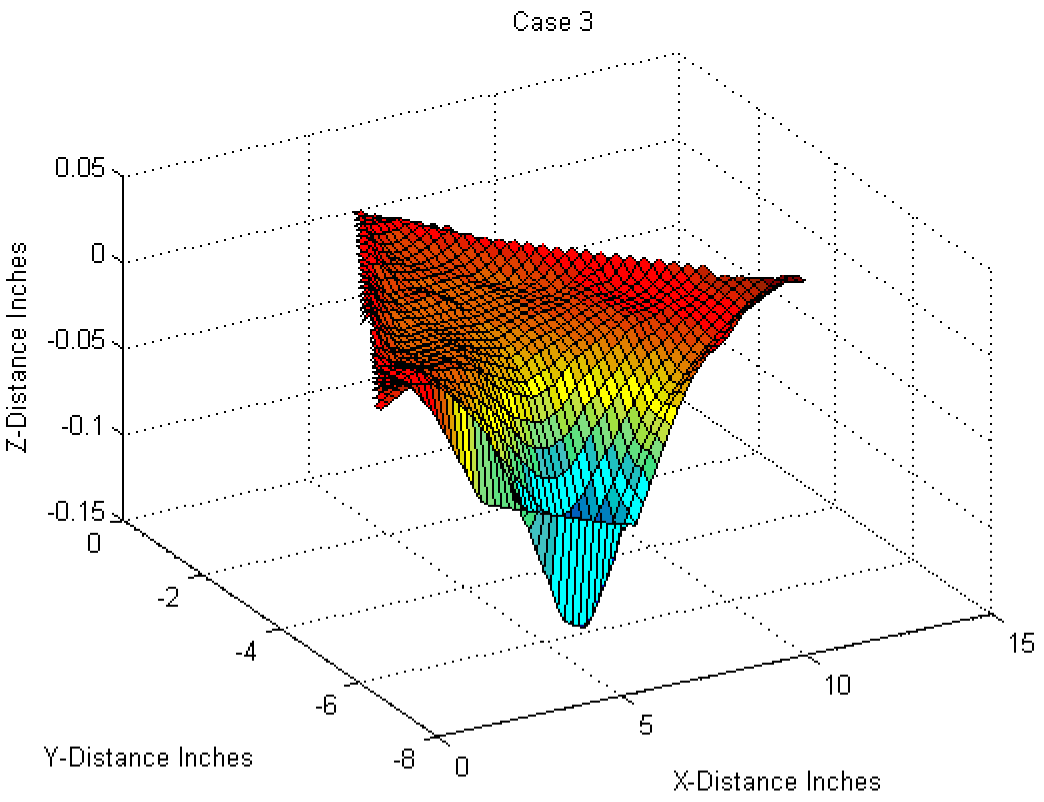

Figure 93: Case 3 Contour Plot

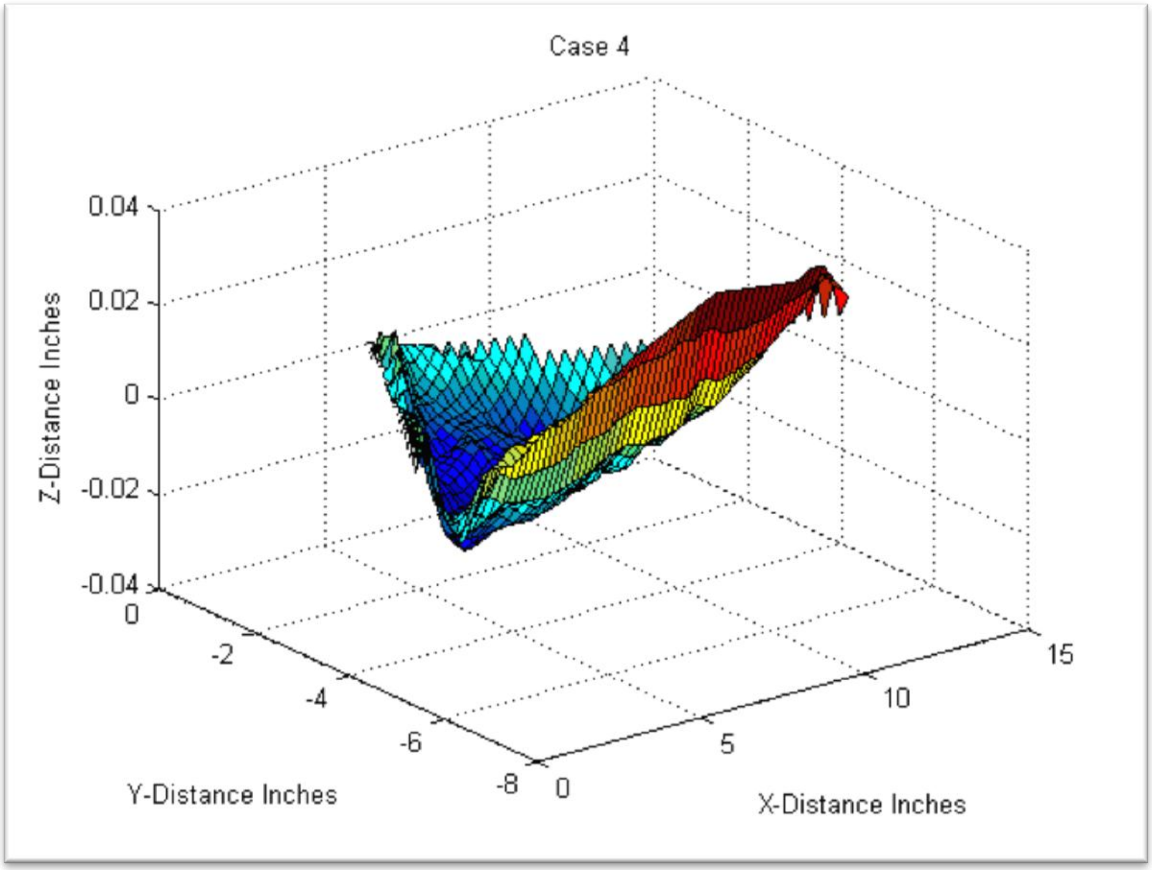

Figure 94: Case 4 Contour Plot

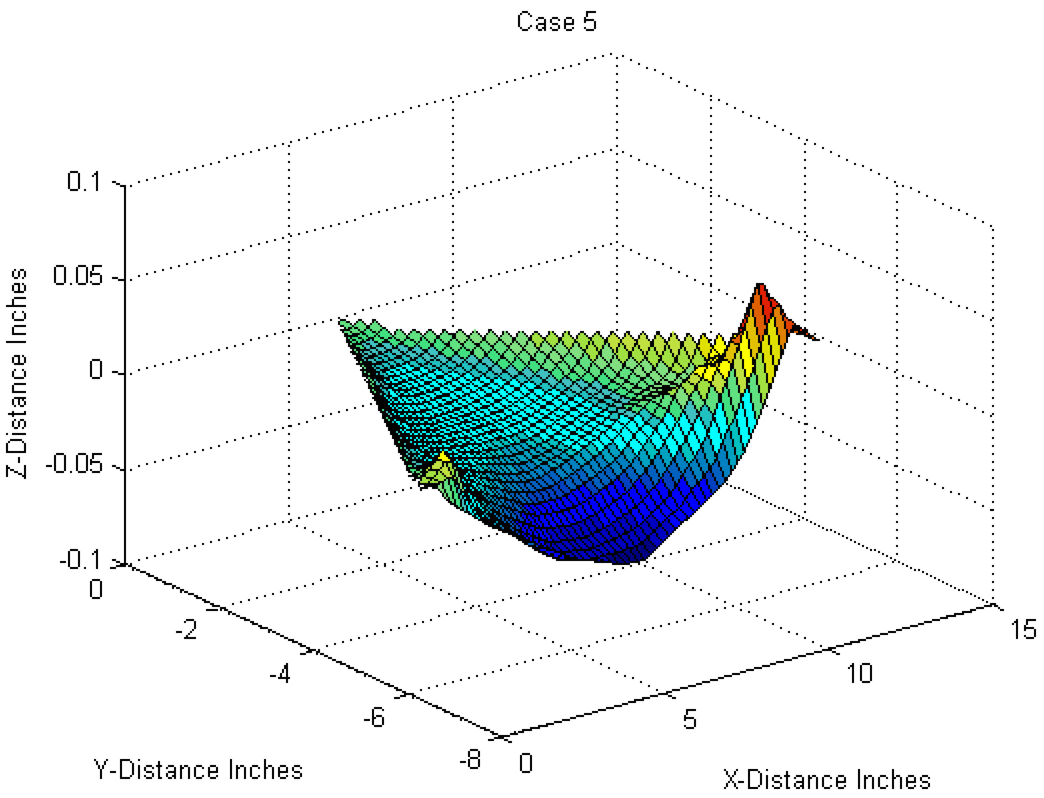

Figure 95: Case 5 Contour Plot

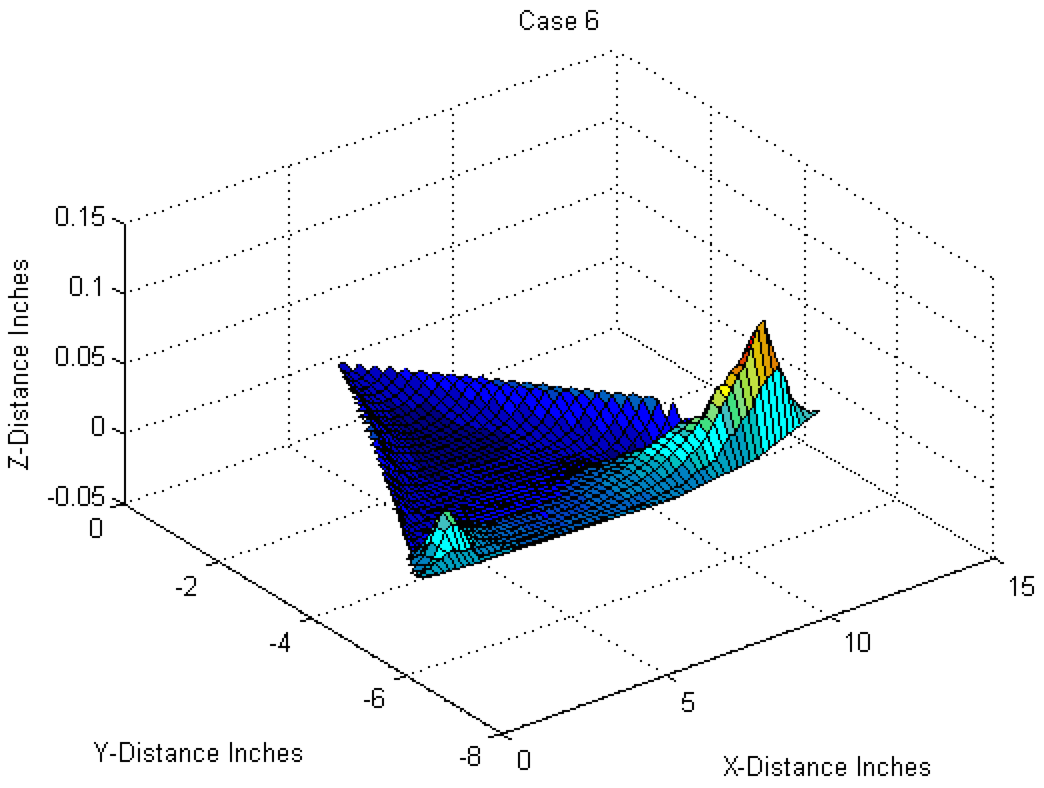

Figure 96: Case 6 Contour Plot

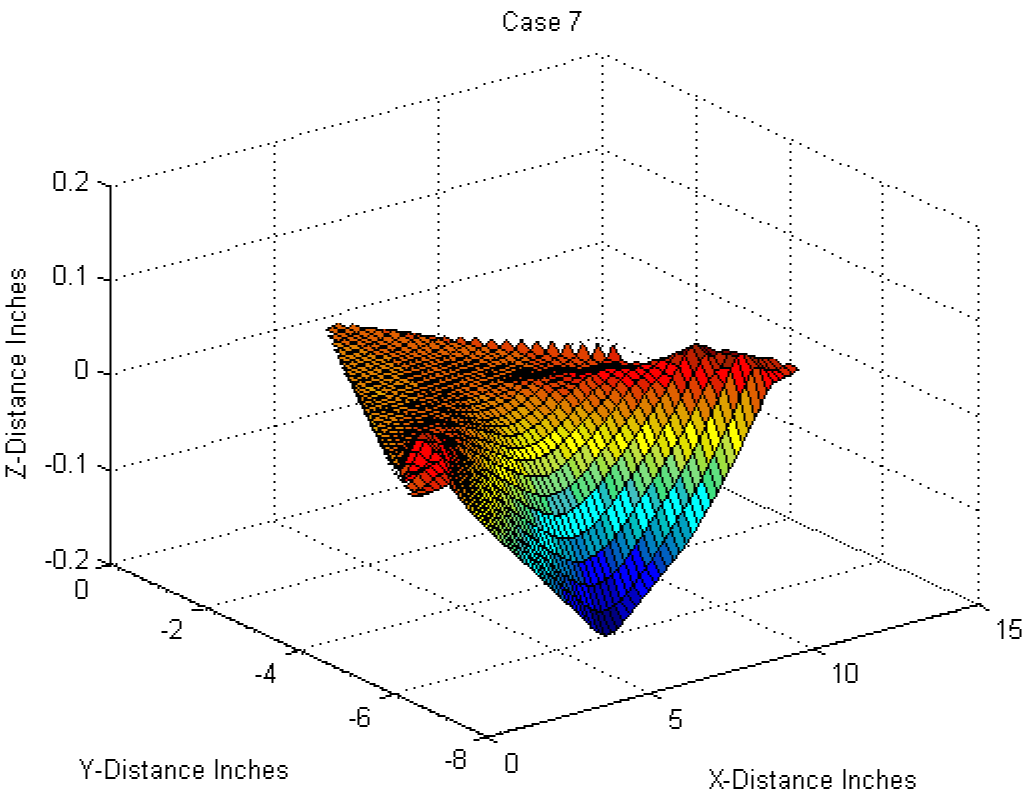

Figure 97: Case 7 Contour Plot

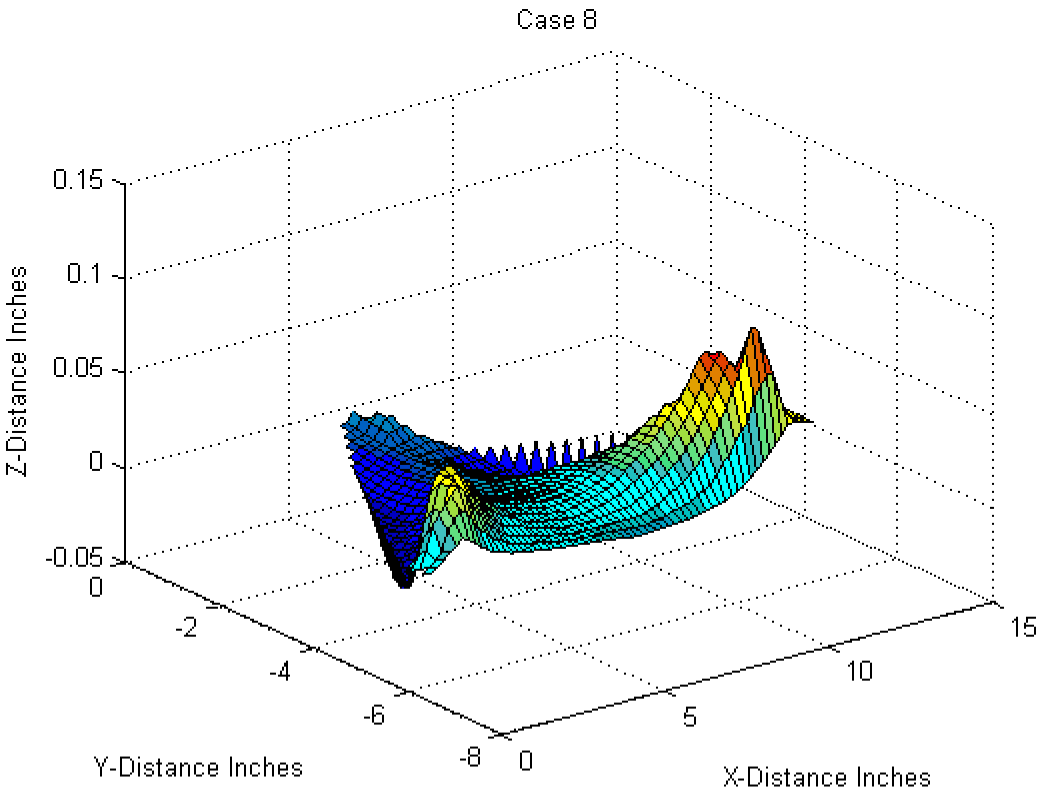

Figure 98: Case 8 Contour Plot

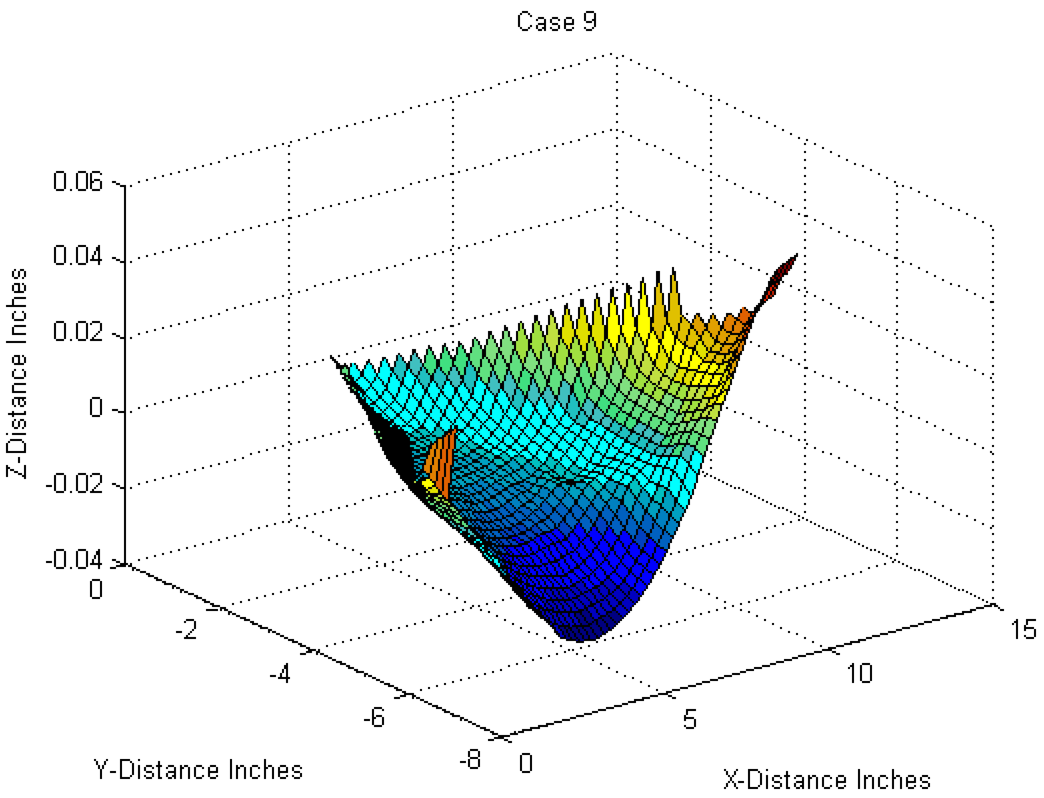

Figure 99: Case 9 Contour Plot

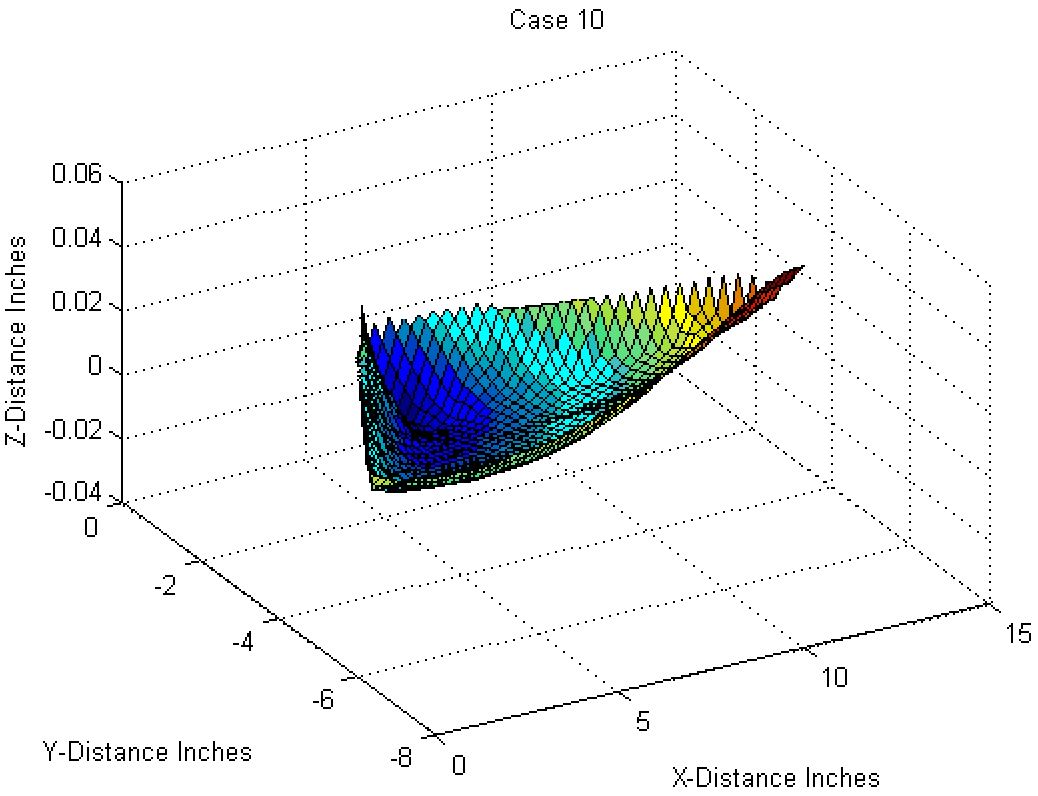

Figure 100: Case 10 Contour Plot

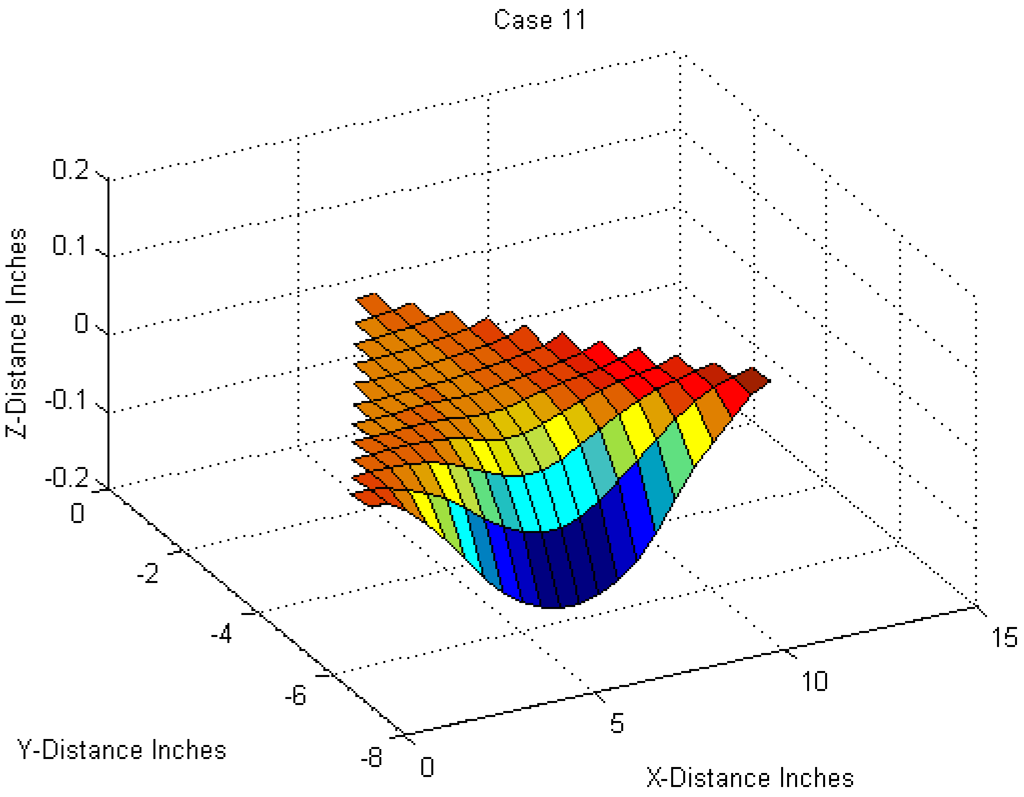

Figure 101: Case 11 Contour Plot

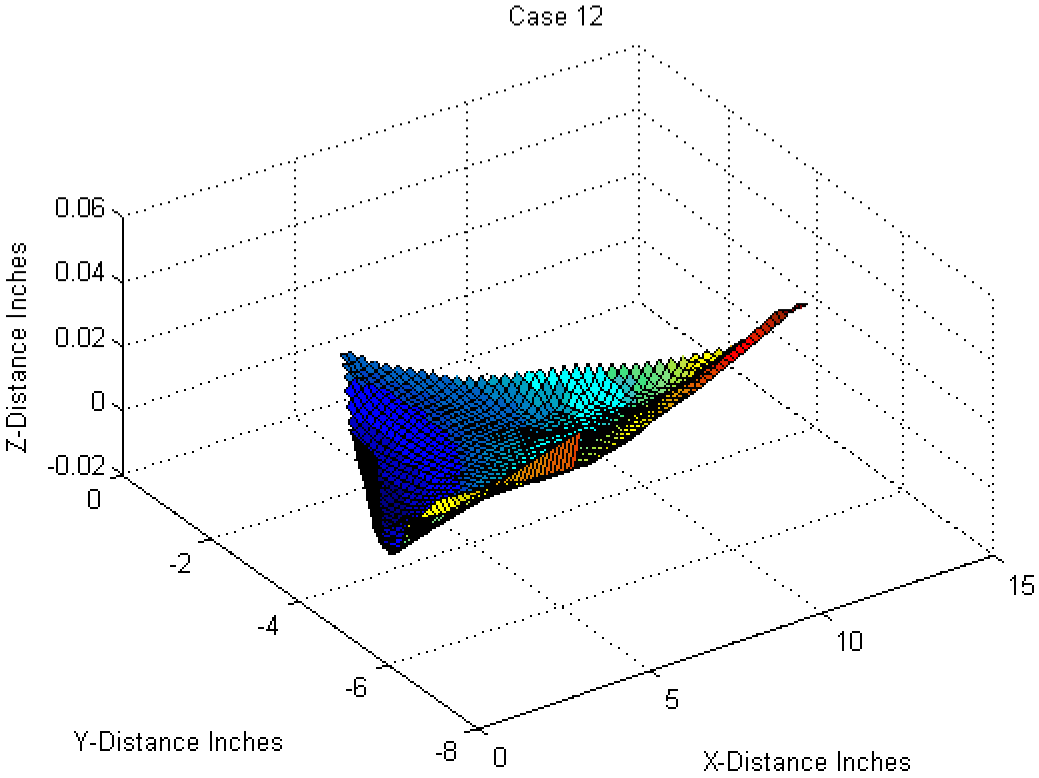

Figure 102: Case 12 Contour Plot

Bibliography

Small Solar Power Sail Demonstrator "IKAROS". (2012, January 6). Retrieved from Japan Aerospace Exploration Agency: http://www.jaxa.jp/projects/sat/ikaros/index_e.html

Anderson, J. L. (2011, November 29). *NASA'S Nanosail-D 'Sails' Home -- Mission Complete.* Retrieved from NASA: www.nasa.gov/mission_pages/smallsats/11-148.html

Budynas, R. G., & Nisbett, J. K. (2008). *Shigley's Mechanical Engineering Design 8th Edition.* New York, New York.

Callister, W. D., & Callister, W. D. (2000). *Fundementals of Materials Science and Engineering: An Integrated Approach.* (5th, Ed.) Wiley.

Clemmons, D. L. (1964). *The Echo I Inflation System.* Washington, D.C.: National Aeronautics and Space Administration.

Cobb, R. G., Black, J. T., & Swenson, E. D. (2010, July-August). Design and Flight Qualification of the Rigidizable Inflatable Get-Away-Special Experiment. *Journal Of Spacecraft And Rockets, 47*(4), 659-669.

Dharamsi, U. K., Evanchik, D. M., & Blandino, J. R. (April 22-25, 2002). Comparing Photogrammetry with a Conventional Displacement Measurement Technique on a 0.5m Sqaure Kapton® Membrane. *43rd AIAA/ASME/ASCE/AHS/ASA Structures, Structural Dynamics, and Materials Conference. AIAA 2002-1258.* Denver, Colorado: American Institute of Aeronautics and Astronautics.

Eos Systems Inc. (2009). PhotoModler Help. *PhotoModler 6*.

(Feb, 1997). *Preliminary Misson Report: Spartan 207/Inflatable AntenaExperiment Flown on STS-77.* Greenbelt, MD: NASA Goddard Space Flight Center.

Foch, R. J. (2011). *Omni-Directional Inflatable Radar Reflector.* Naval Research Laboratory.

Freeland, R. E., Bilyeu, G. D., Veal, G. R., & Mikulas, M. M. (1998). Inflatable Deployable Space Structures Technology Summary. *49th International Astronautical Congress.* Melbourne, Australia: International Astronautical Federation.

Freeland, R. E.; Veal, G. R. (1998). Significance Of The Inflatable Antenna Experiment Technology. *American Institute of Aeronautical and Astronautics, 98-2104*.

Fulcher, J. (2012, March 6). Development of modeling approach for design of precision inflatable structures. *37th Dayton-Cincinnati Aerospace Sciences Symposium*. Dayton, OH.

Ganci, G., & Brown, J. (2000). Developments in Non-Contact Measurement Using Videogrammetry. *Boeing Large Scale Metrology Conference.* Auburn, WA.

Harris, T. (2011, March 9). Thesis, Constrained Volume Packing Of Deployable Wings For Unmanned Aircraft. *Univerisity of Kentucky*. Lexington, KY, USA.

Jacob, J. D., Smith, S., Cadogan, D., & Scarborough, S. (2007). Expanding the Small UAV Design Space with Inflatable Wings. *AeroTech Congress and Exhibition. 07 ATC-217.* Los Angeles, California: SAE.

Jensen, M. (2004, August 31). *Solar Sails Could Send Spacecraft 'Sailing' Through Space.* Retrieved from NASA: http://www.nasa.gov/vision/universe/roboticexplorers/solar_sails.html

Leifer, J.; Belvin, W. K. (April, 2003). Prediction of Wrinkle Amplitudes In Thin Film Membranes Using Finite Element Modeling. *44th AIAA/ASME/ASCE/AHA Structures, Structural Dynamics, and Materials Conference. 2003-1983.* Norfolk, Virginia: American Institute of Aeronautics and Astronautics.

Lennon, A. (2008, April). Gossamer Structures Enable Space Engineers To Think Big. *Engineers Journal, 62*(3), 187-191.

Mathers, N. (February, 2010). *Inflatable Antena for Portable Direct Satellite Communication.* Melbourne, Australia: RMIT University.

Pappa, R. S., Black, J. T., & Blandino, J. R. (n.d.). *Photogrammetric Measurement Of Gossamer Spacecraft Membrane Wrinkling.*

Pappa, R. S., Black, J. T., Blandino, J. R., Jones, T. W., Danehy, P. M., & Dorrington, A. A. (2003, November-December). Dot-Projection Photogrammetry and Videogrammetry of Gossamer Space Structures. *Journal of Spacecraft and Rockets, 40*(6), 858-867.

Pasco. (n.d.). Rosevill, California. Retrieved from http://www.pasco.com/prodCatalog/ME/ME-9450_super-pulley/index.cfm

Shaver, L. (2011, July 13). Email. Kinetic Systems.

Simpson, A. D. (2008). Dissertation, Design and Performance of UAVs with Inflatable Wings. Lexington, KY: University of Kentucky.

Smith, S., & Fadi, A. F. (2009). *Materials for High Altitude Deployable Wings.* Mechanical Engineering, University of Kentucky.

Talley, C., Clayton, W., Gierow, P., Laue, G., McGee, J., & Moore, J. (April, 2002). Advanced Membrane Materials for Improved Solar Sail Capabilities. *43rd AIAA/ASME/ASCE/AHS/ASC Structures, Structual Dynamics, and Materials Conference: 3rd AIAA Gossamer Spacecraft Forum*, *AIAA 2002-1561.* Denver, Colorado.

Thomas, M., & Friese, G. J. (1980). Pressurized Antennas For Space Radars. *Sensor Systems for the 80's Conference* (pp. 65-71). Colorado Springs, Colorado: American Institute of Aeronautics and Astronautics.

Thota, P., Leifer, J., Smith, S., & Lumpp, J. K. (January, 2003). Initial Pattern Evaluation For Inplane Displacement Measurement Of Thin Films. *International Modal Analysis Conference IMAC-XXI.* Orlando, Florida.

Vita

Isaac John Scherrer

Born July 25th, 1986 in Cincinnati, OH

Education

MS, Mechanical Engineering, University of Kentucky (UK), Lexington, KY (August, 2012)

BS, Magna cum Laude, Mechanical Engineering, University of Kentucky, Lexington, KY (May 2010)

Professional Experience

Graduate Research Assistant – 02/2010-Present

- Dynamic Structures and Controls Lab, University of Kentucky, Lexington, KY

General Electric Aviation – 01/2008-08/2008

- Aviation Component Service Center
- Digital Engine Collaboration

Lab Technician – 05/2007 – 08/2007

- Rheinisch-Westfaelische Technische Hochschule (RWTH) Aachen, Germany

Planum Excavating – 05/2006-08/2006

- Commercial Excavating Estimator

Awards

- Awarded Research/Teaching Assistant Scholarship 2010-Present
- Marion T. Brooks Academic Scholarship 2008, 2009
- Thomas Tonkin Memorial Engineering Scholarship 2008, 2009
- Downey Engineering Scholarship 2006, 2007
- Academic Excellence Scholarship at University of Kentucky 2007, 2008
- Kuehner German Engineering Scholarship 2007
- Alpha Tau Omega Fraternity Scholarship 2006
- Dean’s list 2006 – 2010
- Graduated Magna Cum Laude from the University of Kentucky 2010
- Graduated Cum Laude from Highlands High School 2005